# Diamond photonic crystals for new bio-sensors

Petru Borta

Petru Borta. Diamond photonic crystals for new bio-sensors. Optics [physics.optics]. Université Paris Saclay (COmUE), 2019. English. NNT : 2019SACLS006 . tel-02014478

HAL Id: tel-02014478
https://theses.hal.science/tel-02014478
Submitted on 11 Feb 2019

# Cristaux photoniques en diamant pour la réalisation de bio-capteurs innovants

NNT : 2019SACLS006

Thèse de doctorat de l'Université Paris-Saclay
préparée à Université Paris Sud

École doctorale n°575
Electrical, optical, bio : physics and engineering (EOBE)
Electronique et optoélectronique, nano- et microtechnologies

Thèse présentée et soutenue à Saclay, le 09 janvier 2019, par

**Petru BORTA**

Composition du Jury :

| | |
|---|---|
| Jocelyn ACHARD<br>Professeur, LSPM Université Paris 13 | Président |
| Gaëlle LISSORGUES<br>Professeur, ISIEE Université Paris-Est | Rapporteur |
| Nicolas LE THOMAS<br>Professeur, INTEC Ghent University – IMEC | Rapporteur |
| Xavier CHECOURY<br>Professeur, C2N Université Paris-Sud | Directeur de thèse |
| Hugues GIRARD<br>Ingéneur de Recherche, CEA-LIST | Co-encadrant de thèse |

Thèse de doctorat

To my dear wife,
Delia

# Acknowledgments

Firstly, I would like to express my special appreciation and thanks to my supervisor Mr. Xavier Checoury for his confidence and also for giving me the opportunity to do this PhD thesis at the Centre de Nanosciences et de Nanotechnologies. I thank him for the continuous support and guidance during these three years. Despite his workload as a Master supervisor and his research, he always found the time to advise and to guide me regarding my research or my manuscript. I would also like to thank Mr. Hugues Girard, my co-advisor during this PhD thesis at the Laborateur Capteurs Diamant from CEA-LIST. His advice and help during this PhD work made this period easier. Also, I appreciate the insightful suggestions and discussions. Even if I did not interact as much as would have liked with the LCD laboratory, every time I went there I felt that I was part of the team.

I also want to express my gratitude to my committee members for the interest they brought to my PhD work. I would like to thank Mrs. Gaëlle Lissorgues and Mr. Nicolas Le Thomas for accepting to be my rapporteurs and for the careful reading of my manuscript. I thank equally Mr. Jocelyn Achard for accepting to be the President of my PhD jury.

I would like to thank to all the Quantum Dot group from C2N for the good moments that we spent together daily. Firstly, to Mr. Sébastien Sauvage, I would like to thank for the numerous scientific advises and for the time allocated to help me to better vulgarize my work. To Mr. Philippe Boucaud and Mr. Moustapha El Kurdi I would like to thank for sharing their scientific knowledge to help me surpass some of the encountered issues. To Mr. Zheng Han I want to thank for the help and advice regarding the clean room processes. A sincere thank you to Mr. Léonard Monniello for the help regarding the optical characterization of my samples. I would want to thank Mrs. Farsane Tabataba-Vakili, Mrs. Yijia Zeng, Mr. Iännis Roland, Mr. Mohamed Chaibi, Mr. Anas Elbaz and also to the Nanoélectronique members for the stimulating discussions that we had during the lunch or coffee time.

I would like to address my thanks to all the LCD group for the good moments that we spent together and for the warm welcome at each of the organized events. A big thank you to Mr. Samuel Saada, who despite his charged planning, he found the time to teach me the secrets of the DIADEME reactor. He shared his scientific knowledge regarding the diamond growth in an easy way to understand. I want to thank Mr. Jean Charles Arnault, Mrs. Céline Gesset and Mrs. Christine Mer for the rich scientific and personal interactions. I thank my fellow PhD colleagues Mr. Julien Dechevalrie, Mr. Kee Han Lee, Mrs. Magdalena Kurzyp, Mr. Cyrile Barbay and Mrs. Amélie Venerosy for the nice moments spent together.

A big part of my PhD thesis was dedicated to clean room fabrication processes. For that, I want to thank all the clean room engineers for the trainings and their expertise which allowed me to advance in my research, especially to Mr. Etienne Herth, Mr. David Bouville, Mr. Fabien Bayle, Mr. Xavier Le Roux, Mrs. Natalie Isac, Mr. Jean-Rene Coudevylle, Mr. Abdelhanin Aasime.

My last thank you are for all my family. I will be grateful to them knowing the sacrifices they did for me to arrive at this moment. A big thank you for my wife, Mrs. Elena-Delia Pascalu, who supported me during this PhD and beyond.

université PARIS-SACLAY
ÉCOLE DOCTORALE
Physique et ingénierie : électrons, photons, sciences du vivant (EOBE)

**Titre : Cristaux photoniques en diamant pour la réalisation de bio-capteurs innovants**

**Mots clés :** cristaux photoniques ; bio-capteurs ; diamant ;

**Résumé :** Au cours des dernières années, la recherche dans le domaine des bio-capteurs optiques sans marquage a connu une croissance rapide du fait de la nécessité de développer des méthodes toujours plus performantes pour la détection et la mesure de faibles concentrations de molécules spécifiques dans divers domaines. Parmi les différentes méthodes optiques existantes, les cristaux photoniques (CP) offrent une alternative prometteuse du fait de leur sensibilité. D’autre part, le diamant, utilisé comme matériau pour la réalisation de ces dispositifs offre de bonnes propriétés optiques et la possibilité de réaliser une fonctionnalisation de surface efficace facilement. Dans ce contexte, cette thèse propose un nouveau design de bio-capteur optique à cristaux photonique bi-dimensionnel en diamant, fonctionnant à des longueurs d'onde proche de 800 nm.

Une géométrie originale de trous d'air circulaires organisés selon une maille carrée a été choisie pour maximiser la sensibilité du bio-capteur à des changements d'indice de réfraction en leur surface. Il a été démontré analytiquement que les modes à faible vitesse de groupe avaient une plus grande sensibilité à ces changements. Des méthodes numériques ont permis de préciser les paramètres géométriques optimaux du CP.

Le design proposé est basé sur la mesure de décalage angulaire dans le spectre en réflexion d'un mode lent résonant du CP quand celui-ci est éclairé par une lumière monochromatique.

Des films de diamant polycristallin de quelques centaines de nanomètres à quelques micromètres d’épaisseur ont été déposés sur différents substrats. L’ensemble des procédés technologiques nécessaires à la réalisation des CP et spécifiques aux films de diamant polycristallin ont été développés ou optimisés, comme, entre autre, un procédé de lissage obtenu par gravure plasma, un procédé de transfert de films de diamant sur un autre substrat par collage, un procédé d’amincissement des films de diamant et la fabrication des CP par lithographie électronique et gravure plasma.

Les échantillons réalisés dans la salle blanche du C2N ont été mesurés optiquement et les hypothèses théoriques concernant les performances du capteur ont étés validées. Un mode avec une vitesse de groupe c/100 à une longueur d'onde de 800 nm a été mesuré et la sensibilité correspondant a cette structure a été estimée à 500 degrés par unité d'indice de réfraction (°/RIU), une valeur supérieure d’un ordre de grandeur à celles rencontrées couramment dans les capteurs à CP bidimensionnels. Ces résultats représentent un premier pas vers un biocapteur hautement sensible, comprenant une fonctionnalisation de surface du diamant pour une reconnaissance de cible spécifique.

**Université Paris-Saclay**
Espace Technologique / Immeuble Discovery
Route de l’Orme aux Merisiers RD 128 / 91190 Saint-Aubin, France

université
PARIS-SACLAY

ÉCOLE DOCTORALE
Physique et ingénierie :
électrons, photons,
sciences du vivant (EOBE)

**Title :** Diamond photonic crystals for new bio-sensors

**Keywords :** photonic crystal ; bio-sensor ; diamond ;

**Abstract :** Over the last years, the research on the label-free biosensor topic has experienced a very rapid growth because of the need to develop high-performing methods to detect and measure low concentrations of specific molecules in various fields. Among all the methods proposed, photonic crystals (PhC) structures offers a good alternative due to their sensitivity. Moreover, the use of diamond as material make the proposed device more attractive due to its optical properties, high chemical stability and efficiency of surface functionalization. In this context, this PhD thesis propose a new design of optical bio-sensor based on diamond two-dimensional photonic crystals, working at the wavelength near 800 nm.

An original geometry of circular air holes arranged in squared lattice was chosen in order to maximize the sensitivity of such photonic structures to refractive index changes on their surface. It was analytically proven that modes with low group velocity are more sensitive to these variations. Numerical methods gave the necessary information to determine the optimal geometrical parameters of the PhC. The proposed design is based on measuring the shift of the angular reflectivity of a low group velocity guided mode resonance (GMR) PhC when probed with a single frequency light.

Polycrystalline diamond films were grown on two different substrates, with thicknesses ranging from a few hundreds of nanometers to several micrometers. The technological processes required for the realization of PhC on polycrustalline diamond were developed or optimized, such as surface planarization by inductively coupled plasma (ICP) dry etching, diamond film transfer onto new substrate by wafer bonding process, diamond films thinning and surface patterning with PhC using Electronic Beam Lithography (EBL) and ICP methods.

The samples realized in clean-room facilities were optically measured and the theoretical assumptions were validated. A GMR with a c/100 group velocity at a wavelength of 800 nm was measured and its sensitivity is estimated to be in the order of 500 degrees/ refractive index unit (°/RIU), a value that is one order of magnitude higher than the typical values encountered for sensors based on 2D PhC. These results represents a first step towards a highly sensitive bio-sensor, including a diamond surface functionalization for specific target recognition.

**Université Paris-Saclay**
Espace Technologique / Immeuble Discovery
Route de l’Orme aux Merisiers RD 128 / 91190 Saint-Aubin, France

# Contents

# General introduction

The development of high performing optical sensors represents a real challenge in order to satisfy the requirements demanded in various domains, such as healthcare (detection of pathogens), food safety (microbiological analyzes) or defense and security (toxic gas detection). The research interest in optical sensors, especially in refractive index sensors, can be linked on their detection performances, low cost, real time analysis and miniaturized dimensions. The technological progress become sufficiently advanced to realize structures with design dimensions at the nanometric scale. The accomplishment of these types of compact devices for biophotonics represents a major impact on the study and characterization of biological phenomenons, for example the interaction between two types of molecules (probe and target).

In this context, numerous structures were proposed based on integrated optics. In particular, the remarkable optical properties of the photonic crystals (PhCs) have led to the design of various photonic devices for different applications. The PhCs offers the possibility of fabricating structures with high quality factors (Q), small modal volumes, and, as a consequence, enhanced interactions between light and matter. Along these properties well desirable for sensing, this approach does not require a prior labeling of the target molecules. Moreover, the real time direct method of quantification of the molecular interaction probe / target on the surface of the PhC structure simplifies the detection procedure.

At present, the materials used for sensing photonic devices are, in majority, silicon, silicon nitride and glass. These materials are well known in micro-fabrication field, thus the production of large quantities of devices at low prices is possible. Though, the efficiency of surface functionalization on these materials is low. As consequence, the fabrication of optical biosensors on other materials, in particular materials compatible with bio-chemical studies, triggered a lot of research. Since the development of growth methods of synthetic diamond, various designs of chemical and biological sensors on this material were proposed. In particular, polycrystalline diamond represents a candidate for the fabrication of label-free optical biosensors, due to its physico-chemical properties, its compatibility with standard micro-fabrication technologies and the possibility of growth of large surface films on different substrates. The possibility to fabricate photonic crystal structures on diamond and the surface functionalization by covalent bonds represents desired properties for the biosensors.

This PhD thesis propose a new photonic crystal optical label-free biosensor for detection at the limit of the visible wavelength range. The proposed design was optimized to be sensitive to small refractive index variations. This thesis work was realized in the frame of collaboration between the Laboratoire Capteurs Diamant (LCD) from CEA-LIST Saclay, where the growth of polycrystalline diamond samples was produced, and the Quantum dot and photonic nanostructures group from the Photonic department of Centre for Nanoscience and Nanotechnology (C2N), where the numerical simulations, clean-room fabrication of the proposed design and samples measurements occurred.

In the first Chapter, I start by describing general notions for optical biosensors. After a classification based on the transduction type, the working principle of the optical biosensors and their main performances parameters will be described. In the second part of the Chapter will be presented some basic properties of photonic crystals, followed by a brief presentation of two types of photonic crystal technologies available, while comparing their performances with the surface plasmon resonance (SPR) technology, which is the reference method for the optical label-free biosensor field. Further on, diamond will be introduced as transduction material, where some optical properties suitable for biosensing will be presented.

The second Chapter is dedicated to the conception of photonic crystals oriented for biosensing. Given the innovative method of the proposed device to detect refractive index variations, the conception requires a good comprehension of the physical phenomenon that occurs when the light is introduced to the structure. The design will be described in detail, followed by the introduction of the appropriate sensitivity formula to determine the sensing performances. Numerical simulations will be performed by different methods, and the results will allow us to describe the light behavior inside of the photonic crystals in different conditions. Two different types of PhC designs oriented for sensing for visible wavelength range will be proposed. The strategy to maximize the sensitivity values for each design type and the theoretic sensor performances will be exposed.

In the third Chapter are presented the polycrystalline diamond film growth conditions and the technological micro-fabrication processes involved in the realization of polycrystalline diamond photonic crystals biosensors. The optimization and development of new protocols for device fabrication with better optical properties and performances will be described. Firstly, the surface smoothing protocol optimization of the polycrystalline diamond films will be shown, with the goal of processing thicker diamond films than previously reported. Secondly, a polycrystalline diamond film transfer method onto different substrates will be described, with the aim to realize films with higher crystalline uniformity. Thirdly, the fabrication of photonic crystal structures on polycrystalline diamond films on two different substrates will be presented.

The forth Chapter involves the optical characterization of the fabricated diamond PhCs structures on different substrates. Firstly, the experimental setup and results of optical measurements of the different PhC configurations will be discussed, results that will be compared to the numerical simulations. Different experimental setup configurations will be described, with the aim to validate the theoretical assumptions. Secondly, measurements at different temperatures will be described, experiments that allow us to estimate the sensitivity values for the fabricated sensor.

# Chapter 1

# Two dimensional diamond photonic crystal interest for optical label-free bio-sensing

## 1.1 Introduction

Biosensor - related research has experienced a very rapid growth over the last years because of the need to develop high-performing methods to detect and measure low concentrations of gases or specific molecules in biological, environmental or food samples ([1]). The biosensor requirements are more and more stringent in order to respond to the demands in different fields, such as healthcare, food safety or defense and security. Real time detection and easy to read result are among the requirements for the biosensors. Equally, the devices need to be compact, compatible for integration in portable systems and to have a reduced cost. In this first Chapter are presented several examples of optical label-free technologies, with their advantages and limitations. I start by introducing general concepts of biosensors, reviewing a few examples of different types of transduction methods and their application. The second part of the Chapter is focused on optical biosensor methods, where a brief state of the art is presented. In the next section are introduced some basic properties for photonic crystals used in this thesis. Further, a brief state of the art of two types of photonic crystal technologies available will be done, while comparing the performances with the surface plasmon resonance (SPR), which is the reference technology in the optical label-free biosensor field. Polycrystalline diamond will be introduced as a candidate as the transduction material for our proposed design, and some of its optical properties suitable for biosensing will be presented.

## 1.2 Types of available biosensors

Various definitions and terminologies are used to define a biosensor, depending on the field of application. It can be described as an analytical device that detect and quantify a particular physico-chemical phenomenon and convert it into an easily exploitable quantity for the user (it can be an electrical, acoustic, piezoelectric, optical signal etc). Generally, a biosensor is composed of two main parts : a sensitive element and a transducer. The ability to detect specific biological interactions is provided by the sensitive element. The biosensor needs to be capable to translate the recognition event into a physical measurable signal, characteristic that is assured by the transducer. The device is completed by an interface between the measured signal and the user.

### 1.2.1 Sensitive element

The sensitive element consists of a set of biological molecules, such as proteins, enzymes, antibodies, nucleic acids (DNA or RNA) or other biomimetic components. Such biosensors need to be able to quantify the interactions, bindings or recognition events with the analyte solution / environmental medium under study. The detection is required to be selective and specific to the targets, to accurately monitor their evolution. These requirements can be very challenging as a multitude of different components are present in a biological solution (blood, saliva, urine etc) or in air, whist the target molecules / gases represents only a small part of the total components. To be selective and specific for a particular target, the sensitive element is made with a probe attached to the surface of the biosensor by chemical bonds. These probes exploits the high affinity towards a specific target. For example, in the case of a protein detection, the probe is typically an antibody and the target is the specific antigen.

### 1.2.2 Transducer

The transducer is the second main component of a biosensor. This part is typically in contact with the sensitive element and ideally give information not only for the quality of the recognition event, but also for the quantity of the target / probe binding events. The type of transducer used will decide the application of the sensor. Different methods of transduction can be categorized depending on the physical property exploited for the recognition event, such as electro-chemical (potentiometric, amperometric, impedance, conductometry), electrical, piezoelectric, galvimetric and pyroelectric, nano-mechanichal, acoustic or optical. During this Chapter, I will focus only on optical biosensor category. This type of biosensors can be classified into two main parts: labeled and label-free.

#### 1.2.2.1 Label-based bio-sensing

In this case of labeled-based optical biosensors, the recognition event is indirectly measured, the target molecules interacting beforehand with a marker molecule for the detection. A marker / label is defined as any external molecule that is chemically / temporarily attached to the targeted molecule. It is used to transmit information from the molecular recognition event that occurred at the surface of the sensor. Labeling a molecule can be done by various methods (fluorescent, chemiluminescent, quantum dots etc). As example, fluorescent labeling allows the detection of the targets by exploiting their optical properties. Fluorescence labels are currently available in many forms and can be detected to any wavelength of the visible range, UV or IR. The labeling process requires a preparation step prior to detection. This implies that the biological solution, where the targeted molecules are found, will experience reactions that can alter the natural behavior of the targeted molecule. Another problem that can be encountered is the bleaching phenomenon or the decrease in the luminescence signal intensity due to the multiple tests performed. These reactions are unwanted for the real-time quantitative measurements. The specificity of the attachment to the targeted site of a molecule is another challenge. The labels may interact with other compounds of the analyte solution, leading to a misinterpretation of the result. The possibility that the binding site of the target molecule to be occupied by another compound will lead to a false positive result of the measure. Despite all these drawbacks, biosensors that uses markers are currently a mature field, with the detection protocols that have been well established during the years, with technologies that allows low limit of detection (fg / ml) ( [2, 3]).

#### 1.2.2.2 Label-free bio-sensing

A second type of biosensors is the label-free method, where the optical detection measures the signal directly from the molecular interaction target / probe. The detection procedure is simplified, without any pre-treatment of the biological solution. Gas detection sensors are possible using this class of biosensors. Kinetic studies can be done in real-time, without labeling the target molecules. The label-free detection can be obtained by measuring the refractive index change related to biological recognition event at the surface of the biosensor. The index variation is directly related to the concentration or surface density of the targeted molecule present on the sensitive layer.

## 1.3 Optical label-free biosensors for bio-detection

The technological progress accomplished in fabrication and also better understanding of physical phenomenon in photonics contributed to the improvement of sensor performances,

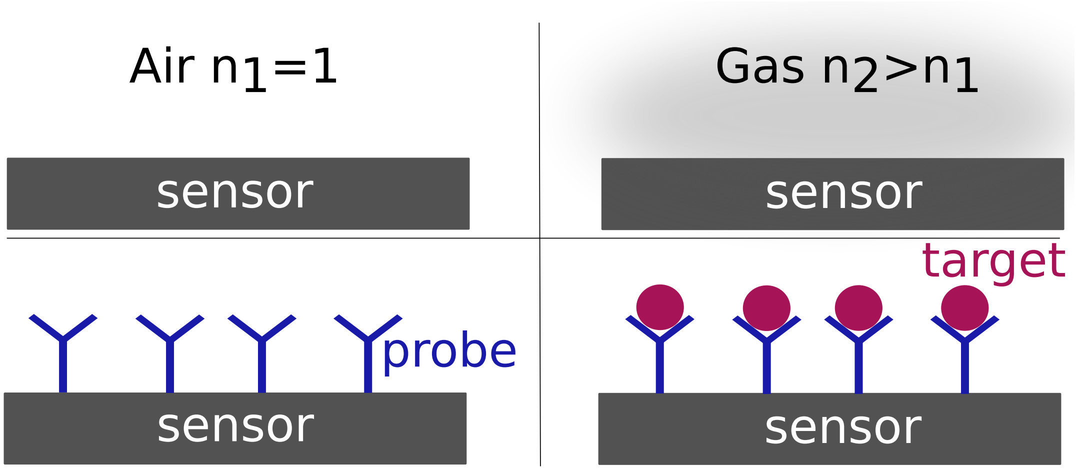

Figure 1.1: Top : global refractive index change detection; Bottom : surface refractive index change related to specific recognition event between probe (blue color) and target (red color) deposited on the surface of the optical sensor, which will locally modify the refractive index.

especially in the light-matter interaction, sensor miniaturization and integration in compact devices. As consequence, better sensitivities and limit of detection are obtained, with shorter detection time, ease of manipulation and lower cost.

### 1.3.1 Working principle

The working principle of an optical label-free sensor is based on the change of one of the light properties, once it make contact with the targeted element. There are multiple detection methods available, such as exploiting refractive index changes, absorbance or non-linearity properties. Further we are interested only on the optical sensor based on refractive index changes.

One can distinguish two categories of optical refractive index sensors, as illustrated in Fig. 1.1. The first type of biosensors are capable to measure the global refractive index change of the environmental medium (gas or liquid), as example the refractometers. The second type, more frequently encountered, are the optical biosensors are based on the configuration represented in the bottom part of Fig. 1.1, where the surface events are superimposed over the global refractive index change. Insofar, as the electric field is located at the surface of most of the sensors, a local refractive index variation induced by a surface binding event, i.e. probe / target recognition event is detected by the transducer. In order to have a specific recognition, the sensor's surface is functionalized with bio-recognition molecules (probes). Ideally, the sensor will detect refractive index changes related only on the molecular binding events.

## 1.3.2 Performances of a biosensor

Various configurations of refractive index biosensors were proposed and a definition of a general figure of merit (FOM) to define the performances of the biosensors is not trivial, knowing that the performances of different technologies rely on a multitude of factors. Firstly, the optical characteristics of the transducer are taken into account, such as the quality factor (Q) or the intensity in the reflection or transmission spectrum. Secondly, the quality of the probe layer for bio-recognition and its affinity to the target molecules. It can vary for the similar sensors with the same optical characteristics, depending on the transducer material, i.e. protocol efficiency for surface functionalization. A third factor is the optical setup type used for measurements, setup that will introduce noise to the measured signal. The biosensor performances are characterized by a series of performance parameters. In this Chapter, I will describe those parameters that are suitable for the proposed design.

### Bulk sensitivity

The sensitivity corresponds to the variation of the measured signal related to a refractive index change of the whole environment :

$$\mathrm{S}_\lambda = \frac{\mathrm{d}\lambda}{\mathrm{dn}} \tag{1.1}$$

where $\mathrm{d}\lambda$ is the wavelength shift of the resonance.

This expression is valid for a various types of biosensors based on resonators, such as ring resonators, photonic crystals (PhC) or localized surface plasmon sensors. In all the presented cases, the sensing is related to the frequency shift of a resonant mode ([4]), expressed in nm per refractive index unit (RIU). Typically, the shift is detected by transmission or reflection measurements.

In the case of measurement of an angular spectrum, a refractive index variation can also induce an angle shift in the reflectivity or transmission spectrum, as in some cases of SPR and PhC. In this case, the sensitivity is expressed as :

$$\mathrm{S}_\theta = \frac{\mathrm{d}\theta}{\mathrm{dn}} \tag{1.2}$$

where $\mathrm{d}\theta$ is the angular shift of the resonance.

The bulk sensitivity is usually important for device calibration, where known refractive index changes are induced to the sensor environment by varying the temperature or using known mixture of water and ethanol for example. Also, this performance parameter can be useful when the target objects are bigger than the exponential tail of the optical mode (i.e.

cell detection).

### Surface sensitivity

A biosensor is designed to detect molecular recognition events which take place at the surface of the biosensor. Ideally, the surface sensitivity is related only on probe / target molecular bindings. Is not trivial to define an universal quantity reflecting the surface sensitivity for all types of optical biosensors although this surface sensitivity can, in some cases, be theoretically related to the bulk sensitivity.

### Resolution

The resolution (R) of a sensor is the minimum variation value that can be accurately measured. This parameter is important when the detection is performed for small target concentrations. It depends mainly on the transducer, the chosen detection method, the signal-to-noise ratio (SNR) or data treatment.

The resolution is also strongly influenced by the intrinsic shape of the measured signal. The ability to accurately distinguish between two different signals depends on the amplitude of the measured shape and its width, which depends in general mainly on the quality factor of resonant mode.

## Figure of merit

In the case of the optical biosensors, the figure of merit is often introduced as the product of $\mathrm{Q} \times \frac{\mathrm{d}\lambda}{\mathrm{dn}}$ or $\frac{\mathrm{d}\theta}{\mathrm{dn}} \times \frac{1}{\delta\theta}$ for an angular measurement, which is the sensitivity multiplied the sharpness of the detected mode in the reflectivity or transmission spectrum. As mentioned before, the FOM depends on multiple factors. Nevertheless, the FOM can be considered as a good indicator when describing the expected performances of a sensor. The better the sensor performances, the higher the FOM value.

### Limit of detection

The sensitivity alone does not adequately measure the performances of a sensor. The limit of detection (LOD), that is the smallest refractive index shift that can be precisely and accurately measured, is often mentioned when the performances of a device are indicated. It can be defined as the product of the sensitivity multiplied the resolution of the sensor :

$$\mathrm{LOD} = \mathrm{S} \times \mathrm{R} \tag{1.3}$$

The limit of detection must not be confused with the sensitivity of the biosensor because it depends at the same time on the sensitivity and also on the detector used in optical setup. The LOD is given to evaluate the performances of a biosensor associated to a measuring optical setup. The smaller the LOD value, the more sensitive is the association.

## 1.4 Photonic crystals for optical biosensors

The optical technologies available for bio-sensing are numerous. This Chapter has not the scope to list and detail all different types of optical biosensors for bio-detection, different reviews establishing this part ([5, 6, 7, 8, 9]). Instead, we will concentrate on the properties of PhC and their application for biosensing. Firstly proposed by E. Yablonovitch and S. John in 1987 as an analogous of semi-conductors for optical field ([10]), photonic crystals are the building block of the proposed design in this thesis, for bio-sensing purpose. In addition to the purpose used here, the PhC are of great interest in applied photonics and telecommunications, signal treatment or non-linear optics. In the next paragraphs I will present a few basic properties of the PhCs, followed by a classification from the type of optical modes of interest and a comparison with the surface plasmon resonance (SPR), which is the reference technology in terms of label-free optical detection. The materials used for device fabrication will be also discussed.

### 1.4.1 Optical properties : Control of Electromagnetic Waves through photonic crystal

A crystal is a periodic arrangement of atoms or molecules. It uses a pattern formed from atoms or molecules that is repeated in space, named lattice. This type of periodic arrangement offers to an electron the possibility to propagate through it or not and the conduction proprieties of the crystal will depend from the crystal components and also from its lattice geometry.

Electrons propagates as waves, and if they match several criteria, they can travel through the periodic potential without scattering. Nevertheless, waves can be prohibited to propagate inside the crystal within certain energies ranges in certain directions, phenomenon known as gaps. If the prohibition extends to all possible propagation directions, the phenomenon is known as a complete band gap ([11]).

In optics, by analogy with the atomic crystal from solid state physics, is the photonic crystal, in which the atoms or molecules are replaced by macroscopic media with differing dielectric constants. The periodic potential is replaced by a periodic dielectric function (a periodic index of refraction).

If the dielectric constants of the materials in the crystal are different enough and if the

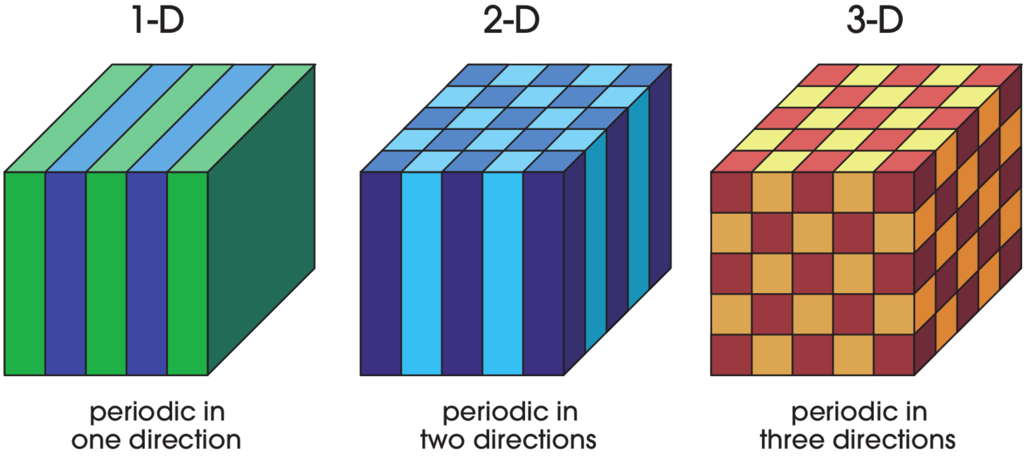

Figure 1.2: Example of one-, two- and three-dimensional photonic crystals. Different colors indicates material with different dielectric constants ([11])

light absorption by the materials is minimal, then the light refractions and reflections from all the interfaces can produce the same phenomena for photons (known as light modes, bands or resonances) as the atomic potential produces for electrons. Band diagrams are the representation of these phenomena and consists in the frequency evolution of the modes as a function of the wavevector and the direction of light propagation. They give important information necessary to design the photonic crystals, such as the geometry architecture oriented for sensing.

The refractive index, depending on the number of directions in which the pattern is repeated, lead to one-dimensional (1D), such as Bragg mirrors, two-dimensional (2D), as studied during this PhD work, and three-dimensional (3D) structures, such as opals (Fig. 1.2).

Light propagation in a photonic crystal obeys Maxwell equations. One considers the propagation within a mixed dielectric medium, linear, isotropic, free or charges or currents, without time variations of dielectrics properties or losses and with $\mu_0 = 1$.

Using a time dependence in $e^{(-i\omega t)}$, Maxwell equations become:

$$\boldsymbol{\nabla} \times \mathbf{E} - \mathrm{i}\, \omega\, \mu_0\, \boldsymbol{H} = 0 \tag{1.4}$$

$$\boldsymbol{\nabla} \times \boldsymbol{H} + \mathrm{i}\, \omega\, \epsilon_{\mathrm{o}}\, \epsilon_{\mathrm{r}}(\mathrm{x},\mathrm{y},\mathrm{z})\, \boldsymbol{E} = 0 \tag{1.5}$$

$$\boldsymbol{\nabla}.\, [\epsilon_{\mathrm{r}}(\mathrm{x},\mathrm{y},\mathrm{z})\, \boldsymbol{E}] = 0 \tag{1.6}$$

$$\boldsymbol{\nabla}.\, \boldsymbol{H} = 0 \tag{1.7}$$

where $\boldsymbol{E}$ and $\boldsymbol{H}$ represents the electric and magnetic fields, respectively. $\epsilon_0$ and $\mu_0$ represents electric and magnetic permittivity of vacuum respectively and $\epsilon_{\mathrm{r}}(\mathrm{x},\mathrm{y},\mathrm{z})$ denote the relative dielectric permittivity of the crystal.

In the following equations one can consider that the fields constitute physically acceptable solutions of Maxwell's equations. Combining eq. 1.4 and eq. 1.5 results in:

$$\frac{1}{\epsilon_{\mathrm{r}}(\mathrm{x},\mathrm{y},\mathrm{z})}\boldsymbol{\nabla}\times(\boldsymbol{\nabla}\times\boldsymbol{E})-\frac{\omega^2}{\mathrm{c}^2}\boldsymbol{E}=0 \tag{1.8}$$

$$\boldsymbol{\nabla}\times\left[\frac{1}{\epsilon_{\mathrm{r}}(\mathrm{x},\mathrm{y},\mathrm{z})}\boldsymbol{\nabla}\times\boldsymbol{H}\right]-\frac{\omega^2}{\mathrm{c}^2}\boldsymbol{H}=0 \tag{1.9}$$

with $\mathrm{c}={}^1\!/\!\sqrt{\epsilon_o\mu_o}$. The propagation eq. 1.8 and eq. 1.9 are to be considered in the sense of distributions, meaning that these equations include the boundary conditions at the interfaces of the different materials, in this case they include the continuity of the tangential components of the electric and magnetic fields([12]).

Given the periodicity of the $\epsilon_{\mathrm{r}}$, the Bloch-Floquet theory applied to eq. 1.9 allows to obtain solutions, as described in equation ([11]) :

$$\boldsymbol{H_k}=\boldsymbol{u_k}\cdot\mathrm{e}^{\mathrm{ik}} \tag{1.10}$$

where k is a wave vector of the first Brillouin zone and $\mathrm{u_k}$ has the same periodicity as the relative dielectric permittivity of the crystal and is named Bloch mode. They are solutions of the equation:

$$(\boldsymbol{\nabla}+\mathrm{i}\boldsymbol{k})\times\left[\frac{1}{\epsilon_{\mathrm{r}}(\mathrm{x},\mathrm{y},\mathrm{z})}(\boldsymbol{\nabla}+\mathrm{i}\boldsymbol{k})\times\boldsymbol{u_k}\right]-\left[\frac{\omega(\boldsymbol{k})}{\mathrm{c}}\right]^2\times\boldsymbol{u_k}=0 \tag{1.11}$$

with $\left(\frac{\omega(k)}{c}\right)^2$ appearing as the eigenvalues of the hermitian operator :

$$(\nabla+\mathrm{ik})\times\left[\frac{1}{\varepsilon}(\nabla+\mathrm{ik})\times.\right] \tag{1.12}$$

Solving the eq. 1.11 allows to determine the discrete set of $\omega(\mathrm{k})$.

### 1.4.2 Structure design arrangement and its properties

A two-dimensional photonic crystal is periodic along two of its axes (x and y) and homogeneous along the third one (z), as presented in Fig. 1.2. In our case, the dielectric is not strictly constant along z direction due to the finite thickness of the structure (Fig. 1.3 a). The modes of the structure are confined in this direction by total internal reflection due to the high refractive index contrast between the slab and its surroundings. In the Transverse-electric (TE) case, the $\mathrm{E_x}$ and $\mathrm{E_y}$ components of electric field are non zero in the

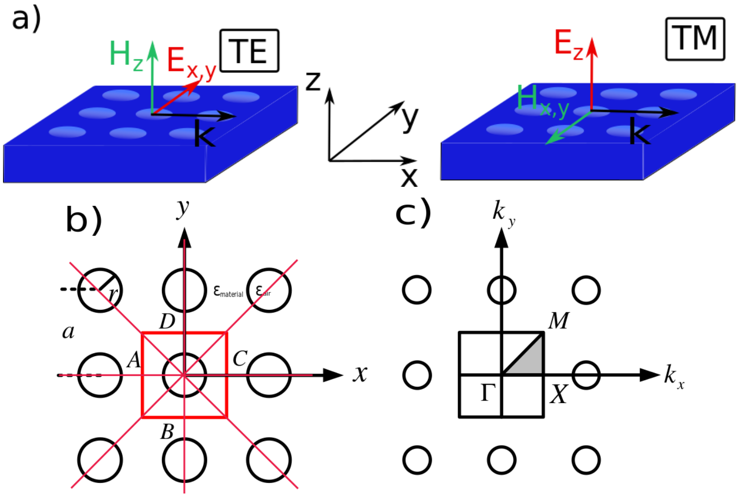

Figure 1.3: a) Two-dimensional photonic crystal with squared lattice arrangement composed from air holes in material for TE and TM polarization; b) Fundamental lattice cell representation (ABCD red square) and it's axes of symmetry (red lines); c) the corresponding reciprocal lattice with irreducible Brillouin zone (the gray zone defined by Γ, X and M points, which represents 1/8 of the first Brillouin zone) ([13])

$(x, y)$ plane of symmetry of the structure, while the $H_x$ and $H_y$ are zero in the same plane. For the Transverse-magnetic (TM) case, which is symmetrical opposite, the $H_x$ and $H_y$ field components are non-zero and the $E_x$ and $E_y$ are zero in this plane.

**Irreducible Brillouin zone** 2D photonic crystal can be realized in the (x,y) plane with arrays of nano-pillars or holes in material, arranged in different forms, such as triangular, squared or hexagonal lattices. In Fig. 1.3 a) is represented a network of square lattice of circular air holes (used in this PhD thesis). The first Brillouin zone is also square, as depicted in Fig. 1.3 c), making analogy easier. Calculating the band diagram of this structure allows to have rich information on the optical properties. Normally, the band diagrams have to be simulated in all possible directions inside the photonic crystal. Actually, thanks to symmetries of the crystal (Fig. 1.3 b), the calculation is restricted to the first irreducible Brillouin zone, as shown in Fig. 1.3 c). The first Brillouin zone can be expressed as the region of the reciprocal space composed by the points which are closer to the origin than to any other vertex of the periodical lattice ([12]). In the presented case, the structure presents six axes of symmetry (Fig. 1.3 b) red lines), which can be deduced from one to another through rotations of $\pi/4$. The reciprocal lattice presents a square symmetry and the first Brillouin zone is bounded by $-\pi/a < k_x, k_y < \pi/a$. The k wavevector values that will be expressed are represented by the gray triangle Γ X M from Fig. 1.3 c), with two edges of equal length $\pi/a$ which represents the irreducible Brillouin zone in the reciprocal space ([12]).

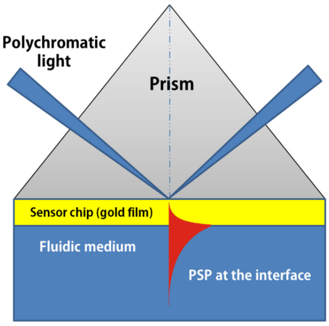

Figure 1.4: SPR working principle ([15])

### 1.4.3 Comparison with Surface Plasmon Resonance

Since the SPR is one of the well established techniques in the domain of optical biosensors, I will briefly present the working principle of the method, followed by a comparison with several examples of PhC technologies. Extended discussions and comparisons of different proposed technologies can be found in those reviews [14, 15, 16, 17].

The surface plasmon resonance is the resonant oscillation of conduction electrons which occurs at the interface between the materials, one with the real part of its permittivity positive and the other one with the real part negative, such as between a dielectric material and a metal (gold or silver in general), upon light injection. At a certain incidence angle, part of the incoming light energy couples with the electrons in the metal surface layer, which then move due to excitation ([15]). The electron movements are named plasmon, and they propagate parallel to the metal surface. There are multiple SPR sensing configurations, such as plasmon excitation by means of a prism ([18]) or optical fibers ([19]). In the prism case, the incident light is injected through a high refractive index glass prism in the so called Kretschmann configuration of the attenuated total reflection (ATR) method (Fig. 1.4). For a certain incidence angle, a resonant dip in the reflection spectrum appears when the propagating wave inside the prism is phase-matched to the surface plasmon waves at the metal-air interface. When a small refractive index variation of the environmental medium occurs due to a molecular recognition event, the coupling conditions will change. Since the position of resonance dip is determined by the phase matching condition, the resonance dip is now associated with a different surface plasmon mode at a different parallel wavevector ([4]). This multi mode nature of SPR sensors is the reason for the extraordinary sensitivity values obtained by this method (the entire surface plasmon dispersion relation representing a continuum of modes with different modes having different wavevectors).

The SPR method gives good sensitivity values and measures in real time molecular interactions, thus the method started to be commercialized by various companies, such as Biacore system from GE Healthcare ([20]). Typical LOD for SPR systems are as low as $10^{-6} \sim 10^{-7}$ RIU. However, this method is not well suited for every possible application. For the cases where the detection of large quantities are wanted (bacteria or cells), the evanescent field penetrates the environmental medium only for a few hundreds of nanometers, insufficient in the mentioned cases. Another limitation of the SPR method is the difficulty to differentiate between a bulk variation from a surface refractive index variation although several techniques are available to overcome this limitation.

### 1.4.4 Types of PhC

The label-free optical biosensors based on PhC can by classified in two classes by the type of the targeted modes to detect, namely the devices based on PhC micro-cavities and based on guided mode resonances (GMR).

#### 1.4.4.1 PhC cavities

As mentioned in the paragraph 1.4.1, one characteristic of the PhC is the photonic band gap (PBG), where the propagation of the light will be prohibited for that frequency range. However, like in the semiconductor case, the existence of a defect in the crystal periodicity will make possible the apparition of permitted states, named defect modes, inside the PBG. The creation of a defect consists in locally breaking the periodicity of the crystal by adding or removing dielectric material. In the case of hole networks for 2D PhC, the defect mode can be obtained by removing holes, changing their radii or slightly shifting one or multiple holes, which make possible the presence of strong confined electromagnetic field and small mode volume ([21]). In the reflectivity or transmission spectrum, this defect mode is translated to a narrow-band dip or peak within the band gap, as presented in Fig. 1.5. All the types of PhC cavities sensors rely on the measurement of the evanescent tail of the PhC mode that interacts with the environmental medium, which provides the refractive index sensing method.

Typical PhC cavities can be classified into :

- $L_n$ cavities type represented by line defects, where n is the number of adjacent holes removed from the periodic lattice for localizing the light along a line (Fig. 1.5 a)
- heterostructure cavities, where hole size and / or period is changed along a line defect (Fig. 1.5 b)
- nanobeam cavities, where a row of holes is realized and a hole removal radii change or position change is performed (Fig. 1.5 c)

Photonic crystal cavities exhibit a strong spatial and temporal light confinement (which translates into high quality factors Q and small mode volume). The sensing volumes are

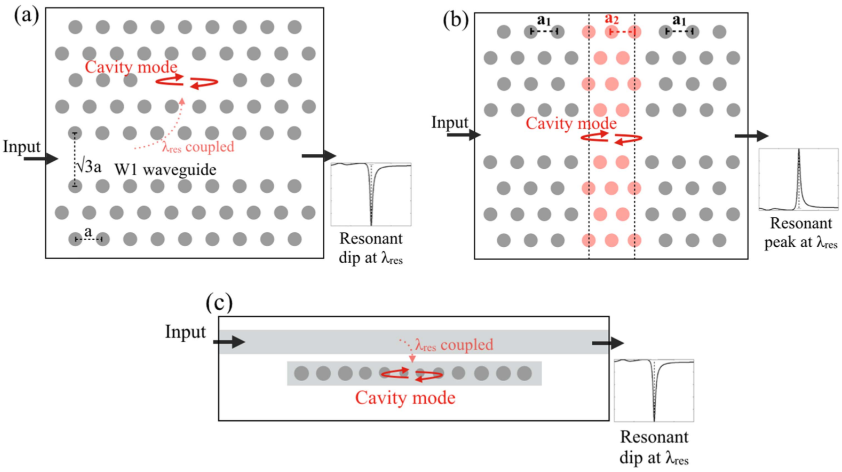

Figure 1.5: Different types of PhC cavities([14])

very small, which is practical for integration in ultra compact miniaturized devices, with the possibility for multiplexing and arraying.

Insofar, as a small variation of the refractive index occurs on the surface of a PhC cavity, the targeted mode will experience a small frequency shift. This property can be used as a transduction method and justify the choice of PhC cavities as optical detectors. The spectral position $\lambda_{\text{res}}$ of the resonance of the cavity can be used as reference. Thus, the measurement of the spectral position $\Delta\lambda_{\text{res}}$ is the result of a refractive index change $\Delta$n that took place on the surface of the PhC cavity due to a molecular recognition event, as shown in Fig. 1.6, with typical values listed in Table 1.1.

The first 2D PhC cavity biosensor was proposed in 2004 by Chow *et al* where they detected a variation of 0.002 of the refractive index with a cavity having a Q factor of around 400 ([22]). They obtained a sensitivity of 183 nm /RIU with measurement of a glycerol : water mixture.

Falco *et al* used a waveguide and added a slotted cavity ([23]), configuration that reached the highest sensitivity values reported for 2D PhC cavities of 1500 nm/RIU with a Q of $5 \times 10^5$ and a LOD of $7 \times 10^{-6}$ RIU. This design is based on a multi mode cavity, because such a sensitivity value cannot be possible for a single mode cavity, according to the formula of the perturbation theory, as I will explain in Chapter 2. Indeed, the slotted devices show very good performances in terms of sensitivity and LOD within the class of PhC biosensors, mainly due to the strong spatial confinement of the mode within the air slot and a large overlap of the mode with the sensing medium.

A comparison between the PhC cavities and SPR method is made in order to determine the interplay between the Q and the sensitivity values, properties that influence the final performances of a biosensor. In the review of Pitruzzello *et al* ([14]), the authors compared a nanobeam cavity with SPR method for DNA detection in analyte solution, with the

| Structure type | Analyte detected | Q factor | Bulk Sensitivity (nm/ RIU) | FOM ( nm / RIU) | LOD | References |
|---|---|---|---|---|---|---|
| 2D PhC cavity | Glycerol : water | $\sim 400$ | $\sim 183$ | $7.3 \times 10^4$ | \ | [22] |
| 2D PhC waveguide | Glucose solutions | 4000 | 1538 | $6.1 \times 10^6$ | $7 \times 10^{-6}$ RIU | [23] |
| 2D PhC waveguide | ssDNA | \ | \ | \ | 20 nM | [24] |
| SPR | ssDNA | $\sim 10$ | $\sim 10^3$ | $\sim 10^4$ | 50 nM | [25] |

Table 1.1: State of the art of different biosensors based on PhC cavities

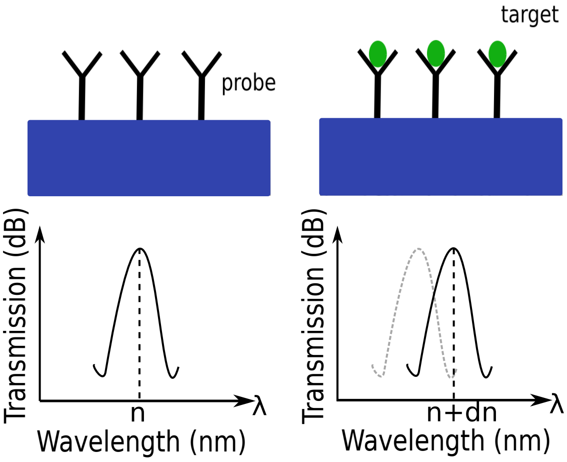

Figure 1.6: Sensing principle of the PhC optical biosensor with an initially functionalized surface on the left part, which leads to a coupling on incoming light to a resonance mode of the diamond detected in the transmission spectrum. In the right part is depicted the biological recognition event, which induces a change in refractive index and implicitly a spectral shift

complementary DNA strains immobilized on the surface. In [25], they detected single strand DNA with SPR imaging, obtaining an LOD of 50 nM. In the case of the PhC waveguide proposed by Toccafondo *et al* ([24]), they detected also single strand DNA by tracking the spectral position of the mode, obtaining a similar LOD of 19.8 nM. Even though the geometries are different, the LOD is very similar. To improve the LOD for PhC cavities, the functionalization protocols and sources of noises needs to be optimized and minimized, respectively.

Even though the PhC cavity based optical biosensors possess similar or better LOD than the SPR method, a very few PhC devices are commercially available ([26]), whereas the SPR are commercialized since the 1980s (GE Healthcare). The SPR is the reference technology when referring to optical label-free biosensors. Its relative ease of use and fabrication simplicity gained over the other proposed devices. However, the PhC fabrication requires more complicated methods to be realized, in some cases electron beam lithography can be required or nanoimprint technology.

#### 1.4.4.2 Guided mode resonances based optical biosensors

A second class of PhC biosensors is guided mode resonance (GMR) based optical label-free biosensors. This type of device exploits the in-plane resonant modes of the structure, that can be probed with collimated light from the outside, often at normal incidence. The ability to couple directly to the GMR is an attractive characteristic of the configuration because of the easiness of interfacing with light sources and detectors in an efficient way.

These PhCs operate like a waveguide but also scatter light coherently like a grating

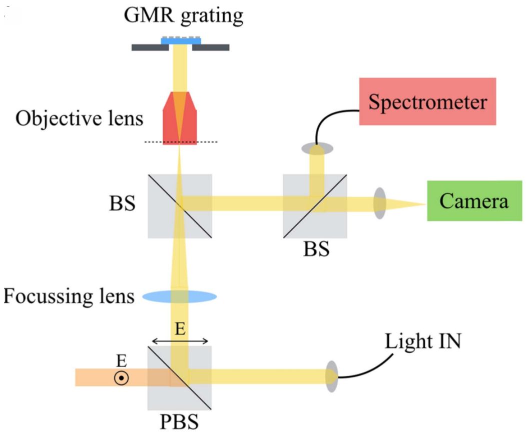

Figure 1.7: Typical optical setup for measuring reflection of a GMR based label - free optical biosensor at normal incidence. PBS represents the polarizing beam splitter which ensures polarization section. BS is a normal beam splitter ([14])

when light propagates, leading to a sharp angular or spectral signature that appears in their reflectivity spectra. Such angular or spectral signature appears when there is a phase matching between the incident wave with the guided mode resonance. Phase matching occurs when the parallel component to the slab of the wavevector of the incident collimated light equals the wavevector of the guided resonance, given by the dispersion curve of the guided resonance mode. In the case of a refractive index change, e.g. when a molecular binding occurs at the surface of the PhC, the dispersion curve is shifted vertically towards the lower frequencies ([11]). This results in an angular or spectral shift of the GMR, since the phase matching occurs at a different wavevector. This shift represents the sensing property of this type of biosensors.

The bases of this optical biosensor configuration were established by Magnusson ([27]) and Cunningham ([28]), where they opened the path for GMR based configuration for sensing applications. They obtained detection of streptavidin concentrations down to ng / ml.

Typical optical setup for GMR detection is shown in Fig. 1.7. The typical sensitivity values are modest compared to the PhC cavities values (around 100 nm / RIU and a LOD in the range of $10^{-5}$ RIU), which is considered as a drawback of this kind of sensor ([14]) (Table 1.2).

Various configurations based on GMR detection are reported in the literature, using different strategies to maximize their performances. To name several examples, El Beheiry *et al* ([29]) simulated a silicon nitride suspended membrane with a square array of circular holes, structure completely immersed in an analyte solution. An impressive sensitivity value of $\sim$ 800 nm / RIU was found, mainly related to the fact that the device uses both the top and the bottom surfaces of the structure as sensing regions. A similar configuration was experimentally performed by Huang *et al* ([30]), where the authors obtained a bulk sensitivity of 510 nm / RIU, with a Q of the targeted GMR only of about 100.

Magnusson proposed a device that supported both TE and TM polarization ([31]). The two GMRs shown different modal distributions and the detection of both modes gave two sets of measured data. This configuration allows to differentiate between any background index or density fluctuations from the recognition events, providing a self-referencing technique. Fitting the acquired data from measurements and comparing them with the simulations, the author estimated both the thickness and the refractive index of the absorbed layer from a single experiment, obtaining a LOD of 156 nm / ml.

Configurations that are based on angular spectrum detection of the GMR experience sensitivity values of 40.92 ° / RIU in the case of 1D PhC ([34]) or 65 ° / RIU for 2D PhC ([33]). Meanwhile, using SPR method, higher sensitivities were reported using diverse strategies, such as 237 ° / RIU ([35]) or 535.9 ° / RIU ([36]).

#### 1.4.4.3 Materials and integration in opto-electronic circuits

The different designs proposed to obtain the highest sensitivities and lowest LOD are based on different fabrication technologies and different materials. Integration of PhC in opto-electrical circuits began about two decades ago, with the 1D PhC type being the most numerous, because of the relative easiness of realization. In the last years, 2D PhC experienced a considerable growth, mostly from the fact that technological processes to fabricate this type of structure became more mature, offering higher performances for the device because of the better light confinement. The fabrication of 3D PhC type structures is still challenging for most of the materials.

PhC fabrication requires materials that are transparent at the targeted wavelength range and needs to have the highest dielectric permittivity possible to strongly confine the electromagnetic field. Thereby, in general, the materials used are semiconductors, such as GaAs, InP or AlN ([37]), and silicon, with the configuration Silicon-On-Insulator (SOI). More recently, realization of PhC on organic compounds and polymeric materials, such as PMMA ([38]), offers a new path for optical sensors.

However, there are always different limitations in order to achieve higher performances of the devices. One limitation is represented by the surface functionalization efficiency to a specific target, where most of the materials need an improvement of the functionalization protocols in order to lower the non-specific recognition events. A bottleneck of these devices is the development of surface chemistry. In order to have a strong surface functionalization with probe molecules, it is often recommended to have a covalent binding to the surface ([39]) instead of physical adsorption.

In this context, the change towards new materials was needed, in particular to the

| Structure type | Analyte detected | Q factor | Bulk Sensitivity | FOM ( nm / RIU) | LOD | References |
|---|---|---|---|---|---|---|
| GMR 2D PhC | Glycerol : water | $1.6 \times 10^5$ | $\sim$ 800 nm/ RIU | \ | $1 \times 10^{-7}$ RIU | [29] |
| GMR 2D PhC | \ | 100 | 510 nm/ RIU | \ | \ | [30] |
| GMR 2D PhC | BSA; Streptavidin | $\sim$ 150 | 88 nm/ RIU | $1.3 \times 10^4$ | 1 ng / ml | [28] |
| GMR 2D PhC | Avidin | $\sim$ 200 | 88 nm/ RIU | $1.7 \times 10^4$ | 1 µg / ml | [32] |
| GMR 1D PhC | TNF-α Calreticulin | \ | \ | \ | 156 nm / ml | [31] |
| GMR 2D PhC | \ | \ | 65° / RIU | \ | \ | [33] |
| GMR 1D PhC | \ | \ | 40.92 ° / RIU | \ | 50 fg / ml | [34] |
| SPR | \ | \ | 237 ° / RIU | \ | \ | [35] |
| SPR | \ | \ | 535.9 ° / RIU | \ | \ | [36] |

Table 1.2: GMR optical biosensor performances

compatible materials with biomolecules. One alternative material can be diamond, which posses physico-chemical properties desired for an optical biosensor. In the following part I will present some advantages in the use of this material compared to other materials.

## 1.5 Synthetic diamond

The performances of the optical biosensors are part related to the physico-chemical properties of the used material for sensing. Diamond as transduction material offers a good efficiency of surface functionalization, property desired for an optical label-free biosensor, which give an advantage compared to the other types of materials ([37, 38]).

Diamond is extremely stable in acid, basic or oxidant environments ([40, 41]) and also to corrosion ([42]). It posses a low thermal dilatation coefficient and does not create an native oxide on its surface, contrary to the majority of the semiconductors. These extraordinary properties give the possibility for the devices to detect in extreme conditions in various fields.

Due to its chemical inertia, diamond is tolerated by the human body, result expressed in multiple studies ([43, 44, 45]). In addition to the biocompatibility property, the path towards miniaturized implantable devices was opened.

Synthetic diamond is an attractive material for the biological interfaces, mainly for transduction applications. Various experiments showed the possibility to create stable bonds between the diamond surface and the probe molecules by covalent bonds ([46]). The termination of diamond surface can be modified (hydrogen, oxygen or fluorine termination) in order to diversify the types of molecules that can be bonded covalently on the surface ([47]).

Diamond is already used for other biosensor technologies, such as Surface Acoustic Waves (SAW), high energy radiation detection, radiation dosimeters, electrochemistry, optics or MEMS, all of the cited topics being found in the LCD group. In addition to that, the LCD laboratory has experience of the synthetic polycrystalline diamond growth and disposes of various Chemical Vapour Deposition reactors for diamond growth.

It is known that monocrystalline diamond offer better optical properties compared to polycrystalline type. Even with this advantage, the monocrystalline diamond is not used extensively in devices because of the small size samples that can be grown.

Very few groups are working for the realization of photonic structures based on diamond. Most of the concepts are realized onto monocrystalline diamond due to its superior optical properties regarding the polycrystalline one, which lead to the possibility of high quality factors (around 10000 measured in [48]). 1D PhC cavities ([49]) and 2D PhC cavities ([50, 51, 52, 53]) were realized in monocrystalline CVD diamond. The mentioned photonic structures are not designed for bio-detection purpose.

The use of diamond for GMR based optical biosensors does not demand high quality factors. This requirement guided us to the polycrystalline type for fabricating the proposed optical biosensor. In addition of the optical properties of the photonic crystal structures, the combination with the physico-chemical properties of diamond represents an asset for the proposed device.

The polycrystalline diamond was grown at the LCD laboratory, where samples up to 2 inch were fabricated with film thicknesses ranging from several hundreds of nanometers to a few micrometers.

Even if 2D PhC were realized since 2007 in polycrystalline diamond ([54]), the research on this material for optical field for biological detection was limited, mainly due to the fact that the surface roughness and the presence of grain boundaries lower the optical performances of the photonic structures. 2D PhC structures were reported in our group detecting at 1.55 µm wavelength, with a quality factor of 6500 ([55]).

The proposed design was optimized to detect at the limit of the visible wavelength range. The reasons of choosing this wavelength range are the availability of cameras on the market that are very efficient at low prices and inexpensive mono-mode laser sources. Also, water absorbs at the 1.55 µm wavelength, fact that limit the quality factor that can be achieved. From the fabrication point of view, the detection at visible wavelengths requires fabrication of smaller diamond structures, fact that renders the PhC realization more difficult. In addition to that, tunable laser light sources are very expensive at this frequency range, fact that requires a precision in fabrication at the nanometer scale. Detecting at the visible wavelengths is more challenging than working at the IR wavelengths due to smaller structure sizes that have to be fabricated.

## 1.6 Goals of the thesis

In this introductory Chapter, I presented the advantages offered by the label-free optical sensors compared with the labeled ones. The working principle of a refractive index optical biosensor was discussed and the main properties of a biosensor were exposed to describe their performances. Further discussions were focused on the use of photonic crystals as new technologies for optical label-free biosensors, which represents an alternative to the mature technology of surface plasmon resonance. A classification of PhC structures was done by the type of the targeted modes, namely the PhC based cavities and guided mode resonance based. Some examples of each type of PhC structures were mentioned, and their performances were compared with the SPR technology.

With the progress obtained in the last decades in silicon micro-fabrication, the majority of the proposed design are realized in silicon material. Though, some issues regarding the efficiency of surface functionalization of silicon are encountered, guiding the path to fabrication of optical biosensors on other materials, in particular technologies based on biocompatible materials. Therein, one candidate is represented by diamond as material. Photonic structures can be realized on diamond and its surface can be functionalized with probes experiencing covalent bonds with diamond, a desired property for the biosensors.

For this PhD thesis, I propose a new photonic crystal optical label-free biosensor based on guided mode resonances detection at the limit of visible range (800 nm), realized on polycrystalline diamond. This proposed biosensor is designed to overcome the performances reported in literature by diverse technologies, offering a sensitive device for molecular recognition events.

The conception of the proposed design is based on a series of numerical simulations for specifying the geometrical parameters for this type of structure in order to be sensitive at the refractive index variations. The realization of the calculated designs using clean-room micro-fabrication technologies represents another important aspect of this PhD thesis. The optimization of existing methods and the development of new techniques for realizing different device configurations proposed lead to the control of the various structure fabrication in the nanometer range in polycrystalline diamond, methods that can be applied for other purposes than photonics.

The fabricated biosensor was optically characterized in order to determine its performances. The results of the measurements of the fabricated devices are compared with the numerical simulations in order to verify the theoretical assumptions.

# Chapter 2

# Design of 2 D photonic crystals for bio-detection

## 2.1 Introduction

The goal of this thesis work is to realize a sensitive platform on 2D photonic crystals for the detection of biological species. In the Chapter 1 of the thesis, I presented a brief state of the art of technologies and devices related to the optical biosensor field based on photonic crystals. For better understanding the light behavior for this type of structures, there is a need to enter in details of PhC's optical properties. We propose in this work an innovative type of the photonic structure that combines properties of different proposed technologies from the literature. An explanation of physical phenomena that occur needs to be done, along with the geometrical parameters of PhC that influence the final performances.

Different optical structures are proposed to act as transducers for biosensors. The choice of 2D photonic crystals was done for their advantages, such as high quality factors, small surface area, compatibility with micro-electronics cleanroom fabrication and the possibility to control the light propagation inside the device, properties that are demanded for a biosensor. Using diamond as material makes the device more attractive for bio-sensing due to its optical properties, as well as its physico-chemical properties, such as the efficiency of surface functionalization and bio-compatibility. The possibility of growing polycrystalline diamond on large surfaces opens the path for production of thousands of biosensors on the same sample.

The 2D PhC pattern that we will propose was intended to be as simple as possible from the fabrication point of view. The biosensor design is optimized for detection of small refractive index changes, in order to realize a device that has a low limit of detection and high sensitivity values. Using this property, the structure is foreseen to have the best performances in the visible wavelengths.

In this Chapter will be presented the strategy used to optimize the performances of the proposed architecture. I will propose different designs for 2D diamond PhC biosensor based on different substrates and each of them will be described in detail and the performances of each design will be evaluated.

## 2.2 Photonic crystals for bio-detection

### 2.2.1 The effect of small perturbations

As presented in the Chapter 1, the field of optical label-free biosensors has increased in the last decade with application in different domains (healthcare, biology and medical research, chemical safety, environmental monitoring etc). The principle of optical biosensor consists in the variation of optical properties of a structure when the refractive index of the surrounding media varies. In other words, ideally, the light propagation inside the PhC is modified when a targeted species is detected on the surface of the structure. The binding of molecules induces a local refractive index change of the PhC, that will be visible on the dispersion relations. In general, the electromagnetic field is concentrated in the higher refractive index medium ($\mathrm{n} = \sqrt{\varepsilon}$), with a resonant mode at pulsation $\omega$. When a variation of the refractive index occurs, the dielectric function changes from $\varepsilon$ to $\varepsilon + \mathit{\Delta}\varepsilon$. Using the perturbation theory ([11]), the frequency shift $\mathit{\Delta}\omega$ of an optical mode of the structure can be obtained, as expressed :

$$\mathit{\Delta}\omega = -\frac{\omega}{2}\frac{\int \mathrm{d}^3\,\mathrm{r}\;\mathit{\Delta}\,\varepsilon\,(\mathrm{r}) \mid \mathbf{E}\,(\mathrm{r}) \mid^2}{\int \mathrm{d}^3\,\mathrm{r}\;\varepsilon\,(\mathrm{r}) \mid \mathbf{E}\,(\mathrm{r}) \mid^2} + \mathcal{O}(\mathit{\Delta}\varepsilon^2) \tag{2.1}$$

where $\omega$ and E are the pulsation and the electric field corresponding to the unperturbed eigenmode associated with the perfectly linear and lossless dielectric function $\varepsilon$. The error $\mathcal{O}(\mathit{\Delta}\varepsilon)^2$ can be neglected in the cases where $\mid \mathit{\Delta}\varepsilon \mid / \varepsilon < 1\%$, but for the configurations where the maximum refractive index changes are much less than 1%, the perturbation theory is nearly exact.

Using Eq. 2.1, in the case of 2D photonic crystal biosensor in which a refractive index variation $\mathit{\Delta}\mathrm{n}$ occurs, the volume integral in the numerator has nonzero contributions only in the perturbed regions. This variation is realized at the surface of the PhC due to a recognition event or at the environmental medium, when temperature or humidity change takes place. For example, it can be written $\mathit{\Delta}\varepsilon/\varepsilon \approx 2\mathit{\Delta}\mathrm{n}/\mathrm{n}$. Supposing that $\mathit{\Delta}\mathrm{n}/\mathrm{n}$ is the same in all the perturbed regions, one can obtain the following relation ([11]) :

$$\frac{\mathit{\Delta}\lambda}{\lambda} \approx -\frac{\mathit{\Delta}\omega}{\omega} \approx \frac{\mathit{\Delta}\mathrm{n}}{\mathrm{n}} \cdot (\text{fraction of} \int \varepsilon \mid \overrightarrow{E}(\overrightarrow{r}) \mid^2 \text{ in the perturbed regions}) \tag{2.2}$$

In other words, the relative frequency change is equal to the relative refractive index changes multiplied by the fraction of the electric field energy located inside the perturbed regions.

Typically, the target molecules are carbon-based bio-molecules with a refractive index of 1.5. They have higher refractive indexes than the analyte solution / water (n=1.33) or air (n=1). Binding of these molecules on the surface of the structure increases the refractive index of the structure, which in turn lowers the frequency of the modes.

Two classes of photonic crystal biosensors are proposed in the literature, namely devices based on PhC cavities or based on guided mode resonances (GMR). The first type have an in-plane approach for light injection or collection, and offers a high degree of spatial confinement, configuration that give the possibility for extreme miniaturization. Also, it comes with some disadvantages as well, one drawback being the difficulty to inject and to collect light in these small devices since optical fibers and microscope objectives need to be precisely aligned.

The second class of biosensors is GMR-based devices. This type exploits the in-plane resonant modes of the structure, with the interrogation from an out-of-plane radiation source. The ability to couple directly to the resonant modes is an attractive characteristic of the configuration because of the easiness of interfacing with light sources and detectors in an efficient way. In this PhD thesis, this class of PhC biosensors was studied, where the properties and performances of several proposed designs are presented and discussed.

Regarding a small variation of the refractive index near the structure, a frequency shift of the resonant modes will occur, property that can be used as a transduction method. The initial spectral position can act as the reference ($\lambda$). The shift measurement of the spectral position of the mode ($\Delta\lambda$) is related to the refractive index change ($\Delta$n) induced at the structure's surface, as shown in Eq. 2.2. The performances of a biosensor are characterized by different parameters, one of them being the sensitivity, measured in nm / RIU, where RIU is the refractive index unit. Each PhC is optimized to have the best configuration possible, but the highest sensitivities obtained in the case of a single mode structure are limited to a value smaller than $\lambda$/n, which typically translates to 1000 nm / RIU spectral sensitivity for 1550 nm wavelength or 533 nm / RIU for the 800 nm wavelength biosensors ([56]).

An idea for maximizing the spectral sensitivity of a dielectric-based structure was proposed by Fan et al ([4]). The authors start by describing the origin of the extraordinary SPR sensitivity values, i.e. the multi-mode nature of the sensing scheme. They showed that the same concept can be applied to a dielectric system, thus exhibiting similar extraordinary spectral sensitivity. The dielectric-based system proposed consist in a waveguide suspended above a prism with angular interrogation (as SPR technique), designed at 1550 nm wavelength. For this structure, they showed that the spectral sensitivity value can be enhanced by changing the incidence angle of the incoming probe wave to match the dispersion relation of a particular waveguide mode. They succeeded to increase by 28 times the spectral sensitivity value as compared to in-plane configuration of the same structure, thus finding similar values as in the SPR case.

We propose a new design of a biosensor where the dispersion relation of a targeted GMR match the properties of the incoming light. This concept is similar to the one proposed in [4]. The strategy involved in the biosensor design will be detailed in the next sections.

### 2.2.2 Proposed design

Integration of PhCs in opto-electrical circuits began about two decades ago. 3D PhC possess the best light confinement in all three directions. The fabrication of this type of structures is still challenging for most of the materials. Moreover, due to diamond hardness, it is difficult to realize structures at the nanoscale level with high accuracy and good reproducibility. For that, a 2D PhC was preferred, taking into account the technological processes involved during the fabrication.

The design of the device is based on guided mode resonances detection, where light from an external radiation source couples with GMR confined within the slab and exhibits a sharp feature in the reflection spectrum. In the literature, in general, collimated light is injected at normal incidence and the reflected or transmitted light spectrum in collected. Various configurations based on GMR detection are reported in the literature, using different strategies to maximize their performances (see Chapter 1 subsection 1.4.4.2).

The proposed design is based on the GMR detection. The GMR has the energy confined in the slab, but contrary to the truly guided modes or PhC cavity resonance, they can easily be coupled optically from the outside with collimated light. The schematic representation of the proposed biosensor is shown in Fig. 2.1 a). The device came with a series of changes referring to the classical configuration proposed in the literature. Firstly, the light detection occurs in the reflectivity spectrum, at a desired angle from normal incidence. Injecting and detecting at the normal direction to the surface limits the sensitivity values, as it will be explained later. This change in the injection and collection method offers the possibility to control two polar angles : the colatitude angle $\theta$ (angle from the surface normal direction), and the azimuthal angle $\phi$ (angle from x-y surface plane).

Another difference implies the detecting element. The detection of the incident light coupled with a guided mode of the PhC can be realized by two methods. The first one include light interrogation at a fixed angle with a spectrally broad source and a spectrometer as detector. This configuration will dispose of a spectral sensitivity, calculated in nm per RIU, as in the presented cases ([56, 31, 29]).

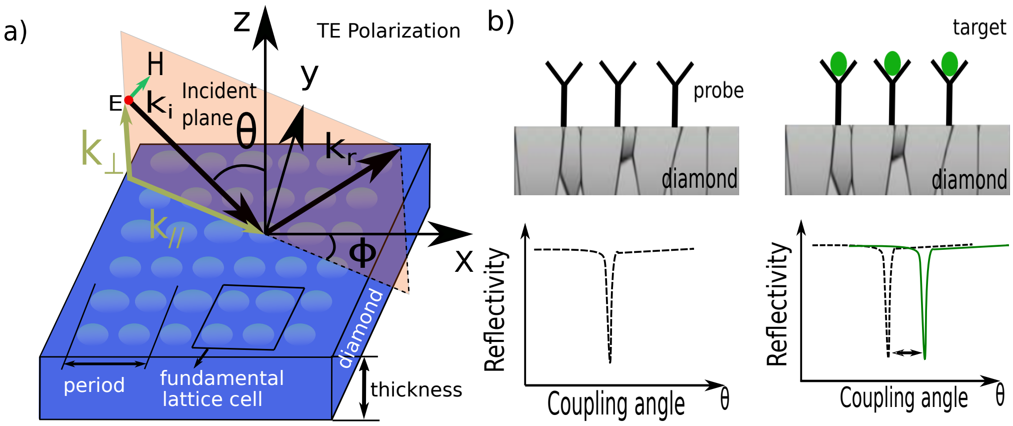

Figure 2.1: a) Schematic representation of the photonic crystal design with angular light injection at desired $\theta$ co-latitude angle and $\phi$ azimuthal angle for in-plane direction. b) Sensing principle of the proposed biosensor with an initial functionalized surface on the left part (black dashed line), which leads to a coupling on incoming light to a resonance guided mode of the diamond. In the right part is depicted the biological recognition event, which induces a change in refractive index and implicitly an angle shift (green line).

The second method involves the light injection from a single wavelength source, but angularly spread, and the detection of the coupled guided modes of the structure is performed by means of a camera. This configuration replaces the spectrometer by a camera and will dispose of an angular sensitivity, expressed in degrees per refractive index unit (°/ RIU). This configuration was preferred for the biosensor (Fig. 2.1 a) and the design of the diamond structure was chosen in such way that a targeted GMR to be found at a specific frequency for visible light detection. Using angular interrogation format, light can be injected to the structure at various $\theta$ angles and different directions regarding the PhC structure ($\phi$ angle). Having these specifications for the PhC proposed design, it will be possible to somehow overcome the sensitivity limits imposed by the in-plane configuration, as described by Eq. 2.2.

The goal of the designed structure is to inject light from a single wavelength source and to probe two different GMRs with different group velocities at different incident angles, which will give two sets of information regarding the recognition event on the device surface. In this manner, the penetration depth of each mode will be different, fact that would allow us to differentiate between surface and bulk refractive index variations. Further, I will detail the strategy involved for the design of the final optical biosensor.

When light is injected with a certain $\theta$ angle, the parallel wavevector is equal to :

$$\|\overrightarrow{k_{\|}}\| = \overrightarrow{\|k_i\|} \times \sin\theta = \frac{\omega \times \mathrm{n_{environment}}}{\mathrm{c}} \times \sin\theta \tag{2.3}$$

where $\overrightarrow{k_{\|}} = \mathrm{k_x}\overrightarrow{x} + \mathrm{k_y}\overrightarrow{y}$ is the wavevector into the (x,y) plane, $\mathrm{k_i}$ is the incident wavevector, $\omega$ is the normalized frequency, $\mathrm{n_{environment}}$ is the refractive index of the surrounding medium and c is the speed of light (Fig. 2.1 a).

The light coupling from the free-space with a leaky mode of the PhC structure occurs when there is a phase matching between the incident wave with the GMR of PhC. For a given fixed frequency of the light, there is a single particular $\theta$ angle at which the coupling occurs, as schematically illustrated in 2.1 b). In the reflectivity spectrum, this light coupling can be translated in an intensity decrease in the reflectivity at a particular $\theta$ angle (Eq. 2.3), depicted in dashed black line, which will serve as reference angle.

When a refractive index change takes place, e.g. due to a target / probe recognition event, the coupling angle shifts (green line from Fig. 2.1 b).

A light coupling to the GMR of the PhC occurs when the parallel component to the slab of the wavevector $\mathrm{k_{\|}}$ of the incident collimated light equals the wavevector of the GMR given by the dispersion relation curve of the GMR. In the black lines from Fig. 2.2 a) and c) are illustrated the dispersion curves of two different group velocities GMRs. The corresponding reflectivity spectra are shown in the black lines from Fig. 2.2 b) and d).

In the case of a molecular recognition event, the refractive index of the PhC structure will increase and therefore the dispersion curves are vertically shifted towards lower frequencies, according to the Eq. 2.2 (green lines in Fig. 2.2 a) and c). The frequency shift $\Delta\omega$ of the mode is of the same order in both cases (Eq. 2.2) because we can expect similar E field patterns, in particular if we consider two different regions of the same dispersion curves, but the coupling wavevector $(\mathrm{k} + \Delta\mathrm{k})$ will shift differently to couple at the same frequency.

This refractive index change will cause a change in the coupling angle $(\theta + \Delta\theta)$ since the phase matching occurs at different wavevector (green curves from Fig. 2.2 a) and c). In the reflectivity spectrum, this angle shift, depicted in green lines in Fig. 2.2 b) and d), represents the propriety of the structure to sense small variations of the refractive index.

This angular shift $\theta + \Delta\theta$, depends on the frequency shift $\Delta\omega$, but also on the group velocity $(\mathrm{v_g} = {}^{\Delta\omega}/_{\Delta\mathrm{k_{\|}}})$. A bigger $\mathrm{k_{\|}}$ wavevector shift (Fig. 2.2 c) translates to a bigger angle shift on the detector (Fig. 2.2 d), leading to the possibility to detect smaller refractive index variations .

In the case of small perturbations, we can consider frequency and wavevector shifts as local and assimilate dispersion curves to straight lines with the slope equals to $\mathrm{v_g}$. Furthermore, we can expect that the the dispersion curves before and after the perturbation caused by molecule binding events are parallel lines since the modes are only very slightly perturbed, as in Fig. 2.2 a) and c).

It can be observed that in the case presented in Fig. 2.2 c), the mode with low $\mathrm{v_g}$ is experiencing a larger wavevector shift $(\Delta\mathrm{k_{\|}} = {}^{\Delta\omega}/_{\mathrm{v_g}})$, that implicitly will induce a larger angle shift, when a refractive index change occurs, in order to couple at the same fixed

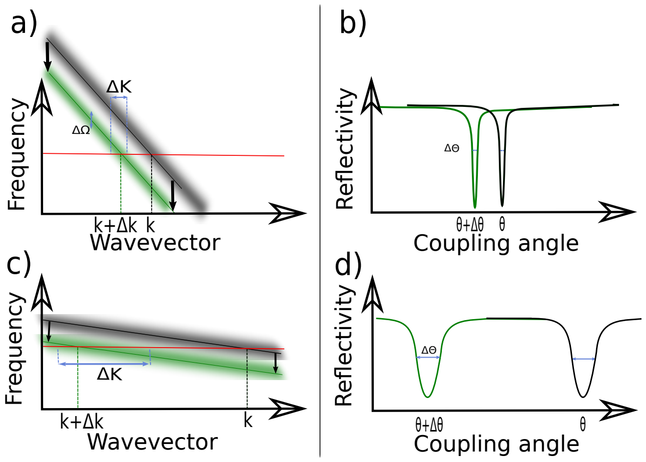

Figure 2.2: a) Schematic band diagram showing the dispersion curves of the resonant mode (the black lines) and in the green curves are represented the resonant modes with an index perturbation. The width of resonance mode $\Delta\omega$ is similar for both cases. The red line represents the fixed frequency of the probed light; b) Features appearing in the reflection spectra of the structure with different detected width (FWHM). On the diagrams are depicted the $\theta$ angle change for two resonant modes with different group velocity

frequency.

The derivative of the coupling wavevector with respect to the refractive index change can be described starting from Eq. 2.3 as follows:

$$\Delta \mathrm{k}_{\|} = \frac{\omega \times \mathrm{n}_{\mathrm{environment}}}{\mathrm{c}} \times \cos\theta \times \Delta\theta \tag{2.4}$$

This angle shift related to a refractive index change ($^{\Delta\theta}/_{\Delta n}$) is the angular sensitivity property of the biosensor. The angular sensitivity can be calculated from the group velocity definition ($\mathrm{v_g} = {}^{\Delta\omega}/_{\Delta \mathrm{k}_{\|}}$) and the Eq. 2.4. as follows :

$$\mathrm{Sensitivity} = \frac{\Delta\theta}{\Delta \mathrm{n}} = \frac{\Delta\,\omega}{\omega \times \Delta \mathrm{n}} \times \frac{1}{\cos\theta \times \mathrm{n}_{\mathrm{environment}}} \times \frac{\mathrm{c}}{\mathrm{v_g}} \times \frac{180}{\pi}\ [^\circ/\mathrm{RIU}] \tag{2.5}$$

where $\Delta\omega$ is the normalized frequency change due to a refractive index change on the structure, $\omega$ is the normalized frequency of the mode and c is the speed of light in vacuum.

To maximize the values of sensitivity, the parameters of the Eq. 2.5 needs to be optimized. The maximum frequency shift is given by Eq. 2.2, the incidence angle $\theta$ is limited in practice by the spot size obtained on the sample, $\mathrm{n}_{\mathrm{environment}}$ is 1 for air and 1.33 for water or biological solutions. The factor that can significantly enhance the sensitivity value of the proposed structure is the group velocity. Usually, low group velocity modes are encountered at wavevectors of high symmetry in the Brillouin zone of the PhC, i.e. for a very particular angle of incidence. As I will demonstrate further in this Chapter, it is possible to decrease the group velocity values for a large range of incident angles by using a particular design.

The sensitivity can be virtually infinite for modes with $v_g \rightarrow 0$, the ability to detect small angle shifts of the modes depends also from the bandwidth of the mode ($\Delta\Omega = {}^{\omega_0}/_{Q}$), where Q is the resonance quality factor. The GMRs interrogated from outside at a particular wavevector have a finite lifetime due to the PhC structure design, but also from fabrication imperfections or material absorption, as will be explained in details further in this Chapter. This finite lifetime translates to a finite angle width :

$$\Delta\Theta = \frac{c}{v_g} \times \frac{1}{\cos\theta \times n_{\mathrm{environment}}} \times \frac{1}{Q} \times \frac{180}{\pi} \tag{2.6}$$

Decreasing the group velocity (Fig. 2.2 c), the dispersion curve will better match the fixed frequency of the light injection, increasing the bandwidth of the detected GMR in the reflectivity spectrum $\Delta\Theta$ as in Fig. 2.2 d).

A decrease of the resonance width improves the locating of the angular resonance in the presence of noise originating from mechanical or laser fluctuations and therefore improves the detection limit of the device ([57]).

A trade-off is required between the low group velocity of a targeted GMR, which basically gives the sensitivity value of the structure, and the Q factor of the same guided mode resonance at a certain angle for a certain direction. It is necessary to keep the product $v_g \times Q$ high enough to have a narrow resonance width and good detection limit of the biosensor. This value will depend on the optical measurement setup used.

During this PhD thesis, I designed structures with low group velocity for a targeted GMR and with a quality factor achievable in fabrication, which can be detected with precision in the reflectivity spectrum.

### Visible light detection

The design of the 2D PhC is realized for detecting the refractive index changes at the limit of the visible regime at $\sim$ 800 nm. The reasons of choosing this wavelength range are because of the cameras available on the market that are very efficient at low prices and inexpensive mono-mode laser sources. A third reason is to avoid the frequency of 1.55 µm, even if that at this wavelength range there are available tunable laser light sources and detectors. Indeed, the infrared spectrum of water is dominated by the intense absorption due to the fundamental O-H stretching vibrations, absorption that limits the Q of the structure at 1.55 µm.

The realization of diamond photonic crystals for visible light detection represents a real challenge because it requires fabrication of small holes in the range of one hundred nanometers in diameter. Furthermore, continuous laser light sources at visible wavelength range that can be finely tuned, as there can be found at 1.55µm, are expensive, fact that requires a precision in fabrication at the nanometer scale. To my knowledge, there are no sensors for this wavelength range in polycrystalline diamond, mainly due to the fabrication challenges. The proposed design offers a large tolerance once fabricated in order to detect at the desired wavelength. The C2N Orsay is equipped with two single frequency lasers : one at 760 nm and the second one at 795 nm wavelength. All the PhC structures are designed and optimized to function at one of the mentioned laser wavelength.

## 2.3 Numerical simulation tools

I designed the PhC by simulating the structure using numerical tools. The results allows to determine the optimal parameters for bio-detection, as well as the quality factors or sensitivity values. Among all existing methods, plane wave expansion method (PWE) and Finite Difference in Time Domain (FDTD) are the most used. The use of these two calculation methods permits to understand the behavior of PhC in different conditions. The description of these two methods is beyond the purpose of this thesis, detail explanations can be found in ([11]). I will briefly describe however some parameters used for all the simulations of this thesis.

### 2.3.1 Plane wave expansion method

PWE is a computational method utilized in electromagnetics that simulates the eigenstates and eigenvalues of Maxwell's equations in a periodic structure, in Fourier space. It is the most used technique for calculating the dispersion relations of specific PhC geometries in which the simulations of the structures are periodic in the three directions of space.

To simulate the 2D PhC, a periodicity in the third direction is thus artificially introduced. As a consequence, the fundamental cell must be separated by a sufficient background region to ensure electromagnetic isolation. The guided modes are localized inside the PhC, so that the additional periodicity of the membranes with large separation will not affect the modes' eigenfrequencies ([58]). These guided modes cannot couple with the modes in the background, so these discrete bands are confined. Nevertheless, these confined modes can be calculated using PWE method despite the z direction periodicity. Leaky modes, however, which are not strongly guided, are dependent on the period introduced in the vertical direction. Typically, the supercell is a few times the fundamental cell lattice height.

The software used during my thesis for band diagram simulations using plane wave expansion method is MPB (MIT Photonic-Bands), a free software developed by Massachusetts Institute of Technology by Joannopoulos team ([11, 59]). 2D or 3D computation of structures were evaluated. It allows to calculate the electromagnetic field distribution of each mode of the structure and also the density of states.

### 2.3.2 Finite Difference in Time Domain method

FDTD method allows solving differential equations in the time domain. Proposed by Yee in 1966 ([60]), it consists on discretization of the electromagnetic field propagation E and H in space and time (Yee grid). The harmonic solutions are obtained in a second step through a Fourier transformation in time. In other words, the determination of the total field at any time t and at any point of space when an incident electromagnetic pulse strikes a photonic crystal with finite sizes can be obtained. The choice of the electromagnetic source with large frequency spectrum allows to determine all the resonant modes of the desired structure in one simulation. One other particularity of this method consists in introducing boundary conditions for finite dimensions of PhC. Perfectly Matched Layers (PML) can be defined at the borders of the PhC to progressively absorb the scattered field without generating any artificial reflection phenomena ([12]). It is possible to use Bloch-periodic boundary conditions and symmetry in certain directions which permits to reduce significantly the duration of the simulation.

Along the extraction of the resonant modes, using a time-domain method is possible to calculate the photon lifetime $\tau$ for these modes which is related to the quality factor by $Q = \omega \, \tau$ and also to compute transmission or reflection spectra.

There are multiple choices of software to simulate FDTD method. In this thesis the one used is MEEP (MIT Electromagnetic Equation Propagation) free-software, developed by the team of Joannopoulos ([11, 61]).

### 2.3.3 Data treatment and visualization

The results from simulations were analyzed by program developed by X. Checoury under Matlab program, with which the figures were created. Visualization of the band diagrams of the desired resonances with the corresponding quality factors was realized. The incident pulse is a temporal signal, consisting in a Gaussian source, which allows to obtain the energy dispersion relations.

Reflection spectra were simulated to verify the intensity of the resonances of interest. Spectra were obtained with the incident light assumed to be a Gaussian source. Each spectrum was normalized with respect to the incident pulse, which was calculated similar in another simulation in vacuum without the slab structure.

## 2.4 Design optimization for angular interrogation

I started this Chapter by presenting the general functioning of a optical biosensor based on refractive index measurement. The schematic representation of the proposed design was introduced and it's advantages that lead to surpass the sensitivity values expressed by other designs from the literature.

In the following part I will focus on the optical properties of the PhC structure. Simulation of the dispersion relations of the structure give the necessary information to optimize the performances of the biosensor for visible wavelengths detection. The theoretical sensitivity expectations will be expressed, along with the factors that lead to these values, such as the group velocity and quality factors. The control of the quality factors and the coupling strength of the leaky modes will be described in details. The intensity of the targeted modes on the reflectivity spectrum will be expressed in ideal and real (fabrication) conditions.

### 2.4.1 Low group velocity in 2D photonic crystal

As explained in the beginning of this Chapter for the proposed design, high sensitivity values and low detection limit are requested to increase the performances of the design. These requirements can be achieved for a low group velocity mode with high Q factor. I also showed that the angle shift is larger in a case of a low group velocity mode for a fixed frequency than in the case of a larger group velocity mode (Fig. 2.2 c) and d). The difficulty of designing of such PhC sensor reduces to the ability to design a photonic crystal that presents a slow mode over a series of frequency and wavevector range. Such a mode is robust to fabrication imperfections since slow light is achieved for various frequencies contrary to slow modes at the Γ point that may have a high Q but are slow only near a particular frequency at quasi-normal incidence. To design a PhC with such a mode, numerical simulations were performed. In the next paragraphs, I will show how the 2D PhC can support guided mode resonances experiencing high Q and extremely low group velocity. This approach is general and can be imagined for different geometries, for both TE and TM polarization, as I will present further. Moreover, it will be presented how a shift in frequency can be achieved for the slow light GMR without changing the structural parameters of PhC i.e., even after the fabrication process.

Let's consider a 2D PhC with squared array of circular air holes. I applied plane wave expansion model to simulate the structure using MPB software. Fig. 2.3 represents the band diagram of a two dimensional structure simulated in two dimensions (x and y). It was chosen for its simplicity regarding the 3D representation and the modes behavior for the 2D case extends to the 3D case. So, I will temporarily used this 2D band diagram as if it were a 3D band diagram to explain my approach before doing full 3D simulations.

One can find two types of modes: confined vertically inside the structure with an evanescent profile in air (index guided modes) and guided resonances (modes non-confined) which extends indefinitely in air. In the free-space, the dispersion relation of a plane wave follows the equation $\omega = \frac{\mathrm{c}}{\mathrm{n_{air}}}|\mathrm{k}| = \frac{\mathrm{c}}{\mathrm{n_{air}}}\sqrt{\mathrm{k}_{\|}^2 + \mathrm{k}_{\perp}^2}$, for some perpendicular real wavevector $\mathrm{k}_{\perp}$. For a given value of $\mathrm{k}_{\|}$, there will be modes with every possible frequency greater than c $\mathrm{k}_{\|}$, because $\mathrm{k}_{\perp}$ can take any value. The spectrum of states is continuous for all frequencies above the light line ($\omega_{\mathrm{lightline}} = \frac{\mathrm{c}}{\mathrm{n_{air}}}\sqrt{\mathrm{k}_{\|}^2}$ ). The region of the band structure with $\omega > \mathrm{ck}_{\|}$ is called light cone and is represented by radiative modes, also called leaky-modes or guided mode resonances (GMR), which posses more or less strong coupling with the free-space ([11]). This type of resonances are necessary for our proposed design and in the next sections I will present the mechanisms to tune the coupling with the free-space for a particular mode.

On the other hand, the modes under the light cone have the component $\mathrm{k}_{\perp}$ imaginary, meaning that the modes are vertically confined inside the slab and decay exponentially away from the slab structure. These modes are known as index-guided modes and theoretically propagates without losses inside the crystal and cannot be coupled from the free-space.

Fig. 2.3 a) represents the calculated dispersion curves in 2D for a PhC structure calculated for the TE polarization in the directions described by the irreducible Brillouin zone $\Gamma$ , X and M. The fundamental lattice cell is composed by a single air hole of 0.34a radius (a being the period) and the lattice arrangement is squared.

For this kind of structure, there exist a band that has the same frequency at two particular wavevectors: one at the $\Gamma$ point, at the center of the Brillouin zone and the other at some particular wavevector, denoted J, between the points of high symmetry, X and M, at the boundary of the Brillouin zone (see the black arrow at frequency 0.54 in Fig. 2.3 a). Because the band is continuous and two of its extremities have the same frequency, the group velocity must cancel for wavevectors between the $\Gamma$ point and the J point, as can be seen Fig. 2.3 b). Indeed, when the wavevector is varied along the $\mathit{\Gamma}$ J direction (here at $\phi = 7°$ from the $\Gamma$ X direction, as shown in the inset of 2.3 b), a mode with a frequency near 0.54 experiencing low group velocity over a large number of wavevectors k can be seen above the light cone.

### 2.4.2 Q control of the leaky modes

In the previous paragraphs, the band diagram of the structure was calculated in two dimensions, thus implying that the quality factors are infinite. To have access to the quality factors values of the modes, three dimensional simulations were performed. The band diagram was numerically simulated for TE polarization in MEEP software using FDTD method.

However, the configuration with only one hole in the fundamental cell, does not allow the control of some properties of the radiative modes that are inside the light cone, such

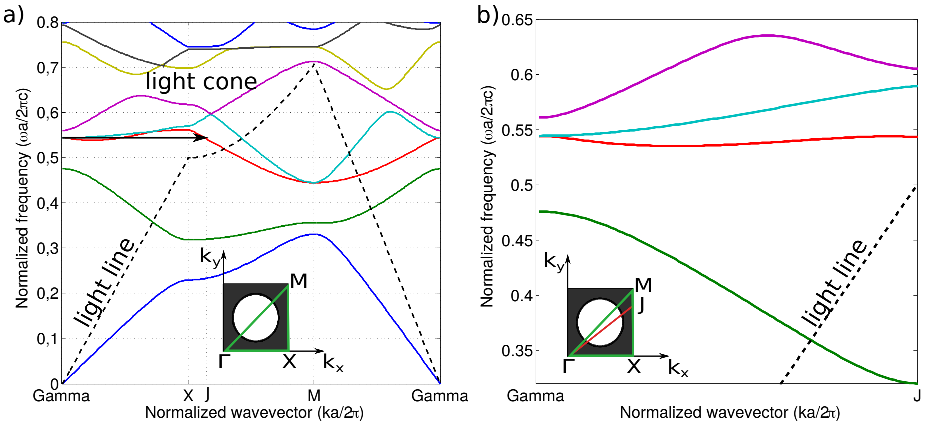

Figure 2.3: a) Band diagram of a two dimensional PhC 2D simulation for a single hole in a fundamental lattice cell for a squared lattice of air holes photonic crystal. The radius of the hole is 0.34 a, where a is the period of the lattice. On bottom left inset is depicted the refractive index of the hole (n=1) and the refractive index of the material (n=2.4) and the wavevector directions in the Brillouin zone in k-space Γ , X and M. The band diagram is shown for TE polarization. b) Band diagram of the same structure probed in a particular direction Γ J to decrease the group velocity of a targeted leaky mode.

as the coupling strength or the quality factor. In the previous subsection I described that the modes inside the light cone can couple to the continuum of unbounded radiation and possess a finite lifetime ([56]).

In general, the radiative modes that lies inside the light cone offer quite low Q. A method to achieve high Q GMR consists in performing a folding of the band diagram of the PhC, for example by imposing a second period to the PhC so that the Brillouin zone is reduced and truly guided modes are folded above the light cone (Fig. 2.4 blue curve).

As explained by Nicolaou *et al* ([62]), for two holes in fundamental lattice cell, when the radius of one hole differs slightly from the other one, $\Delta r = | r_1 - r_2 | \rightarrow 0$, the quality factors of the resonant modes can be tuned at very large values. Indeed, if the hole size difference is small, the resonant mode tends to have the characteristics of a guided mode, where the quality factor tend towards infinity. When $\Delta r$ is decreased, the Q factor can be controlled at the desired value and, at the same time, the coupling of the GMR with an incoming or out-coming wave can be increased.

The same behavior was found in the case of four holes in the fundamental lattice cell (Fig. 2.5 a), with the possibility to tune the desired resonance at the wanted quality factor for a specific direction. In Fig. 2.5 b) are shown the Q factors of a TE polarization GMR of a PhC structure resulted from varying the difference ($\Delta \mathrm{r} = \mathrm{r}_1 - \mathrm{r}_2$) between the “big” hole ($\mathrm{r}_1$) and the other three “small” holes ($\mathrm{r}_2$). In the presented case, the “small” holes were 0.17 a, a being the lattice parameter. It can be observed that the quality factor of the resonant mode is always decreasing when the $\Delta \mathrm{r}$ increases. To achieve higher quality

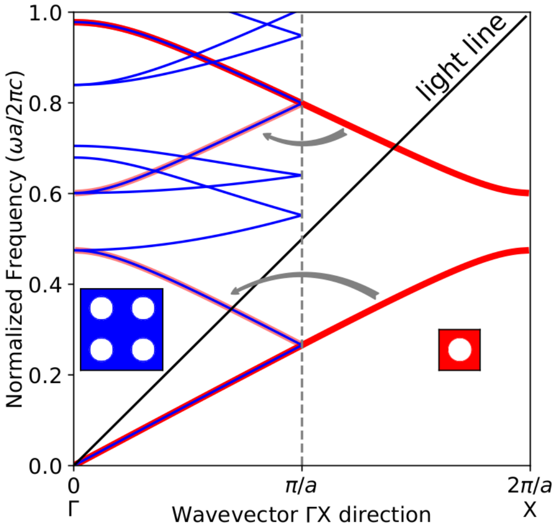

Figure 2.4: Illustration of the band folding. Two band diagrams along the ΓX direction are superimposed for two square lattice PhCs: a single-hole cell PhC of period a/2 (dark red curve) and a four-hole cell PhC of period a (blue curve) with same radii, 0.14a. The light red curve indicates how some modes originate from the folding of the modes of the single hole pattern PhC due to the smaller size of the Brillouin zone of size π/a along ΓX

factors, it is sufficient to have small $\Delta$r. During the structure optimization, similar behavior was experienced for different values of “small” holes. One can conclude that the control of quality factor value of the desired mode at specific interrogation angle for a specific direction was achieved by controlling the $\Delta$r .

#### 2.4.2.1 Q decay mechanisms

Quality factor of a sensor is an important property for describing its performances. A GMR in a resonant cavity decays slowly, resulting in a finite lifetime. It behaves as a mode with a complex frequency $\omega_c = \omega_0 - i\gamma/2$, where $\gamma$ is the loss rate, $\omega_0$ is the resonant mode frequency and the imaginary part of the frequency corresponds to an exponential decay. When the field decays as $e^{-\gamma t/2}$, the energy inside the cavity decays as $e^{-\gamma t}$. The quality factor can be written as the dimensionless quantity $Q \triangleq \omega_0/\gamma$. An interpretation of the quality factor can be expressed as :

$$\frac{1}{Q} = \frac{P}{\omega_0\, U} \tag{2.7}$$

where $^1/_Q$ is the decay rate, P is the outgoing power and U is the electromagnetic energy localized in the cavity.

If the mode has more than one decay mechanism, each mechanism can be characterized

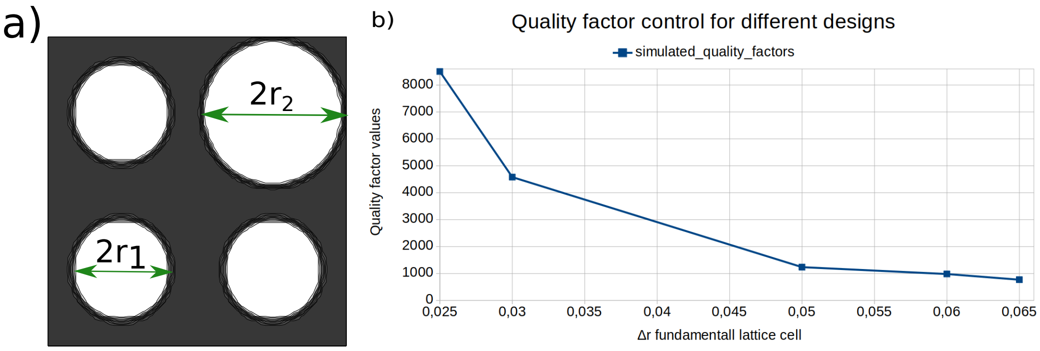

Figure 2.5: a) Fundamental lattice cell with four holes. Three holes (r1, so called small) and the forth one (r2, named big) allows the control of the quality factor and the coupling strength. If the difference $r2 - r1 \to 0$, the quality factor is tuned at very large values. The color-bar on the right side defines the epsilon values: blue color for air holes and red color for diamond; b) Quality factor control for one TE polarization GMR inside the light cone after the band folding and outside light cone(truly guide) before band folding, interrogated in specific direction of 28.8° from the Γ X direction. Quality factor tuning resulted by varying the difference between the big hole and the other three small holes (0.17a for the radius) from the fundamental lattice cell (a).

and a factor $\mathrm{Q_{final}}$ that will contain all the losses can be introduced:

$$\frac{1}{\mathrm{Q_{final}}} = \frac{1}{\mathrm{Q_{intrisic}}} + \frac{1}{\mathrm{Q_{fabrication}}} + \frac{1}{\mathrm{Q_{material}}} \tag{2.8}$$

The $\mathrm{Q_{fabrication}}$ is related to the ability to fabricate, using cleanroom technologies, high quality factor modes in polycrystalline diamond. Losses can be associated to the fabrication imperfections, such as surface roughness or hole etching defects.

The $\mathrm{Q_{material}}$ is associated with losses when light propagates trough, related to the fact that the material is not perfectly transparent at that specific wavelength and there is always a residual absorption. In any case, the non homogeneous distribution of diamond grains in vertical direction leads to symmetry break. The presence of the grain boundaries introduce unwanted losses to the structure which leads to the diffusion and absorption in the visible wavelengths and limits the value of quality factors. In our group, Q=6500 were reported in polycrystalline diamond for photonic crystal cavities for near infrared detection ([55]). This value is though to be limited by the polycrystalline diamond material.

The $\mathrm{Q_{intrisic}}$ corresponds to the quality factor intrinsic of the designed cavity. It can be controlled by engineering the structure design, by choosing the appropriate geometry for the PhC with four holes in the fundamental lattice cell. In other words, by varying the size of one hole radius as compared to the others three from the fundamental lattice cell. The resulting quality factor can be described as :

$$\frac{1}{\mathrm{Q_{intrinsic}}} = \frac{1}{\mathrm{Q_{coupling}}} + \frac{1}{\mathrm{Q_0}} \tag{2.9}$$

where $\mathrm{Q_{coupling}}$ represents the coupling of the guided resonances to outside radiation and $\mathrm{Q_0}$ is the quality factor obtained when the four holes from the fundamental lattice cell are of the same size. The $\mathrm{Q_{coupling}}$ is being subjected to match certain conditions [56]. When coupled, it conduct to interferences in the reflectivity or transmission spectra of the photonic crystal. The shape of resulting features are in general Fano resonance-shape and will be discussed in the Chapter 4 in detail. A good coupling is represented in the normalized reflectivity or transmission spectra by a feature that approaches unity. To maximize the intensity of the reflected mode, we want that :

$$\frac{1}{\mathrm{Q_{coupling}}} = \frac{1}{\mathrm{Q_{fabrication}}} + \frac{1}{\mathrm{Q_{material}}} + \frac{1}{Q_0} \tag{2.10}$$

The fabrication of this type of structures in diamond is new in our group, thus we don't know the quality factor that may be reached for visible range detection. The realization of this type of PhC is more challenging than the cavities previously fabricated for infrared range due to the smaller hole sizes (typically 100 nm in diameter). Starting from these assumptions, the further numerical simulations were done with structures designed to have a quality factor ranging from 800 to 5000.

#### 2.4.2.2 Control of the Q of a leaky mode

In the first example presented in Fig. 2.3, the band diagram is calculated for a two-dimensional simulation. It was chosen for it's simplicity regarding a 3D simulation, to describe the principle of lowering the group velocity of a desired GMR. For the next representation of band diagrams, the numerical simulation were conducted in 3D using MEEP software. The PhC was defined with a finite thickness and the quality factor for each mode was calculated.

Fig. 2.6 a) represents the dispersion relations of a structure, calculated in three-dimensions for TE polarization, with four holes in the fundamental lattice cell (as depicted in inset) and a slab thickness equals to the period. The control of the quality factor of a desired leaky mode was achieved by choosing the appropriate Δr, as shown in Fig. 2.5 b). The band diagram in Fig. 2.6 a) was calculated for a hole size of 0.17 a, which is the same size of "small" holes (0.34a) in Fig. 2.3 a), when the size of the fundamental lattice cell is multiplied by two in each direction. The desired quality factor for the targeted resonant mode of the structure was around 1000 and as consequence the "big" hole was 0.24 a. Additional resonances appear in the band diagram as compared to the structure simulated in Fig. 2.3 a) and are due to the band folding related to the larger cell. The colorbar represents the

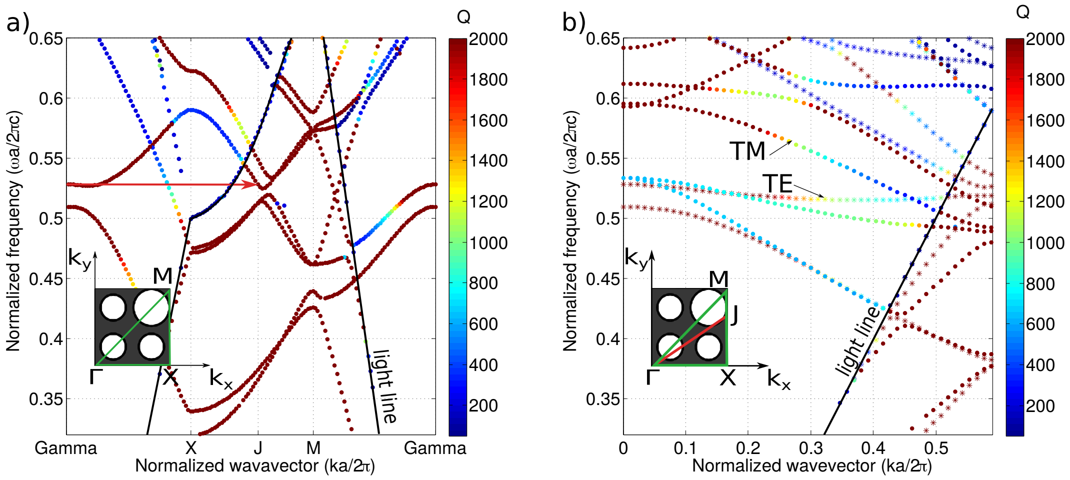

Figure 2.6: a) Band diagram calculation of a PhC with four holes in a square lattice. Radius of the three similar holes is 0.17a, the radius of the forth hole is 0.24a and the thickness is a. On bottom left inset is depicted the refractive index of the hole (blue, representing the index of air n=1) and the refractive index of the material (red, representing the refractive index of the diamond n=2.4) and in gray lines the wave-vector directions in the Brillouin zone in k-space Γ, X and M. The band diagram is shown for TE polarization. b) Band diagram of the same structure when interrogated in the specific direction represented by a black arrow (a). The inset represents the Brillouin zone Γ, X and M and also the specific direction *Γ* J (28° from Γ X direction). The band diagram is represented for both TE and TM polarizations.

quality factor of the resonant modes, with the maximum value shown here in red color of 2000. The Q of the resonances are overcoming this arbitrarily fixed value to emphasize the Q evolution around the targeted Q factor of the fabricated sample. A logarithmic representation of the same diagrams is shown in Fig. 2.7 a), where the Q factors of the modes lying in the light cone are significantly lower than the modes from outside light cone.

The reduced group velocity of a desired resonant mode was achieved using the same strategy explained in subsection 2.4.1. The mode, that is located at the same normalized frequency at the Γ point and at a certain point between X and M, is pointed out by a black arrow. The resulting low group velocity for the desired mode when interrogated in the specific azimuthal direction *Γ* J (28° from Γ X direction, as depicted in the inset) is represented in Fig. 2.6 b) and in logarithmic scale in Fig. 2.7 b). For the targeted GMR, it hardly varies in frequency for a large range of $k_{||}$ wavevectors. Using the linear colorscale, it can be observed that the resonant mode has a $Q_{\text{intrisic}}$ of around 800. The dispersion relations of the structure are shown for both TE and TM polarizations.

The good control of the Q factor of a targeted GMR is achieved by varying the size of one hole from the fundamental lattice cell. Decreasing the difference between the big small and the other three small ones, the Q will increase. For example, low group velocity mode of interest will have its Q factor increased from 800 to ∼ 5000 when the big hole size is

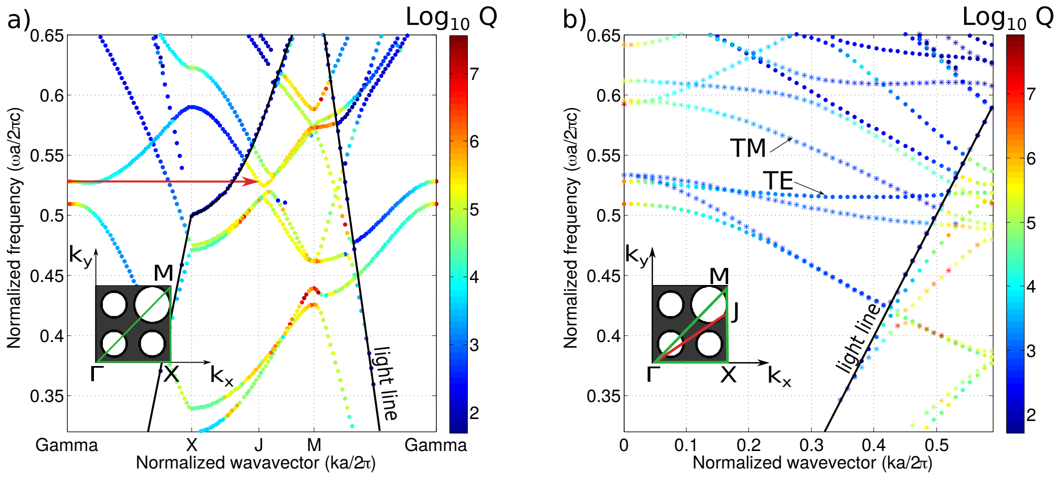

Figure 2.7: Band diagram representation for the same structure as in Fig. 2.6 a) and b) in logarithmic base-10 scale

reduced from 0.24a to 0.2a, as shown Fig. 2.8. The GMR will lower its frequency because of higher effective refractive index of the diamond structure and the reduced radius of the hole. To keep the same slow light propagation for the targeted GMR over a large $k_{||}$ wavevectors, the azimuthal angle $\phi$ is changed, the ideal direction being in this case 30° from the $\Gamma$ X direction.

To summarize, a PhC design was proposed, where a targeted GMR of the structure is experiencing a low group velocity when interrogated in a certain direction and dispose a quality factor that can be controlled at will. The next step in our device conception is to ensure that the reflectivity of the desired mode is sufficiently intense in order to be measured.

### 2.4.3 Reflectivity simulations

Reflectivity spectra were calculated at various $k_{||}$ wavevectors and consists on sharp features superimposed over a Fabry-Perot oscillation, which is the background. More details of this Fabry-Perot fringes and GMR features will be presented in the Chapter 4. In Fig. 2.9 a) is represented the band diagram of the structure, designed with a targeted Q factor of the GMR of 800. Let's assume that we want to calculate the reflectivity for a particular wavevector plotted for a multitude of frequencies (here, $k_{||} = 0.43$, represented in the circled zone pointed out in the band diagram), the corresponding features are obtained (Fig. 2.9 b). It can be observed that most of the modes are well defined, with a reflectivity approaching unity, with features that resemble a Lorentzian line shape.

In real samples, there will be always losses related to material absorption, such as diffusion related to the grain boundaries and fabrication imperfections (surface roughness, hole etching defects). The Q that can be reached in fabrication is unknown. Nevertheless, previous results for PhC cavities in polycrystalline diamond for 1.55 µm show a Q factor of

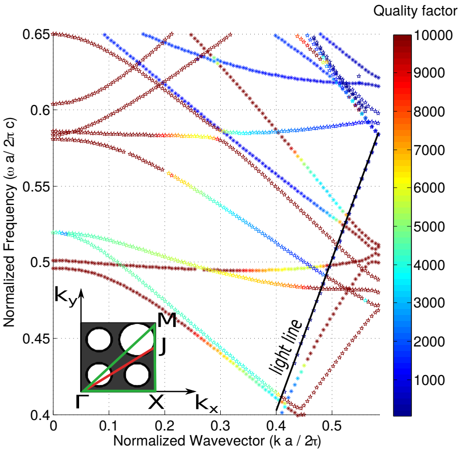

Figure 2.8: Band diagram simulation for four holes in fundamental lattice cell for a 2D square lattice of air holes photonic crystal. Radius of the three similar holes is 0.17a, the radius of the forth hole is 0.2a and thickness is a. On bottom left inset is depicted in green lines the wave-vector directions in the Brillouin zone in k-space Γ , X and M, and in red color the specific direction Γ J (30° from Γ X direction). The band diagram is represented for both TE and TM polarizations.

6500 ([63]). To approximate the real response of the device, simulations were conducted in the reflectivity spectrum adding the mentioned losses. The aim of this calculation consists in the reflectivity monitoring of the targeted GMR with low group velocity to ensure that the intensity of the mode is easily enough to be readable with the experimental setup. The losses are introduced in the software by adding a material conductivity. The value of the parameter was arbitrarily chosen in such a way that the Q factor simulated with the loses is near half the Q factor in ideal conditions. For example, in Fig. 2.9 c), the Q of the structure with losses is limited at 500.

The low $v_g$ TE resonance located at 0.515 normalized frequency from the Fig. 2.9 a) is experiencing a $Q_{intrisic}$ of 753 in the ideal conditions (blue color from Fig. 2.9 c) and when losses were introduced in the simulation, the quality factor was decreased at 506 (red color from Fig. 2.9 c). The detected TE GMR feature decreases in intensity, but it can be clearly observed, with a slightly wider shape. Without changing the losses parameter, in the case of a structure designed to have a lower Q factor in ideal conditions i.e.,with higher coupling losses, the intensity of the reflected GMR will be higher (cyan color from Fig. 2.9 c). For the designs that experience a higher intrinsic Q factor of GMR, the intensity on the reflectivity spectrum will decrease. It can be observed that for a TE GMR with a Q over 1000, when the material limits the Q at 500, the detected mode is hardly visible on the spectrum.

A second case of design is simulated for a structure with the dispersion relations shown in Fig. 2.10 a). The reflectivity spectrum is calculated for $k_{\|} = 0.43$ for a multitude of frequencies, as represented in Fig. 2.10 b). The targeted TE GMR is experiencing a Q of

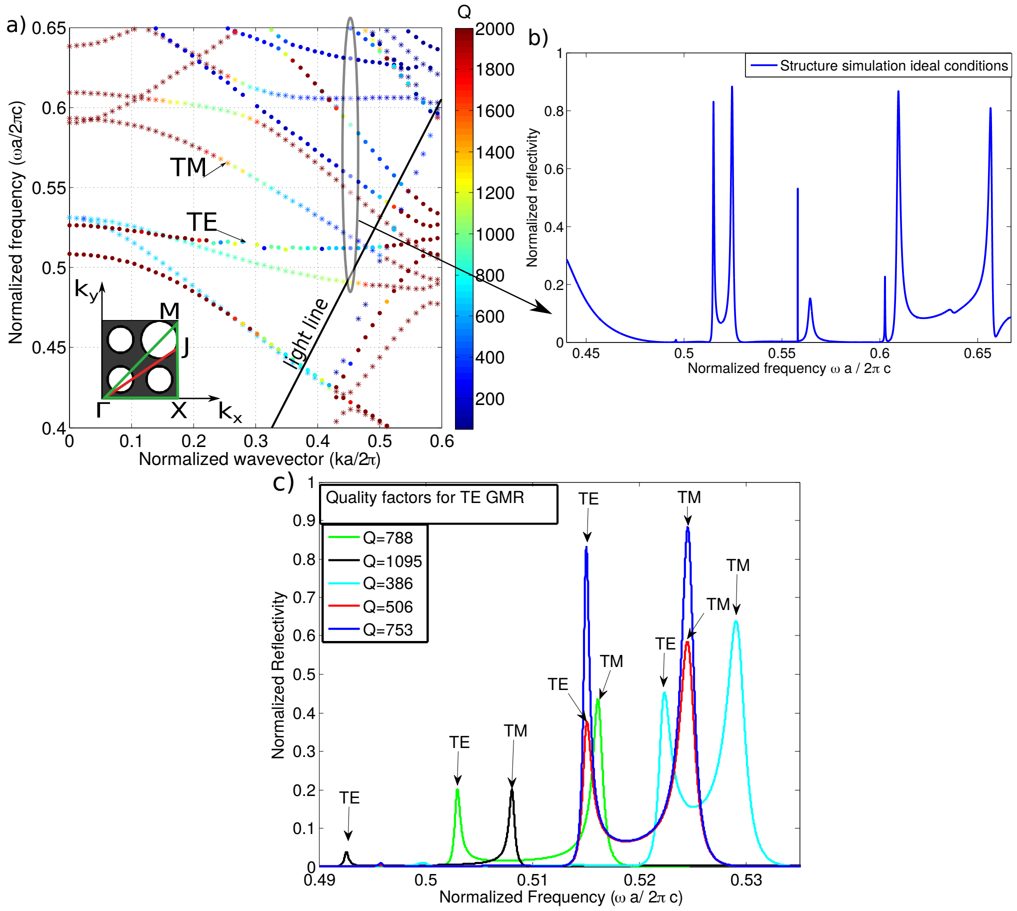

Figure 2.9: a) Band diagram simulation for four holes in fundamental lattice cell for a 2D square lattice of air holes photonic crystal. Radius of the three similar holes is 0.17a, the radius of the forth hole is 0.24a and thickness is a. The inset represents the Brillouin zone Γ, X and M and also the specific direction *Γ* J (28.8° from Γ X direction). The band diagram is represented for both TE and TM polarizations. The encircled zone will be further analyzed; b)Normalized reflectivity spectrum intensity of the structure with low $v_g$ resonant mode at $k_{||} = 0.43$. c) Reflectivity spectrum representation of TE and TM GMR for various structures with different Q : 3 holes of 0.17 and 1 hole of 0.24 (blue color) ideal conditions (Q=753), shown also in b), with the corresponding GMR intensity of the same structure when the Q is limited at 500 (red color); 3 holes of 0.17 and 1 hole of 0.25 (cyan color); 3 holes of 0.17 and 1 hole of 0.22 (green color) and 3 holes of 0.17 and 1 hole of 0.2 (black color)

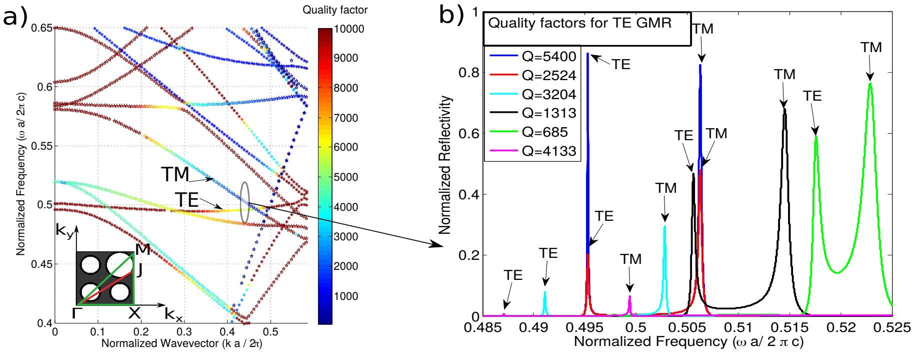

Figure 2.10: a) Band diagram simulation for four holes in fundamental lattice cell for a 2D square lattice of air holes photonic crystal. Radius of the three similar holes is 0.17a, the radius of the forth hole is 0.2a and thickness is a. The inset represents the Brillouin zone Γ, X and M and also the specific direction *Γ* J (27° from Γ X direction). The band diagram is represented for both TE and TM polarizations. The encircled zone will be further analyzed; . c) Reflectivity spectrum representation of TE and TM GMR at $k_{||} = 0.43$ for various structures with different Q : 3 holes of 0.17a and 1 hole of 0.2a (blue color) ideal conditions (Q=5400), with the corresponding GMR intensity of the same structure when the Q is limited at 2524 (red color); 3 holes of 0.17a and 1 hole of 0.19a (cyan color); 3 holes of 0.17 and 1 hole of 0.24a (green color); 3 holes of 0.17 and 1 hole of 0.18a (magenta color) and 3 holes of 0.17 and 1 hole of 0.22a (black color).

5400 in ideal conditions (blue color) and the losses added for material limits the final Q at 2500 (red color). The intensity of the detected GMR is significantly attenuated from 0.9 to 0.2 normalized frequency. For other structures calculated with the same losses parameter, the designs where the intrinsic Q factors are lower, the detected GMR intensity will be higher and for the designs with higher Q will be the opposite case, with the GMR features in the reflectivity spectrum hardly measurable.

Here I show the reflectivity simulations of two designs with different quality factors (800 and 5000) in the ideal conditions. Adding material losses i.e. to simulate real sample conditions, the intensity of the detected GMRs in the reflectivity spectrum was calculated. It was shown that in order to have a easily readable GMR for polycrystalline diamond material, the design was chosen to experience quality factors up to 5000 in real conditions. If we will succeed to fabricate Q of 5000, the intensity of the detected GMR in the reflectivity spectrum will approach unity.

### 2.4.4 2D Photonic crystal biosensor slab performances

One of the design studied during this thesis has the following band diagram (Fig. 2.11 a), where the photonic crystal is optimized to have, according to Eq. 2.5, the best sensitivity values at the limit of visible wavelengths range. The design is the same as the previous example from Fig. 2.6 b), only that the representation of the dispersion relation of the structure was plotted in normalized frequency versus the co-latitude $\theta$ angle instead of $k_{||}$. In Fig. 2.11 b) are represented only the resonances of interest from Fig. 2.11 a).

The goal of the designed structure is to inject light from a single wavelength source (a laser) and to probe two different GMRs at different incident angles. The design will give two sets of different information regarding the recognition event on the device surface, each one having a different electromagnetic pattern, which corresponds to a different penetration depth. Ideally, the two targeted GMRs have low group velocities. Photonic devices that uses two modes detection can be found in literature ([34, 64, 31]).

I will recall that the sensitivity values are calculated for our proposed device according to the formula :

$$\text{Sensitivity} = \frac{\Delta\theta}{\Delta \text{n}} = \frac{\Delta\ \omega}{\text{v}_\text{g}\ \Delta\text{n}} \times \frac{1}{\omega \times \text{n}_\text{environment}} \times \frac{1}{\cos\theta} \times \frac{180}{\pi}\ [°/\text{RIU}] \tag{2.11}$$

As mentioned in the beginning of the Chapter, I searched to maximize the performances of the PhC structure by optimizing each term of the sensitivity formula. We know that the maximum frequency shift is given by the Eq. 2.2 and the refractive index of the environmental medium can be 1 for air and 1.33 in the case of water or biological solutions. The structure design was conceived to target the first GMR suited for our demands and to detect it at high $\theta$ angles relative to normal incidence. The group velocity is the main factor, on which we have the possibility to tune at will. Decreasing it at low values for a desired GMR, the sensitivity values can be significantly enhanced. In the next paragraph I will present the influence of each of the factors that can increase the sensitivity values and also give the expected performances for two different designs optimized during this PhD thesis.

#### 2.4.4.1 Light interrogation at high incidence angles

For the given example of 2D PhC membrane, the structure was engineered to have the TE resonant mode with slow light at high angles (Fig. 2.11). As shown in Fig. 2.11 b), the low group velocity GMR with controlled $\text{Q}_\text{intrisic}$ is found in the reflection spectrum at an angle of 50° from normal incidence.

To make a comparison between a low $\text{v}_\text{g}$ resonant mode at 20° from normal incidence ($1/\cos 20° = 1.064$) and another at 70° at the same frequency ($1/\cos 70° = 2.9238$), the sensitivity value will be increased by a factor 3 in the case of the higher incidence angle.

#### 2.4.4.2 Resonant mode at low frequencies

Fig. 2.6 a) shows the dispersion relations of the 2D PhC membrane. It can be observed that the first resonance that could have slow light propagation into the photonic crystal

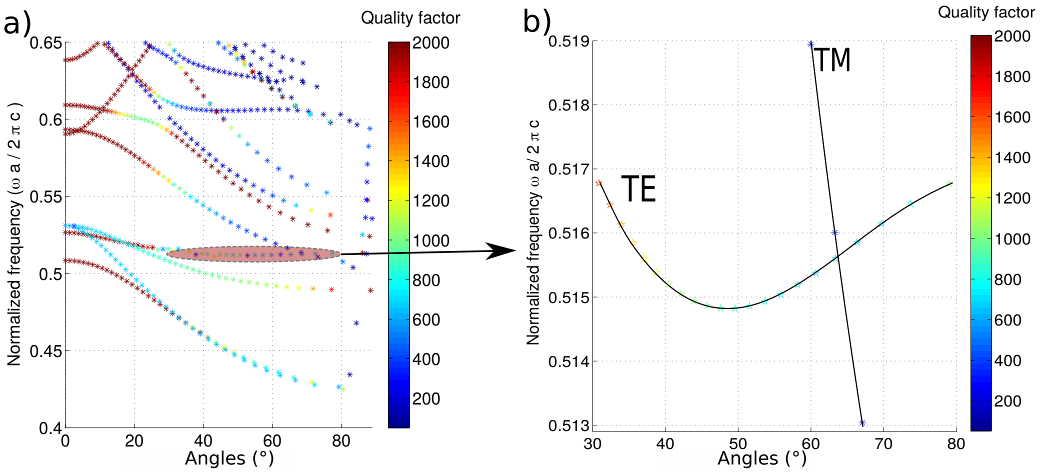

Figure 2.11: a) Band diagram of the same structure from Fig. 2.6, when interrogated in the specific direction *Γ* J (28,8° from Γ X direction). b) Zoom on the dispersion relations of the targeted resonances. The red line represents the specific frequency of the incoming light. The band diagrams are represented for both TE and TM polarizations.

is found at 0.52 normalized frequency. Knowing that the sensitivity formula is inversely dependent from the resonant frequency, working at this frequency will also slightly enhance the final sensitivity value as compared to other slow modes at a normalized frequency of 0.6. Decreasing more the resonant mode involve thicker diamond membranes or smaller holes. The normalized frequency of the desired mode can be decreased to 0.45, but to decrease it more, it will be more challenging from the fabrication point of view. The influence of this parameter is not critical, however I took it into account when the final structure was optimized, searching for the first available resonant mode for each design.

#### 2.4.4.3 Slowest group velocity that can be detected

Slowing the light propagation inside a targeted GMR will enhance drastically the sensitivity values of the structure. As I illustrated in Fig. 2.2, decreasing the group velocity for a desired mode with a certain Q will match the fixed frequency of the laser at a certain angle and the detected mode will have a wider shape in the reflectivity spectrum. The width of the GMR features in the reflectivity spectrum needs to be small in order to detect small angle shifts. For that, we restrict the group velocity calculations for determining the sensitivity expectations at group velocity not lower than 0.003.

In Fig. 2.11 is illustrated an example of structure with quality factor of the desired TE mode of 800, as it can be seen on the colorbar. Simulations of structures with quality factors up to 5000 were calculated, slightly modifying the frequency of the dispersion relations. The control of the Q is realized by changing the size of one hole regarding the other three holes from the fundamental lattice cell.

Sensitivity simulations can be divided in two categories: bulk sensitivity, related to the global refractive index change of the structure and surface sensitivity, where the refractive index is changed only in the near surface of the structure, linked to the molecular binding event.

Bulk sensitivity simulations were performed by slightly changing the refractive index of the surrounding medium ($2 \times 10^{-3}$). In the case of the TE low $v_g$ resonance shown in Fig. 2.11 b), if light is injected at 0.5148 normalized frequency, in the reflection spectrum will appear two features corresponding of the same mode and a third one that corresponds of a TM mode. Furthermore, the possibility to detect two low group velocity modes along with one other mode with high group velocity should conduct to more precise and accurate measurements. The theoretical bulk and surface sensitivity values, calculated using Eq. 2.5 are listed in table 2.1. For the TE mode with a $v_g$ =0.003, there are two coupling angles : the first one at 45.784° with a bulk sensitivity value of 2340°/ RIU and the second one at 51.618° with a bulk sensitivity value of 3110°/ RIU. The second value of the targeted GMR is higher than the first one relies on the fact that the coupling angle is greater, thus the cosine of the angle will slightly improve the final value of sensitivity. The second and the dominant factor is the slightly lower group velocity of the GMR.

The TM rapid mode is coupled at 62.156° and has a theoretical bulk sensitivity value of 62°/ RIU. Except the group velocity, the other factors involved in the calculus of sensitivity has comparable values to the TE mode. Because $v_g$ is almost 85 times higher than in the case of TE second resonance, the bulk sensitivity of TM GMR is 50 times lower. The higher frequency shift when the environmental medium is changed and an increased $\theta$ coupling angle improves the final result in the given conditions.

In the case of surface sensitivity simulations, the refractive index was changed only for a few nanometers of the surrounding medium, which corresponds to a local change of the index related to a recognition event. The calculation was performed by modifying by $2 \times 10^{-3}$ the refractive index over a 16 nm thickness. In general, the target molecules have a refractive index of 1.45 and a size in the range of several nanometers. The reason for choosing these parameters is that the computational time required to simulate a nanometric layer accurately is prohibitive. So we choose to estimate the effect of molecular absorption with a “thick” layer of 16 nm, but with a low refractive index.

When comparing the surface sensitivity values to the bulk ones, it can be observed that in all three case the final value is around five times smaller. The targeted TE and TM behave similarly, as in the bulk sensitivity, keeping the same ratios for the final values.

One can conclude that the PhC proposed design offers extraordinary bulk and surface sensitivity values, overcoming somehow the limitations imposed by the $\lambda/n$ value in the case of a frequency interrogation. The dominant factor that led to such results is the group

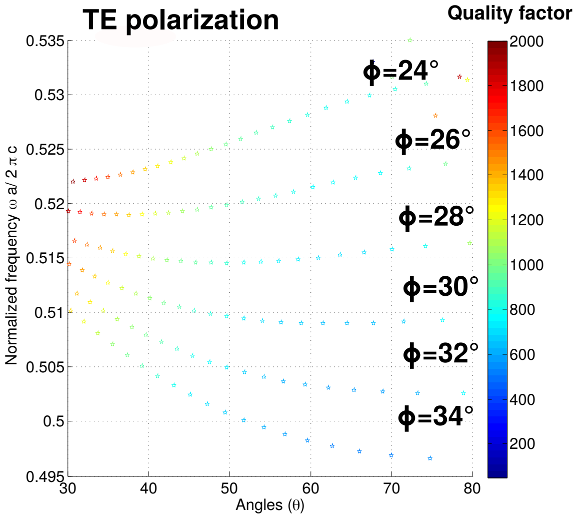

Figure 2.12: Different azimuthal directions possible to lower the group velocity for the PhC represented in Fig. 2.11

velocity. We restrict the value of $v_g$ in simulation at 0.003, but if we are able to detect modes below this value, the sensitivity values could be higher than expected.

### 2.4.5 Structure versatility for decreasing the group velocity

The possibility to decrease the group velocity is possible at different azimuthal angles, as shown in Fig. 2.12. In practice, realizing the device with the desired parameters from the simulations is difficult to achieve. The multiple technological processes involved in the fabrication of a 2D PhC slab makes the actual geometrical parameters to slightly vary from the desired ones (film thickness, hole diameter, surface roughness etc). Once the structure is realized, the optical measurements are performed. The injected light comes from a laser at a fixed frequency. One can finely adjust the energy of the slow GMR by changing the azimuthal $\phi$ angle to match the energy of the laser, as shown in Fig. 2.12. By varying the azimuthal $\phi$ angle from 20° to 30°, the same mode can be slightly varied in frequency and there will always be an angle with a low group velocity, making the design versatile to came across the fixed frequency. This represents more than 8% variation in term of wavelength. Typically, the fabrication imperfections lead to 2-3 % of error from the desired wavelength. One can conclude that the proposed design offers a versatility regarding the frequency of the targeted mode to match the fixed energy of the laser, while maintaining a low group velocity.

| Polar | $k_{\parallel}$ | $v_g$ | $\Delta\omega$ Bulk sensitivity $\times 10^{-4}$ | $\Delta\omega$ Surface sensitivity $\times 10^{-5}$ | $\theta$ n=1 | $\theta$ $n_{env}$ =1.002 | $\theta$ $n_{molec}$ =1.002 | Quality factor | Bulk sensitivity °/RIU | Surface sensitivity °/RIU |
|---|---|---|---|---|---|---|---|---|---|---|
| TE | 0.3691 | 0,00342 | 1.0035 | 2.042 | 45.784 | 45.796 | 45.787 | 1032 | 2339.47 | 476 |
| TE | 0.4037 | 0,003 | 1.0437 | 2.064 | 51.618 | 51.633 | 51.621 | 884 | 3109.53 | 614 |
| TM | 0.4653 | 0.2546 | 1.333 | 2.53 | 62.128 | 62.156 | 62.133 | 320 | 62.13 | 11.78 |

Table 2.1: Bulk and surface theoretical sensitivity values of the two dimensional photonic crystal optimized for sensing from Fig. 2.11

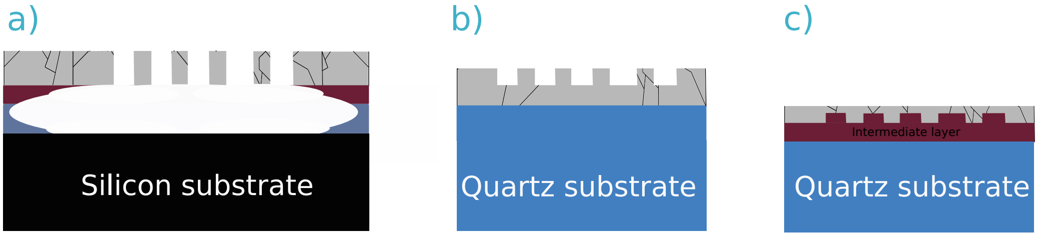

Figure 2.13: Strategies for PhC designs a) suspended membrane on silicon substrate with the light interrogation from the top side of the sample; b) PhC on quartz substrate ; c) PhC embedded inside the diamond film; For b) and c) configurations, the light interrogation is realized from the backside of the sample, thanks to the transparent quartz substrate at visible wavelengths.

#### 2.4.5.1 Incomplete etched holes of 2D PhC fabricated on quartz wafer

In the first example, the 2D PhC was described as being suspended in air (Fig. 2.13 a). From fabrication point of view, the sample is under-etched to fabricate a suspended diamond membrane and to not have interferences with the substrate. The advantage of this configuration is that the detection is acquired from modification of the refractive index from the top and the bottom surface of the diamond. A limitation in the case of a suspended membrane is that when detecting in aqueous or air medium, the solution or the air enters under the structure and make contact with other materials (silicon, silica), that are not functionalized as diamond and that can lead to an accumulation of molecules outside the sensors. From the optical measurement point of view, the light injection and detection is realized from the top of the surface.

A second proposed design is conceived to be fabricated on a transparent substrate on the visible wavelengths, such as quartz substrate. The purpose for developing this method is to optically probe the diamond guided modes from the backside of the sample, offering the possibility for the top part of the sample, where diamond is located, to be used for detection purpose only, while the light is injected from the backside. PhC can be either on the surface (Fig. 2.13 b) or encapsulated in the diamond film (Fig. 2.13 c). In the configuration proposed in Fig. 2.13 b), the holes will not be completely etched over the entire diamond film thickness, thus leaving only the diamond to be in contact with the targeted molecules / gases. The design presented in Fig. 2.13 c) offers a flat diamond surface with 2D photonic crystals embedded inside the sample, with no entrapment sites for biological solution. The drawback of these configurations is that the sensing surface is halved as compared to the Fig. 2.13 a), only the top part of the diamond film is used for sensing.

For both versions of the design on quartz substrate, the strategy to find the best configuration oriented for sensing was the same as presented in the first part of the Chapter on silicon substrate. Band diagrams of this configuration are more complicated to deciphered,

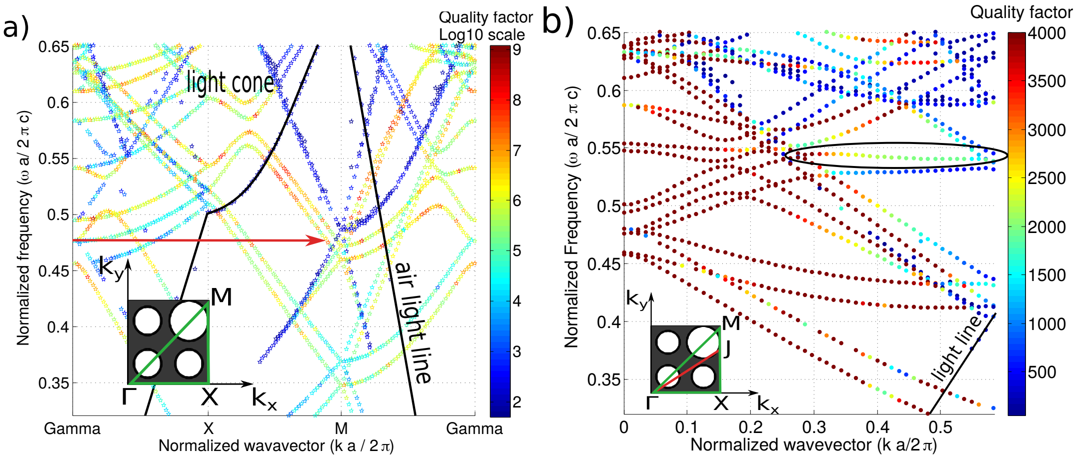

Figure 2.14: a) Band diagram simulation in directions described by the irreducible Brillouin zone for four holes in fundamental lattice cell for a 2D square lattice photonic crystal. Radius of the small holes is 0.16 a, the radius of the big hole is 0.21 a and thickness is a. The inset represents the Brillouin zone Γ, X and M at which the dispersion curves is simulated; b) Dispersion relations of the structure when the interrogation direction is *Γ* J (27° from Γ X direction- depicted in the red line in inset and shown in a) by the red arrow.

because of breaking of the vertical symmetry. However, a configuration with a low group velocity of one diamond resonant mode was found. The band diagram for both versions are similar, that is why I will present the numerical simulations only for one type of the design, namely the one presented in Fig. 2.13 b). The dispersion relation curves of the described structure are calculated in the directions of the irreducible Brillouin zone and its representation is shown in Fig. 2.14 a). Part of the parameters of the structure are slightly changed compared to the silicon substrate design, such as for the small holes from the fundamental lattice cell to 0.16a. The diamond film thickness and the targeted quality factors for desired GMR (up to 5000) are kept the same. By not etching completely the diamond film, the symmetry along z axis is broken, the distinction between TE or TM GMR being no longer valid. A new parameter taken into account was the hole depth in the diamond film. Starting from the band diagram simulated in Fig. 2.14 a) with a hole depth of half of the diamond film, the first suitable GMR is searched to achieve a low group velocity when interrogated to a particular direction. When light is injected at $\phi = 27°$ from the *Γ* X direction, the group velocity of the mode is drastically decreased, as it can be seen in Fig. 2.14 b). The proposed design offers two GMR with low group velocity at different frequencies, with different Q. The targeted GMR is the one found at 0.54 normalized frequency with a Q of 2000.

The design of the PhC structure on quartz substrate has an additional variable parameter, namely the depth of the etched holes in the diamond. In the Fig. 2.15 a), b) and c) are represented three different cases in function of hole depth on the diamond film, simulated in the same conditions. Fig. 2.15 b) is the same structure simulated in Fig. 2.14 b), with the representation of angular dispersion curves versus the normalized frequency. One can observe that the targeted GMR is maintaining the same low group velocity over a large range of incidence angles. The change in hole depth will certainly modify the dispersion relations of the GMRs in the terms of frequency. The group velocity can be reduced in the same way as for complete etched holes i.e., by varying the $\phi$ angle direction. The frequency change is due to the change of the effective refractive index of the PhC, the deeper the holes in diamond film, the higher the frequency of the GMR. In Fig. 2.15 a) is shown the angular dispersion relations when the hole is etched 3/4 of the diamond film thickness. One can observe that the overall Q of the GMRs are decreased. In the contrary, when the holes are etched on 1/4 of the total thickness, the GMRs increases their frequency. The overall increase in the Q is observed and the two GMR pointed out by the gray ellipse are more distant in frequency when compared to the other two cases. The evolution of the Q factor for different hole depths was not further analyzed.

In practice, the fact that the targeted GMR maintains the group velocity for different hole depths represents an asset of the PhC design. A small variation in the fabricated PhC regarding the desired PhC will only change frequency of the targeted GMR, but the dispersion curves remain similar.

Reflectivity simulations were calculated similarly for all the presented configurations from Fig. 2.15. Similar results were found for the corresponding reflectivity spectra, with an intensity approaching unity in the ideal conditions and with an intensity decrease when losses are introduced.

The performances of the designs are calculated similarly as for membrane design. The sensitivity values shown here are for the structure with half diamond film thickness etched holes, with diamond film thickness of a, the small holes of 0.16a and big hole of 0.19a, interrogated in the direction of 30° regarding Γ X direction. The resulted theoretical values are listed in Table 2.2. The sensitivity values expected for this design are similar with the one presented for membrane designs. The smaller value of sensitivity calculated for this design is related to the higher group velocity experienced by the GMR (two times the value found with the previous design). A second factor that limits the sensitivity value is the fact that the sensing occurs only on the top part of the diamond film. It can be also observed that the frequency shift is smaller compared to the one listed in Table 2.1.

The theoretical bulk sensibility values for the diamond PhC on quartz substrate of 2077° / RIU are remarkable, placing the performances of the design above the ones found in the literature for in-plane configuration of PhC or SPR.

I can conclude that the proposed diamond PhC on quartz substrate offers extraordinary sensitivity performances. The design offers the possibility to slow the light propagation

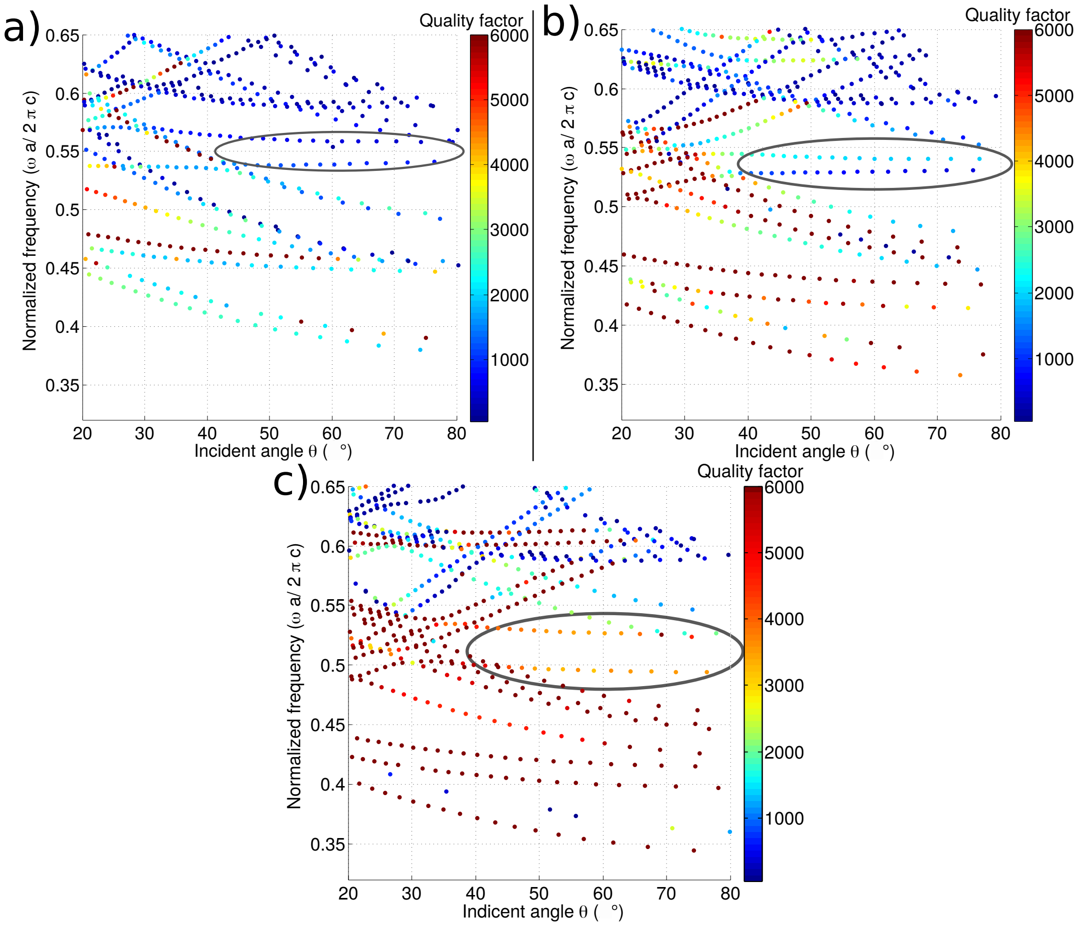

Figure 2.15: Angular representation of 2D PhC structure with four holes in the fundamental lattice, with small holes of 0.16 a, the radius of the big hole of 0.21 a and diamond film thickness of a. The dispersion curves are calculated in the specific direction *Γ* J (27° from Γ X direction). The variable parameter for simulation is the hole depth on diamond film on quartz substrate: a)0.75 hole etch ; b)0.5 hole etch; c)0.25 hole etch

| Polarization | $k_{parallel}$ | $v_g$ | $\theta$ n=1 | $\theta$ $n_{\mathrm{environment}}$ =1.002 | $\Delta\omega\times10^{-4}$ | Quality factor | Bulk sensitivity °/RIU |
|---|---|---|---|---|---|---|---|
| TE | 0.5103 | 0.007 | 80.205 | 80.234 | 0.454 | 1580 | 2077 |

Table 2.2: Bulk and surface theoretical sensitivity values of the two dimensional photonic crystal on quartz substrate, optimized for sensing

inside the PhC, fact that improves significantly the expected sensitivity values. This configuration make possible the light injection from the backside of the sample due to the quartz transparency at desired frequencies, leaving the top part of the surface, where diamond is placed, to be used only for bio-detection purposes.

## 2.5 Conclusion

In this Chapter, I described the photonic crystal parameters that are necessary to model the optical properties of the photonic crystal diamond sensors. Two designs were proposed based on the detection of guided mode resonances of a diamond photonic crystal structure. By choosing a fundamental lattice cell with four holes, with one hole diameter different from the other three, the quality factor of a targeted guided mode resonance can be controlled and tuned at desired values. Due to the control of the light incident angles, it is possible to decrease the group velocity of a targeted mode, fact that led to an increase of the performances of the design. The optical measurement of the device involves light injection from a single frequency source. The design offers the possibility to tune the frequency of the targeted guided mode resonance by more than 8% in term of the wavelength in order to came across the fixed frequency imposed by the light source. This frequency change is possible by changing the azimuthal angle light interrogation direction.

In this Chapter, I proposed two different designs (one suspended in air and another on top of quartz substrate) which were characterized in terms of their theoretical sensitivity values. If the optical measurements are done at a fixed frequency, we have shown that the angular sensitivity is inversely proportional with the group velocity of the GMR of interest, overcoming the limitations imposed by $\lambda/\mathrm{n}$.

These proposed designs improved the expected angular sensitivity values by a factor 10 regarding the existing technologies. These theoretical assumptions represent a step forward in the label-free optical biosensors field.

The following Chapters of this manuscript are dedicated to the development of the fabrication technologies for the realization of the simulated designs. Optical setups are optimized to characterize the fabricated device in order to validate the expected performances.

# Chapter 3

# Micro-fabrication development of diamond photonic crystals

## 3.1 Introduction

The results of numerical simulations gave us the necessary information about the 2D PhC design to realize the device on polycrystalline diamond film. First polycrystalline diamond photonic structures were developed in our group prior to my arrival. The micro-fabrication recipes available served as a starting point for the fabrication of the proposed PhC designs of this thesis. The optimization and development of new protocols for device fabrication with better optical properties and performances were important part of my thesis.

I analyzed each step of the entire technological process in order to reach the optimal parameters for the optical device. For that, the polycrystalline diamond as material was proposed (presented in Chapter 1 section 1.5). The combination of the optical properties of PhC with the physico-chemical diamond properties are well suited for biosensor demands. Polycrystalline diamond was favored to monocrystalline one because of the possibility to grow large samples (2-inch in my case), with relative low cost and while benefiting a very broad knowledge of growth from a few hundreds of nanometers to several micrometers. The growth conditions and the choice of reactor for polycrystalline diamond on large surfaces are studied in order to acquire better optical performances than what was previously done.

The rest of this Chapter is dedicated to the processes that are necessary to realize PhC biosensors in clean room facilities, with high quality factors.

The proposed device was designed to work at the limit of visible wavelength range. This implies the fabrication of smaller structures to be able to function at the desired wavelength.

Thicker polycrystalline diamond films than previously proposed works were considered for PhC device micro-fabrication to yield better optical performances of the devices. We will describe the method and the optimization strategies for polycrystalline diamond surface smoothing process realized by flowable oxide spin-coating, followed by dry etching method.

The performances of the biosensor depends in part on the quality of the material. A transfer onto silicon substrate with silica as intermediate layer was previously proposed. This process was developed to realize the PhC structures on the better crystalline quality part of a thick diamond film. Starting from this recipe, we will propose a new polycrystalline diamond film transfer protocol onto new substrate on two different substrates, namely silicon and silica substrates.

Thanks to the technological process of polycrystalline diamond film planarization, the fabrication of photonic crystal structures was possible by using electronic beam lithography method. We will describe in this Chapter all of the intermediate steps necessary for realizing PhCs.

The existing dry etching diamond recipes were necessary to be transferred onto a new dry etching system. The optimization and the development of new dry etching recipes on the new system will be presented. The samples are characterized by different methods (scanning electron microscopy, atomic force microscopy) at different stages of the device fabrication and the results are shown and discussed throughout the Chapter.

Each of the processes will be largely explained, covering the reasoning of preferring one over any another possible and the optimization steps that lead to the final process.

## 3.2 Synthesis of diamond thin film for photonic structures

As shown in Chapter 1, diamond is a material with good perspectives for the photonic field. Unlike other materials where decades of research was done to develop devices (Si, III-V semiconductors), nano- and micro-fabrication of devices using diamond started about a decade ago, with the interest of different teams ([43, 44, 45, 48, 51, 52, 50, 55, 49, 54]).

When analyzing the polycrystalline diamond, one important characteristic to take into account is the presence of grains boundaries as compared to monocrystalline diamond. The grain boundaries have different chemical composition (it reacts differently compared to bulk diamond), making the task of constructing structures on this material more difficult. Also, from the optical point of view, these grain boundaries are considered as defects, being one of the factors that lowers the quality factor of the PhC. The grain size varies in function of the thickness of the film because of the selective columnar growth mode, hence the interest to grow thick layers of diamond with fewer grains.

My thesis work was done in Centrale de Technologies Universitaires (CTU) MINERVE clean room at C2N Orsay laboratory, where samples up to 2 inch were processed, whereas the growth of diamond on different substrates was carried out at CEA Saclay at Laboratoire

| Property | Value |
|---|---|
| Transmission | 225 nm until far IR, with a residual absorption at $\sim$ 10 µm |
| Refractive index | 2.41 at 500 nm; 2.38 at 10 µm |
| Absorption coefficient | $< 0.1$ cm$^{-1}$ at 10 µm |
| Dielectric constant | 5.7 |

Table 3.1: Optical properties of CVD diamond

Capteurs Diamant (LCD).

### 3.2.1 Chemical Vapor Deposition diamond growth

Diamond is an allotrope form of carbon. It can be found in nature in many shapes, sizes and purities. Natural diamond cannot be modified to answer the demands desired in all possible fields. Each piece of natural diamond is different from the another, leading to different properties. In order to obtain better reproducibility of the physico-chemical diamond properties, methods for diamond synthesis were developed. In this way, coatings and films on a variety of shapes and thicknesses can be obtained.

In the table 3.1 are listed the principal optical properties of diamond.

There are two methods to synthesize diamond : the first one recreates the natural conditions for diamond formation, namely High Pressure / High Temperature (HPHT) and the second one consists in diamond synthesis by Chemical Vapour Deposition (CVD) method.

**Monocrystalline diamond by HPHT method :** HPHT is the method used for the realization of monocrystalline diamond, meaning that the obtained diamond is represented by a single crystal. Nitrogen is required for this type of synthesis, which represents an impurity from the optical point of view. Nitrogen incorporation into the diamond structure increases the absorption ([65]). This characteristic represents an inconvenient for diamond use in integrated optics. Furthermore, HPHT method allow realization of small areas of monocrystalline diamond (a few mm$^2$ available at high price). Industrialization of this type of synthetic diamond is used only in the challenging fields, such as power electronics.

**Synthetic diamond growth by Chemical Vapour Deposition :** The CVD was developed in the early 1980s by a Japanese group. They published a series of articles containing different methods of diamond growth, namely hot-filament CVD process, RF-plasma CVD and microwave plasma CVD ([66, 67, 68]). They reported that diamond particles and films can be deposited on various substrates when heated at around 850 °C, using a gas mixture between methane diluted by hydrogen at pressure ranging between $4 - 5 \times 10^3$ Pa. The methods developed by the Japanese group were taken by other groups and intense research was made to understand the mechanisms of CVD growth (nucleation, structuring, diamond doping etc). Typically, the growth speed of diamond films range between 0.1 and 10 µm / hour, depending on the ratio of $CH_4/H_2$ (an increased amount of methane accelerates the growth process, but decreases the crystalline quality of the obtained diamond films).

Using CVD method, different diamond types can be obtained, depending on the substrate nature, the gas mixture, the temperature, impurity percentage or the geometry of the reactor. CVD diamond can be monocrystalline or polycrystalline.

For the monocrystalline diamond grown by CVD, the substrate needs to be natural or HPHT diamond, where the growth is realized homoepitaxial. The purity of the deposited film is controlled by the purity of the gas mixture during the synthesis process. Although this type of synthetic diamond possess the best optical properties in transmission, the surfaces that can be grown are at maximum $8 \times 8\ \mathrm{mm}^2$. This drawback renders the monocrystalline diamond grown by CVD difficult to process using the micro-fabrication technologies.

For this PhD thesis, we are interested on the second type of CVD diamond, which is the polycrystalline diamond type. Films can be obtained on large surface areas due to the fact that it can be deposited on different substrates (hetero-epitaxy)([69]). However, this type of synthetic diamond posses lower crystalline quality because of the grain boundaries. The film thickness range between a few hundreds of nanometers to several micrometers, with a surface roughness of 10%, and can be deposited up to 4 inch substrates.

Before my arrival, LCD team developed recipes for growing polycrystalline diamond films by Microwave Plasma assisted Chemical Vapor Deposition (MPCVD) onto silicon and quartz substrates, with thicknesses ranging from a few hundreds of nanometers to several micrometers while keeping a good thickness uniformity of the film on the entire wafer.

Diamond growth by MPCVD starts from nanodiamonds previously deposited on the surface, named also seeds, which act as starting sites. These nanodiamonds will grow in size in all directions and at the meeting interface of two neighbor nanocrystals will be formed the grain boundary, because the crystal orientation of two neighboring grains is not necessary the same. These grain boundaries contain amorphous carbon and/or graphite, as well as structural defects (dislocations, twinning, voids, etc). Due to the selective columnar growth of diamond, as the thickness increases, the grains will become bigger, with the possibility to have grains of micrometer size for a few micrometer film.

The assumption was made that the grain boundaries induces light absorption due to their amorphous carbon nature, increasing the losses of the material, thus implying the decrease of the device performances. The density of the grain boundaries is smaller for thick diamond films, from where the interest to have thick diamond films to diminish these presumed optical losses. However, it is known in literature that increasing the film thickness, the roughness will also increase. We will discuss later in this Chapter what is the maximum roughness that we can manage.

When referring to optical losses, the precursor gases injected into reaction chamber can induce a doping into the diamond film, which conduct to the modification of the optical properties. For example, a few amount of nitrogen gas injection increases the deposition rate ([70, 71]), but it will introduce new optical losses in the visible range.

#### 3.2.1.1 Substrate for diamond growth

Synthetic diamond can be grown on many different substrates. I will restrict the list by presenting the ones that form a strong carbide formation (bonding) with the diamond film, have a melting point higher than the diamond growth and have a thermal expansion coefficient close to the one of diamonds. As examples I can mention silicon, quartz ($SiO_2$), silicon nitride ($Si_3N_4$), silicon carbide (SiC), titan carbide (TiC), tungsten carbide (WC) or metals, such as Ti, Nb, Cr, Mo, W ([69]). Among all the presented substrates, I choose to work on silicon and quartz substrates because growth recipes for polycrystalline diamond films on these substrates are well known by LCD group, with the possibility to deposit films on samples up to 2 inch wafers.

Silicon substrate is commonly used in micro-fabrication and all technological processes involved in device fabrication are compatible with silicon, such as Plasma Enhanced Chemical Vapor Deposition (PECVD), etching, electronic beam lithography. Silicon wafers can be found on different sizes, and during this thesis I used 2 inch wafers. When used as substrate for diamond growth, Si (100) type has been chosen for the ease of cleavage or sample cut when needed for PhC fabrication. The temperatures reached during the growth process are around 800°C, a temperature which gives a good compromise between the crystalline quality and the growth rate. The melting point of silicon material is way above this temperature (1414°C), meaning that there is no restriction from this point of view. Diamond is known as having a very low expansion coefficient when heated at 800°C and then cooled down at room temperature ($0.8 \times 10^{-6}\mathrm{K}^{-1}$) ([69]). The silicon substrate has comparable thermal expansion coefficient ($3 - 5 \times 10^{-6}\ \mathrm{K}^{-1}$), an important property that prevents the appearance of cracks or film delamination when the material is heated up/cooled down on diamond film.

The second material substrate used during this PhD thesis was quartz ($SiO_2$). It was chosen mainly because of its optical transparency at visible wavelengths and offers a different/ easier optical characterization of the final device, as I will describe in details in the characterization Chapter IV. Quartz wafer of 2-inch and $20 \times 20 \quad \mathrm{mm}^2$ were used during this thesis. Quartz has higher thermal expansion coefficient ($8 - 14 \times 10^{-6}\ \mathrm{K}^{-1}$) as compared to silicon wafer. As consequence, the temperature during the growth process was

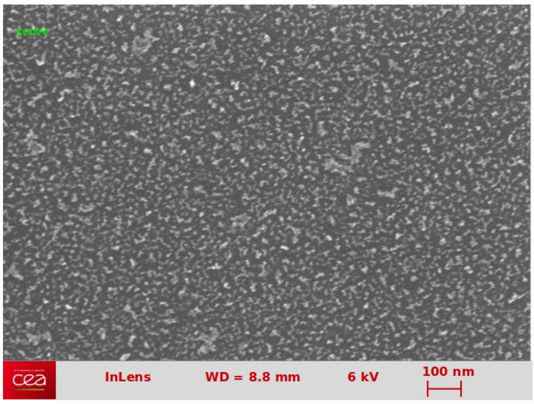

Figure 3.1: HRSEM image of silicon substrate covered by diamond nanoparticles

decreased at ~ 600°C to prevent film delaminaton or cracking due to thermal stresses.

#### 3.2.1.2 Nanodiamond deposition before CVD diamond growth

The first step of the diamond film growth is the deposition of the nanodiamonds (NDs) on the wafer surface, which will act as starting sites. The process needs to be performed in dust free environment to avoid any contamination.

Starting from the previous work done in our group by C. Blin during her PhD thesis and H. Girard work from LCD group, the protocol for NDs seeding onto the substrate prior to diamond film growth by MPCVD deposition has been developed ([63, 72]). Firstly, the substrate was immersed in positively charged poly (diallyl-dimethyl-ammonium-chloride) (PDDAC) solution at 0,2 wt % concentration for 15 minutes and then immersed for 1 hour in negatively charged HPHT NDs obtained by detonation at 0.05% wt concentration. The protocol shows a homogeneous distribution of NDs on surface, a very good reproducibility and a high density of diamond nanoparticles on the surface ($> 10^{11}\text{cm}^{-2}$) ([72]). Sample characterization was done by High Resolution Scanning Electron Microscopy (HRSEM) to observe the uniformity of diamond nanoparticles distribution and also to ensure that there are no aggregates on the surface. Fig. 3.1 shows a HRSEM image of a silicon wafer covered by dispersed NDs.

#### 3.2.1.3 CVD reactor for the growth step

After the seeding step, the actual growth of diamond films is held in a reactor. The best suited reactor at LCD is DIADEME reactor (“DIAmond DEvelopment for Micro-Electronics’). Different growth conditions were developed before my arrival on silicon and quartz substrates of sizes up to 2-inch large, showing a good reproducibility and thickness uniformity.

During my thesis, I realized samples with the growth conditions that were already in place

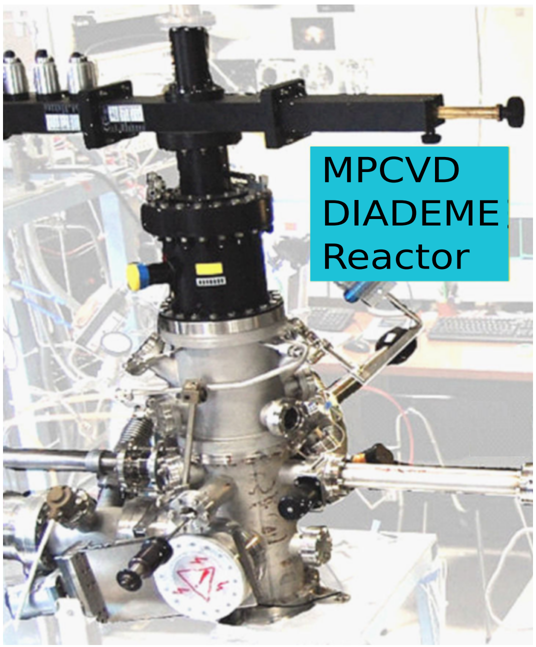

Figure 3.2: Image of the DIADEME system ([74])

to create diamond films with different thicknesses. Also, I developed new growth conditions for polycrystalline diamond to change the morphological structure of the diamond grains. The aim was to decrease the surface roughness for thick diamond films by favoring specific crystallographic planes to emerge. DIADEME reactor will be detailed and the parameters and the results for different recipes will be discussed in the next paragraphs.

DIADEME system is comprised from a MPCVD reactor for the growth of polycrystalline diamond films, as shown in Fig. 3.2. The plasma is produced by a magnetron from SAIREM company at 2.45 GHz frequency and maximal power of 2 kW. During the process, the temperature inside the chamber reaction reaches 800°C at the surface of the wafer and as a consequence the reactor is cooled down using a water system. The electromagnetic waves generated by magnetron are transmitted using waveguides up to a coupling antenna which is placed on the top part of the reactor, just above the sample holder. The antenna is adjusted to emit the microwaves with maximum intensity above the substrate holder (resonant cavity), fact that makes the plasma the most dense at that point, which leads to the increase of the growth rate. The CVD growth process can occur at pressures ranging from 10 to 100 mbar. The rotation of the sample holder increases the thickness uniformity of the deposit on 2 inch wafer. Samples with less than 5% thickness difference from center to edge can be obtained ([73]).

The gases (methane, hydrogen, argon or nitrogen) are injected in the reactor's chamber, where the constant flow rate is maintained using mass flowmetres. The plasma is generated by gas molecules ionization under intense microwave electromagnetic field. The geometry of

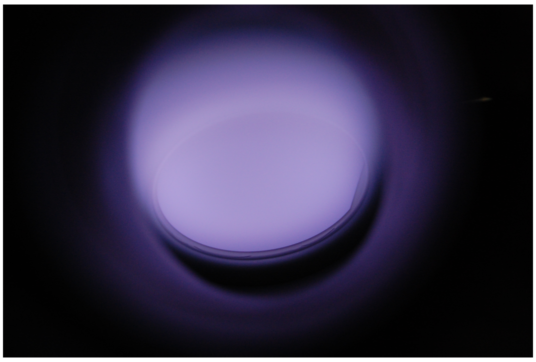

Figure 3.3: Plasma generated inside DIADEME reactor

| | Gas 1 | Gas 2 | Gas 3 | Gas 4 | Gas 5 |
|---|---|---|---|---|---|
| Gas | H2 | CH4 | H2/N2 | O2 | Ar |
| Coef. | 1 | 1 | 975 | 1 | 1,4 |
| Max | 500 | 20 | 1 | 20 | 1000 |
| Rec. % | 49,7 | 7,5 | 0 | 0 | 0 |
| % Vol | 99,4 | 0,6 | N2 ppm 0 | 0 | 0 |
| Actual % | 49,45 | 7,527 | 0 | 0 | 0,0170 |
| | Line 1 | Line 2 | Line 3 | Line 4 | Line 5 |

Flow control (SCCM) 250
Rec. Pressure (mBar) 35
Power 1100
☑ Local to 0 ?
Foward Power 1078 Watts
Reflected Power 1 Watts
Reactor pressure 34,9 Baratron mbar
Gaz recipe No Recipe
Output file 0270417a.xls
Period (s) 1
Graph source for calculation No calculation
Mean 0
Std. Dev. 0
Laser Lock-in 0
Frequency (Hz) 0
Value (mA) 0
Duration(s) 54000
Elapsed(s) 315
Remain (s) 53685
Thickness (nm) 0
Remain (nm) 0
☐ Julien ☐ Jean-Charles
☑ Petru ☑ Samuel
Est. Thickness (nm) 0,0
G.R. (nm/h) 0
Half periods 0
Trigger (s) 60
°C 494
Inpac Coef. 1
Max Pressure 90
☐ Stop on failure
This condition override the permanent 90mBar security.
Max T° 900
T° Autoset
Min T° 300
☐ Stop on failure
Max Reflected 100
☐ Stop on failure
Autostop is on
Transfert schedule
Don't use reactor when yellow light is on, please. Transfert is about to be done.
People to warn when pressure is OK:
☐ Julien ☐ Jean-Charles
☐ Petru ☐ Samuel
Laboratoire Capteurs Diamant
Arrêt prévu : vendredi 28 avril à 09:32
Pilotage de Diadem V1.95

Figure 3.4: Diademe system user interface LabView

the chamber is optimized to generate the plasma above the substrate holder of the sample and therefore the diamond growth process (Fig. 3.3).

The user interface with the reactor was developed under LabView by LCD DIADEME users. The software controls and displays in real time all the parameters involved during the process, such as microwave power injection, reflected power, pressure, gas flow rates, temperature and process time, along with a series of securities to stop the process if parameters are out of tolerance during process (Fig. 3.4).

#### 3.2.1.4 Parameters

Depending on the desired diamond structuring, the choice of the parameters mentioned above influences the diamond grain crystallographic orientation, grain structure or growth rate. Table 3.2 summarizes the growth conditions for polycrystalline diamond on silicon and quartz substrates used in DIADEME reactor. The parameters of the first two recipes from the table were optimized by LCD group before I started the PhD. Regarding the third recipe, I changed the initial recipe for silicon substrate growth to achieve diamond film with lower surface roughness values for thick films.

| Parameters | Silicon substrate recipe | Quartz substrate recipe | Silicon substrate planarization recipe |
|---|---|---|---|
| Pressure mbar | 35 | 22 | 60 |
| Temperature °C | $\sim 800$ | $\sim 600$ | |
| Total gas flow rate sccm | 250 | 250 | 500 |
| Percentage $CH_4$ % | 0.6 | 0.6 | 0.3 |
| Percentage $H_2$ % | 99.4 | 99.4 | 79.7 |
| Flow rate $N_2$ ppm | - | - | 40 |
| Percentage Ar % | - | - | 20 |
| MPCVD power W | 1100 | 700 | 1100 |

Table 3.2: Growth conditions for polycrystalline diamond on silicon substrate used in DIADEME reactor

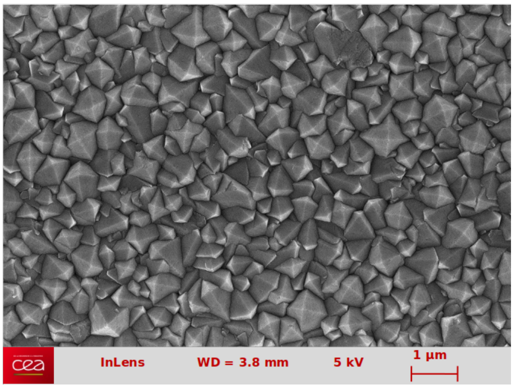

Figure 3.5: HRSEM top view of a polycrystalline diamond film deposited in DIADEME reactor with 3 µm thickness, using the standard growth conditions

**3.2.1.4.1 Standard diamond growth conditions :** In the case of polycrystalline diamond growth on silicon substrates, the growth conditions are listed in Table 3.2. Optical measurements indicates a growth rate of 120 nm/hour in average. In the case of a thin film deposition, namely 400 nm, the process takes less than 4 hours, but for 5 µm thick film, the process time required is around 42 hours. The growth process is long and was being one of the reasons for limiting the thickness to a maximum of 5 µm. I used HRSEM technique to analyze the grain morphology and to measure the grain size. In the Fig. 3.5 is presented a top view example of 3 µm thickness film grown in DIADEME reactor using the growth conditions mentioned in Table 3.2, which promote {111}{100}<100> texture, where {111}{100} are the majority of the faces and the <100> is the principal axis. This texture is induced because of the selective growth associated to diamond crystal having a morphology closed to the octahedron ([75]).

When substrate was changed to quartz, the growth conditions were changed to decrease

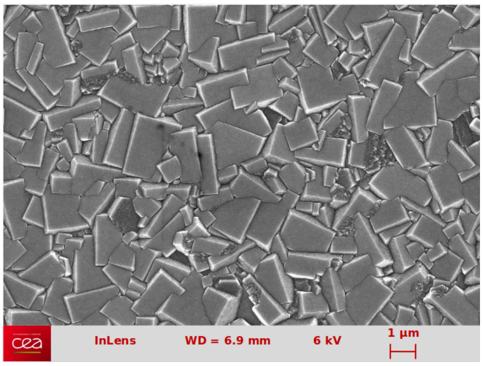

Figure 3.6: HRSEM top view of a polycrystalline diamond film depostited in DIADEME reactor using the growth conditions to decrease the surface roughness

the temperature on the wafer. Quartz has a thermal dilatation coefficient of $8 - 14 \times 10^{-6}$ K$^{-1}$, value that is superior to that of silicon material ($3 - 5 \times 10^{-6}$ K$^{-1}$). To avoid cracking or delamination, a decrease of the microwave power to 700 W and of the pressure to 22 mbar were enough to grow polycrystalline diamond film with the same morphology as in the silicon substrate case, with the drawback that the growth rate is decreased to 75nm/hour.

**3.2.1.4.2 Modified growth condition for roughness decrease :** Starting from the presented growth conditions, I applied a recipe that decreases surface roughness directly during the growth process. After the formation of the {111}{100}<100> texture, the morphology of the grains are changed from octahedron to cuboctahedron. Then, the small {100} faces at the top of the pyramids open. The modification of the pyramid crystal morphology is done by changing the temperature of the deposition process. Then the texture evolve towards {100}{111}<100> and the morphology evolution of the crystal lead to a reduction of the roughness as illustrated in Fig. 3.6. This change was possible for 3 µm diamond films that were already deposited with conditions from Table 3.2 and showed in Fig. 3.5 a). The process was continued for several hours with higher process pressure and gas flow rate as well as introducing argon and nitrogen gases inside the chamber to speed up the growth rate. At the end, the film growth rate was accelerated to 280 nm/hour. Unfortunately, these parameters lead to film delamination from silicon substrate because of the growth temperature increases on the sample surface, implying relaxation (dilatation) of the silicon material due to its slightly higher thermal coefficient that of diamonds. The results obtained by changing growth conditions were not satisfactory enough for our demands. A different method was searched for the surface planarization of the polycrystalline diamond film.

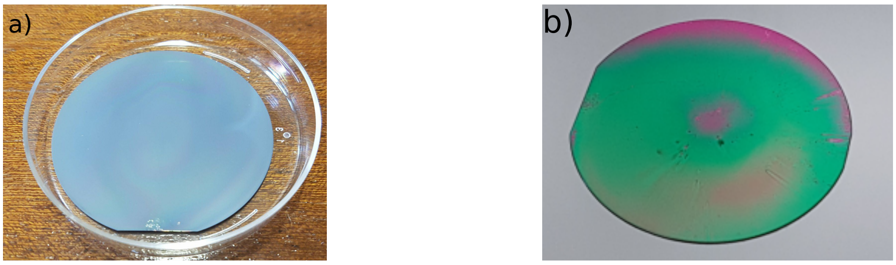

Figure 3.7: Polycrystalline diamond film grown on 2 inch silicon wafer : a) 5µm film; b) 470 nm film (image of the sample after planarization procedure)

### 3.2.2 Diamond characterization

The film thickness was measured by reflectometry. This method analyzes the interference fringes resulting from the reflections at diamond / silicon and diamond / air interfaces. It is the most used technique to measure at the nanometer scale film thicknesses starting from a few hundreds of nanometers until few micrometers. Measuring the sample in different points of its surface, the uniformity is defined as in Eq. 3.1:

$$\mathrm{th} = \frac{\mathrm{th}_{\mathrm{max}} - \mathrm{th}_{\mathrm{min}}}{\mathrm{th}_{\mathrm{max}} + \mathrm{th}_{\mathrm{min}}} \times 100 \tag{3.1}$$

where $\mathrm{th}_{\mathrm{max}}$ and $\mathrm{th}_{\mathrm{min}}$ are the maximum and minimum thicknesses measured on the sample, respectively. A small uniformity value over the whole sample is important because photonic device need to have a precise diamond thickness for use at a specific wavelength. For that I targeted uniformities below 10%. In Fig. 3.7 a) is shown a 5 µm diamond film on silicon substrate with uniformity of 6%. The uniformity can also be estimated with the naked eye from the wafer colors for thin films under 1 µm (Fig. 3.7 b). An uniform color represents a good uniformity and in the presented case the uniformity is 6%.

To conclude, polycrystalline diamond films ranging from 450 nm to 5 µm thickness were deposited by Microwave Plasma assisted Chemical Vapor Deposition. The film deposition was realized on two different substrates, namely silicon and quartz substrates. The growth parameters were almost the same for the two substrates, with the mention that the temperature was decreased in the case of quartz substrate to prevent film delamination. Polycrystalline diamond films with uniformities of 6% were deposited on 2 inch samples.

## 3.3 Planarisation process

### 3.3.1 Aim of the study

Due to the selective growth conditions and the grain morphology of deposited polycrystalline diamond, the sample will have a rough surface, as seen in Fig. 3.5. Depending on the demands of the final device, this aspect may not be influencing its good functioning, as in the case of electro-chemistry ([76]). However, in many other cases, the roughness of the films and different grain sizes with different crystallographic orientations is a limitation. Applications include high-frequency communications, Micro-Electro-Mechanical Systems (MEMS), Surface Acoustic Wave (SAW) devices, diamond semiconductors or optic sensors, where the surface roughness must be controlled.

One goal of my thesis is to fabricate a 2D photonic crystal structures for detection in the visible wavelengths range. For that, numerical simulations were performed to optimize the design structure (Chapter 2) and the results indicate that the PhC hole diameters are in the range of one hundred nanometers. To fabricate these holes, the peak-to-valley (PV) of the film at least needs to be smaller than the hole diameter to realize with accuracy the desired structure on diamond. Typical desired values diamond film thickness are in the range of 370-400 nm, with electron beam resist of 135 nm and a hard mask layer of 105 nm. The technological processes will be discussed in detail in the following paragraphs.

I presented these values required for fabrication of the 2D PhC to accentuate the scale at which the technological fabrication occurs. The polycrystalline diamond film after growth presents different roughness RMS values in function of the film thickness, measured by reflectometry. In the case of my samples, the roughness RMS value is estimated to be in the order of 40 nm for 470 nm thick film and around 600 nm for 5 µm thick film, with peak-to-valley values which we assume that overcome 100 nm and 1.2 µm respectively. The presented values are rough approximations based on reflectometry measurements and HRSEM images. AFM measurements were not performed after the polycrystalline diamond growth to precisely determine the roughness RMS and PV values. In the next section I will explain the necessity of growing 5 µm polycrystalline diamond film, even if the desired thickness for the PhC is only a small part of the total film.

These roughness values are too important to be able to define the patterns onto diamond with high fidelity. Also, surface roughness induces optical losses when light is injected on PhC, in which case the structure's quality factor is lowered. Considering that other materials, like silicon, have surface roughness smaller than one nanometer ([77]), to attempt to be comparable with them, a planarization step is required.

During my work, I tried different strategies to lower the roughness RMS values, starting directly from MPCVD film growth to Chemical Mechanical Polishing (CMP). The method which gives the best results is the transfer of the planar surface of an oxide spin coated on the sample and dry etched by Inductively Coupled Plasma (ICP) method.

The technological clean room process begun onto 2-inch diamond samples. A compromise was made to fabricate PhC onto quarters of 2-inch wafer, size that is easier to manage than a 2-inch wafer, with the possibility to fabricate thousands of different structures on the same sample.

### 3.3.2 State of the art and available processes

Many planarization concepts were studied to reduce the roughness of polycrystalline diamond films, such as laser planarization, thermo-mechanical etching, plasma etching ([78, 79, 80, 81]) or modification of the diamond crystal morphology, shown in paragraph 3.2.1.4.2.

When mentioning diamond planarization, one can consider two different approaches. The first one is the sample planarization by classic mechanical polishing methods. These approaches are suited for thick polycrystalline diamond films. For example, in the work done by Roy ([82]), they succeeded to decrease surface roughness RMS from 2,65 µm to 127 nm after classical mechanical polishing. Diamond is extremely hard and it is very difficult to remove it with other materials. Also, due to the nature of polycrystalline diamond, for thin films in the order of few microns, the physical resistance at the grain boundaries is different when compared to the bulk resistance of diamond crystal. It is then possible that grains are detached during mechanical polishing. To not destroy the material, the material removing rate is low and time consuming.

A second method is proposed by Vivensang *et al* ([83]), where an oxide film is deposited on the surface and then dry etched by Reactive Ion Etching (RIE) method. A decrease in the surface roughness RMS from 40 nm to 5 nm was obtained, result that opened the development of this technique by other groups. Rabarot *et al* ([84]) optimized the method and combined it with chemical mechanical polishing method to obtain roughness RMS values of one to three nanometers.

The strategy that was previously developed in the group was to deposit a flowable oxide layer (hydrogen sislesquioxane HSQ) by spin-coating which planarize locally the surface, and to dry etch by ICP method the HSQ layer and the diamond at the same speed, transferring the planar surface from the HSQ resist onto diamond. The technological steps are represented in the Fig. 3.8 and are discussed in C Blin PhD thesis ([63, 85]). Here are detailed the optimization of these processes.

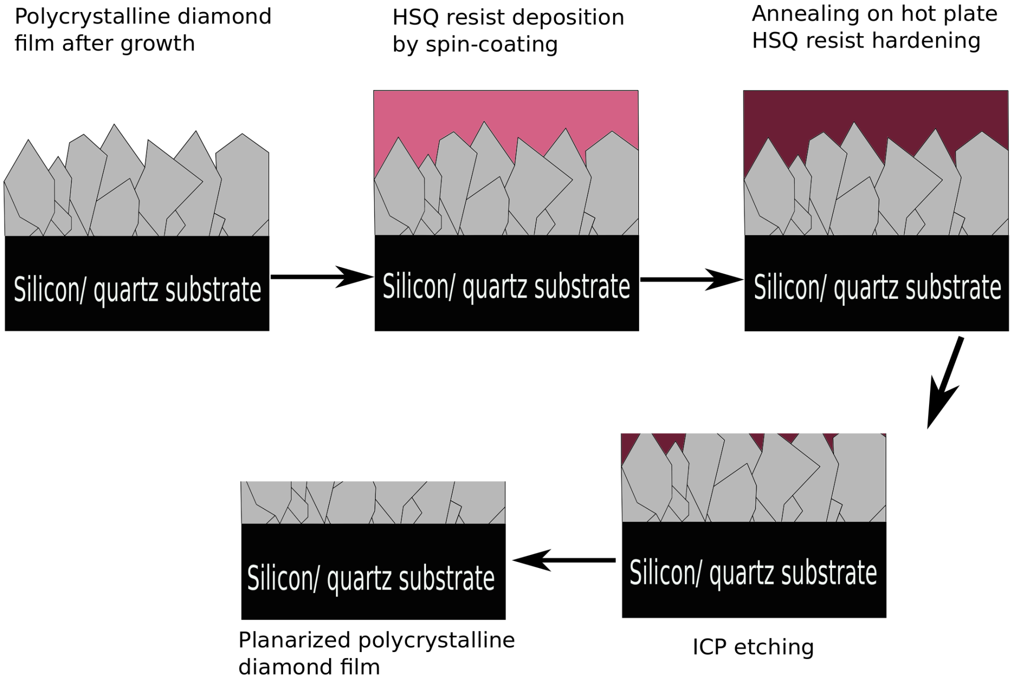

Figure 3.8: Technological steps for polycrystalline diamond film planarization [63]

### 3.3.3 Chemo-Mechanical Polishing of a silica layer deposited on diamond film as grown

The strategy for planarizing polycrystalline diamond films previously developed in the group is useful for thin films, where the sample is covered with the resist with one deposition by spin-coating. The maximum thickness possible to spin a homogeneous film is 750 nm. For thick diamond films (5 µm), the peak-to-valley (PV) of the diamond film overcomes this value. During Blin's PhD thesis, the deposition of a second layer of HSQ resist led to film cracking when annealed. Knowing that the deposition of thicker HSQ layers was not possible, I firstly tried to lower the surface roughness RMS by PECVD silica deposition on top of the diamond, followed by chemo-mechanical polishing. HSQ resist spin-coating was performed afterwards to obtain a global and local roughness RMS values below 1 nm, followed by dry etching of the diamond using ICP. The deposited PECVD silica follows the surface roughness of the sample (Fig. 3.9) and no significant roughness reduction was attended. The use of chemo-mechanical polishing was intended to decrease sufficiently the surface roughness in order that one spin-coating of HSQ resist is enough to planarize locally the surface, as presented in Fig. 3.8 and also to preserve / improve the homogeneity of the sample.

The size of the tested samples was one quarter of 2-inch because this wafer size will be used during PhC fabrication. The first test was done on silicon wafer without diamond with 2 µm PECVD silica to optimize the CMP process parameters. The sample is polished using

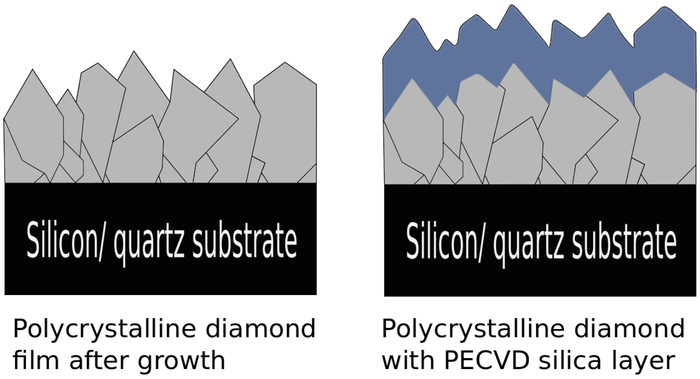

Figure 3.9: Side view of polycrystalline diamond film (gray color) covered by PECVD silica (blue color layer)

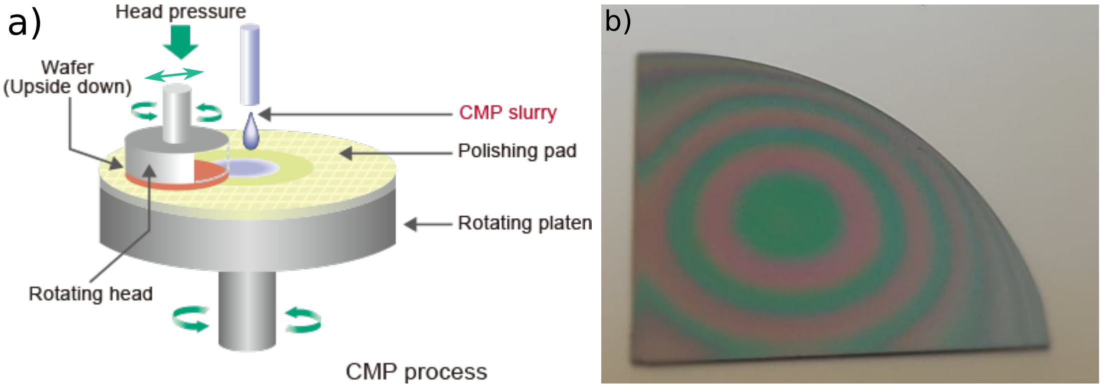

Figure 3.10: a) Schema of chemo-mechanical polishing machine [86]; b) Image during CMP process optimization of $SiO_2$ PECVD on silicon substrate

the PERE machine from MECAPOL company available in the laboratory, with 1 µm grain size pad and silica colloidal slurry as chemical solution. The schematic of this machine is shown in Fig. 3.10 a).

The sample was glued to the sample holder as plane as possible to ensure a proper alignment with the polishing pad. The sample was mounted on the machine with the oxide face downwards, to be in contact to the pad. During the process, the sample holder was rotated on its own axis and also oscillates radially with the polishing pad. Abrasive solution slurry that flows on the pad's surface was utilized for material removing on the sample, the slurry entering between the abrasive pad and sample. A series of studies were performed, where parameters such as applied pressure, pad and arm speed or pad morphology were changed. Similar recipe parameters found in ([87, 88]) were tested. Measurements show that the material removal rate at the center is lower than the one at the borders. It can be observed by the naked eye thanks to color interference (Fig. 3.10 b). After trying different strategies changing the previous mentioned parameters, I could not remove uniformly the silicon oxide layer using CMP method using the available machine at the laboratory. The homogeneity of the sample was degraded, leading to 1.2 µm difference from the center to board of the sample after a few minutes of process. The same behavior is expected with polycrystalline diamond samples with PECVD silica, experiments that I did not perform. The homogeneity cannot be improved by HSQ resist because the planarization is done locally on the sample when spin-coated.

To conclude, the surface roughness decrease using CMP method was not possible for our samples. In the next paragraph I will present the strategy that was proposed to solve this issue.

### 3.3.4 Processes developed for surface planarisation method

I previously presented the strategy to lower the surface roughness RMS for the diamond film with silica layer on the surface using CMP method. The results were not satisfactory and I returned to the technological processes that were already optimized for thin films (Fig. 3.8). As already mentioned, 750 nm is the maximal thickness possible for spin coating the flowable oxide on diamond film. The aim of the new recipe was to deposit a HSQ film twice as thick as what was done before to completely cover the diamond film and to anneal in such a way to achieve a 1.5 µm HSQ film without any cracks.

#### 3.3.4.1 Flowable oxide spin-coating on polycrystalline diamond samples

HSQ is an inorganic polymer with the chemical structure $\left[\mathrm{HSiO}_{3/2}\right]_n$, with excellent gap-filling and local self-planarization properties, that can be spin coated on substrates with a good thickness control. Studies of HSQ resist behavior when annealed were conducted by different groups ([89, 90]). Between 250 and 450°C there are chemical changes that lead to weight loss of the film and above 650°C, the HSQ is transformed to porous silicon oxide structure ([90]).

Different commercial HSQ resists are available, depending on the desired thickness ([91, 92]). For our studies, FOX 15 and XR 1541 6% were utilized. The first one, for thick film deposition (440 to 740 nm), was spin-coated at different speeds (from 5000 rpm to 1000 rpm). The annealing step was conducted on a hot plate in such a manner that the evaporation of the solvent would occur slowly and to limit the formation of air bubbles. The return to the room temperature was done slowly to prevent film cracking. The annealing process was done starting from room temperature on a hot plate and temperature was raised up until 80°C and maintained for 10 minutes. The temperature was further raised until 150°C for 10 minutes and at 250°C for another 10 minutes, then cooled down to room temperature on the plate. Using these baking parameters we succeeded to deposit two layers for 1,5 µm total thickness without any cracks on the surface and without the use of a furnace (as previously used in C. Blin process [63]). An important result was that the thick HSQ film did not crack when the ICP process was performed. The spin-coated thickness with two layers of FOX 15 cover completely the diamond film, this result allows us to process 5 µm thick diamond films.

Deposition of 3 layers of HSQ of 750 nm was tested using the same protocol. After 3 layers were deposited on the surface, cracks appear all over the surface after sample annealing, meaning that the maximal diamond peak-to-valley (PV) that can be handled is around 1.5 µm. Growing thicker diamond films will increase the surface roughness above this threshold and for processing them, another planarization method needs to be optimized.

In the case where the surface roughness is small, the choice of a thinner HSQ deposition is possible. XR 1541 6% can be spin-coated onto samples with thicknesses ranging between 120 and 200 nm (5000 rpm to 1000 rpm). The annealing process was way quicker, 10 minutes at 150°C were enough to sufficiently harden the HSQ and behave similarly when etched as FOX 15. For both HSQ resists, the optimal spin-coated thickness needs to be around 30% thicker that the PV of the diamond film, in order to be sure that the HSQ well covers the entire surface.

The diamond samples were cleaned firstly by acetone, isopropanol and $H_2O$ deionized (DI) water. They were then immersed for 5 minutes in a piranha solution, a mix of $H_2SO_4$/ $H_2O_2$ ratio 3:1, finishing by washing the samples with DI water and dry them with $N_2$ gas stream. This second cleaning step eliminates all organic contaminants. Once the diamond wafer has been cleaned, HSQ solution was spin-coated on the surface to entirely cover the diamond film. The wafer is annealed on a hot plate with the protocol detailed in the beginning of this part.

#### 3.3.4.2 Recipe development for polycrystalline diamond dry etching

The ICP method is widely used in the micro-fabrication industry ([93, 94, 95]). Higher etch speed rates can be obtained, compared to other techniques, such as RIE. Etching process can be obtained by two type of phenomena: a chemical process where a reaction between ionized species and material occurs, and a second physical process, where the acceleration of ionized species is enough to remove material from substrate. When developing a new etching recipe, the parameters that can be controlled are: the gas mixture at different flow rates, the coil power, the platen power, the pressure and the carrier wafer temperature ([94]).

Diamond, due to its physical properties, is known as being one of the hardest material on earth. Studies ([96, 97]) shown that diamond can be etched using different gases, with $O_2$ being the most effective. Using Ar as etching reactant helps the process to flatten the surface and indicated a regime of physical sputtering with low etch rates([98]). During the etching process, the Ar ions mainly etch the annealed HSQ resist, meanwhile the $O_2$ ions

| Parameters ICP | "Fast" Recipe | "Slow" Recipe |
|---|---|---|
| $O_2$ flow rate (sccm) | 60 | 22.5 |
| Ar flow rate (sccm) | 40 | 7.5 |
| $C_4F_8$ flow rate (sccm) | 3 | - |
| Coil Power (W) | 1800 | 600 |
| Platen Power (W) | 100 | 40 |
| Temperature (°C) | 25 | 25 |
| Etch rate (nm/min) | 78 | 13 |

Table 3.3: STS ICP recipes parameters optimized by BLIN

etch the diamond.

The planarization method proposed is divided in two parts : the first one represents the spin-coat of flowable silica to completely cover the diamond film surface. The second one involves the ICP dry etching at the same etch rate the diamond and the annealed silica layer.

Once the HSQ layer is spin-coated on the diamond film surface, the second part of the planarization process can be realized. Dry etching ICP method is used to transfer the planarized surface from the annealed HSQ to polycrystalline diamond film (Fig. 3.8). To realize that, two recipes were available in the group with the parameters listed in Table 3.3. The parameters were optimized for STS ICP machine available in the cleanroom MINERVE, with the aim to have the same etching rate for both the HSQ layer and the diamond film. The "fast" recipe has been used for the most part of the planarization transfer procedure by ICP etching, due to its rapid etch rate compared to the other recipe. The "slow" recipe was used to finish the planarizing process, C. Blin measuring better roughness RMS values as compared to the "fast" recipe (0.9 nm and 2.4 nm respectively).

The samples were processed using these recipes already available until July 2017, when the STS ICP machine broke definitively after several months of intermittent functioning. I was forced to create recipes that fulfill the same behavior on another machine namely the SPTS ICP. The simple transfer of all the parameters of the process did not produce the same result. I started to develop a new planarization recipe using the "slow" recipe parameters because it was the simplest recipe from the two available on the STS ICP. In the following paragraphs I will present the strategy that leads to the final planarization recipe on SPTS ICP machine.

The optimization of the process consisted into the introduction of two different samples, one with annealed HSQ and the other with a already flattened diamond film surface, sample processed previously with STS ICP system. After the etching process test on SPTS ICP, the etching rate of each sample was measured by optical ellipsometry. The combination of these two gases ($O_2$ and Ar) at different ratios, along with the change in the coil power did not

| Parameters ICP | Values Recipe SPTS |
|---|---|
| $O_2$ flow rate (sccm) | 90 |
| Ar flow rate (sccm) | 30 |
| $C_4F_8$ flow rate (sccm) | 4 |
| Coil Power (W) | 2500 |
| Platen Power (W) | 80 |
| Temperature (°C) | 25 |
| Etch rate (nm/min) | 80 |

Table 3.4: Parameters SPTS ICP optimized for diamond planarization

offer a reproducible etching rate for the HSQ sample. Using a longer and powerful cleaning of the chamber before the process stabilized the etching rate of HSQ, but the etching value was to small for HSQ as compared to diamond using these conditions. So I decided to add $C_4F_8$ gas at a 4 sccm (standard cubic centimeters per minute) flow rate (the minimum flow rate possible with this machine under these parameters) to accelerate the etch rate of the HSQ. The idea is similar to the one used previously in the “fast” recipe. By multiplying by 4 the gas-flow of the $O_2$ and Ar gases while keeping the same ratio and doubling the coil power, the etching rate for both HSQ and diamond was around 42 nm/min. The etching rate was doubled when the coil and platen powers were doubled, keeping the ratio 1:1 for both samples. The final parameters for the planarization recipe on the SPTS ICP machine are listed in Table 3.4. The developed recipe has similar etch rate as the “fast” recipe from STS ICP machine. The developed recipe on SPTS ICP was used to smooth the actual diamond samples that will be further processed.

In the following paragraphs I will present the example of 2-inch sample planarization with 5 µm polycrystalline diamond film on silicon wafer (surface after the initial cleaning, Fig. 3.11 a). After HSQ spin-coating and wafer annealing, the sample was glued with Fomblin oil on a 4-inch carrier wafer, the standard wafer size for the ICP machine. Two layers of FOX 15 were spin-coated to achieve a thickness of about 1.2 µm, that is sufficient for homogeneously covering the diamond film. The etching process was performed for a total thickness of 1.66 µm, meaning etching 460 nm of diamond. The sample was immersed in BHF acid to remove the remaining HSQ to analyze the surface of the diamond film at an intermediate point during the planarization process (Fig. 3.11 b). It can be observed that the planarization process is not finished and no new surface defects are introduced using this developed recipe. The sample was covered by 440 nm FOX 15 resist using the same protocol as mentioned above and the etching process time was calculated to achieve a planar diamond film (Fig. 3.11 c). From the SEM image it can be observed that the film roughness decreased drastically, statement that is confirmed by AFM measurements.

Surface roughness RMS was measured by Atomic Force Microscopy (AFM) for 10 × 10 $\mu m^2$.

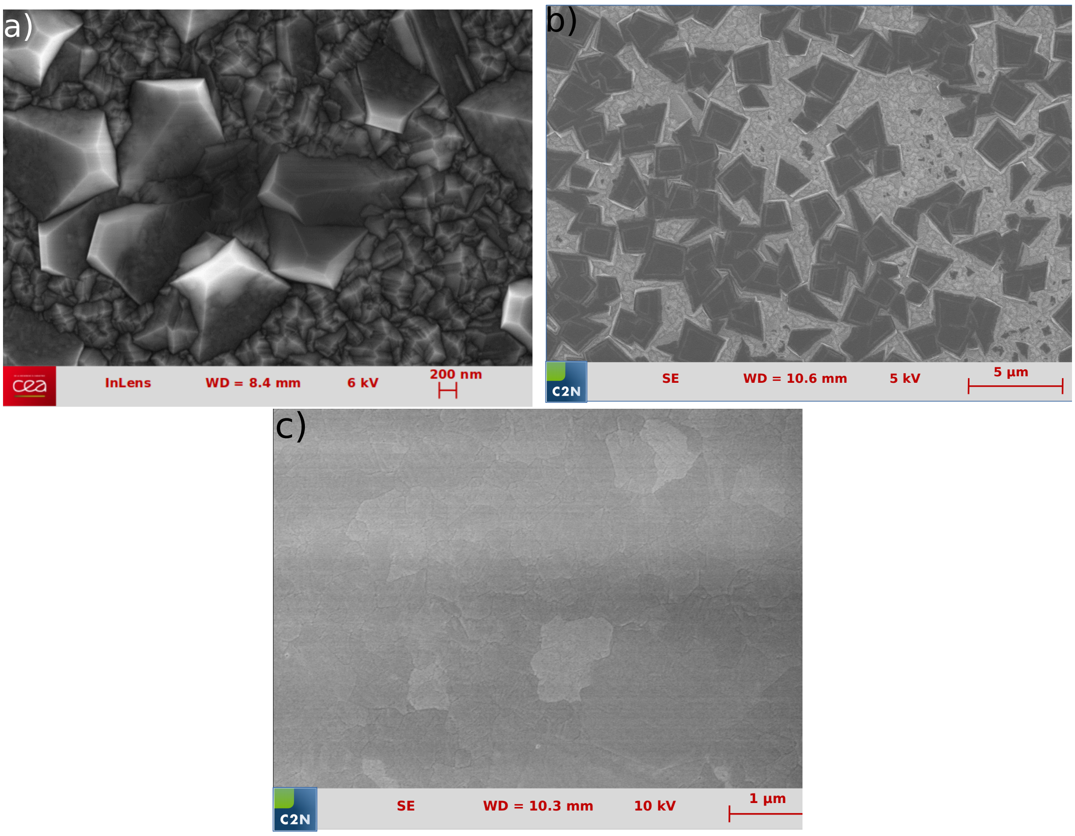

Figure 3.11: Planarization process for 5 µm polycrystalline diamond sample a) after growth ; b) during the planarization process observation with HSQ resist removed to investigate the diamond surface; c) planarized diamond film at the end of the etching process

In Fig. 3.12 a) is depicted the AFM measurement of the previous planarized diamond film from Fig. 3.11. We found holes in the diamond and we believe that they appeared at the grains interfaces during the etching process due to different chemical composition or material hardness difference, as compared to bulk diamond. In the case of the brighter spots, I believe that the AFM tip was contaminated. A 2.6 nm roughness RMS value was found for $10 \times 10\ \mu m^2$.

For 400 nm thick sample on silicon substrate, a roughness RMS value of 724 pm was found (Fig. 3.12 c) and for 400 nm diamond film on quartz wafer a value of 449 pm roughness RMS value was measured (Fig. 3.12 d) for $10 \times 10\ \mu m^2$ in both cases. The results are comparable with the previous work done by C. Blin, showing that the developed recipe gives the same quantitative results. The improvement is that there is no need of two different recipes to planarize the diamond film. If the planarization protocol was performed again for the thick diamond film, lower roughness RMS values could be achieved.

In conclusion, I presented here the details of the planarization process needed for the fabrication of the 2D PhC structures and the strategies used to decrease the polycrystalline diamond film rugosity. Deposition of two layers of HSQ resist without cracks with a maxi-

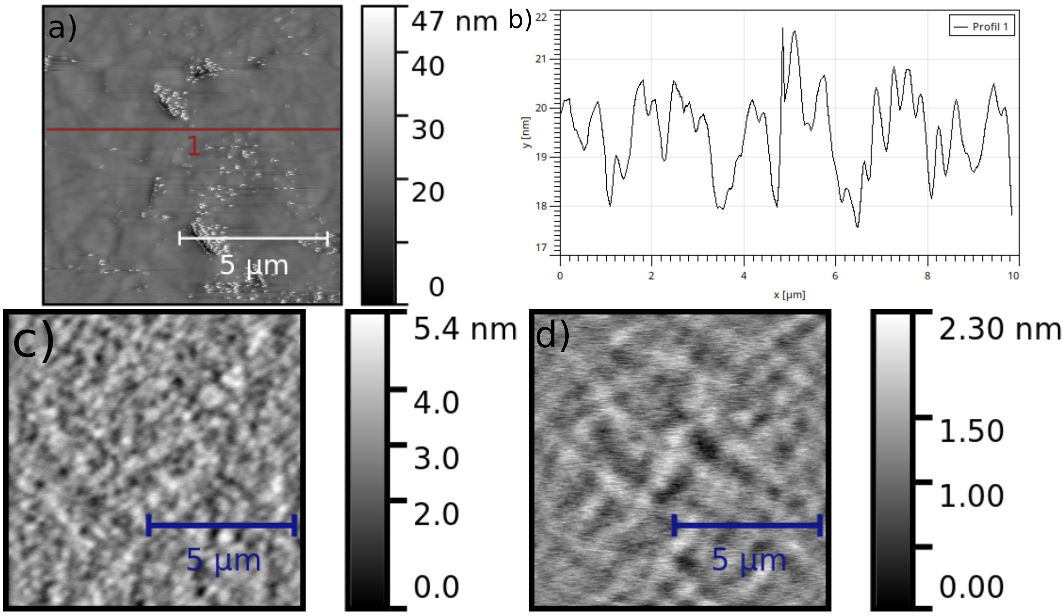

Figure 3.12: AFM measurements on different polycrystalline diamond film samples after the planarization processes (dry etch performed on SPTS ICP system) a) surface topography for 5 µm diamond film on silicon (RMS = 2.66 nm); b) Roughness RMS profile measured on 10 × 10 $\mu m^2$ diamond (a); c) surface topography for 400 nm diamond on silicon wafer (RMS = 724 pm); d) surface topography for 400 nm diamond on quartz wafer (RMS = 449 pm);

mum thickness of 1.5 µm was optimized with a new annealing protocol. Due to the break down of the STS ICP machine where the etching recipes were developed by the group, the development of a recipe on SPTS ICP machine was realized with similar RMS of the final polycrystalline diamond film as the ones found previously on the other ICP system.

## 3.4 Integration of diamond film for 2D photonic crystals

### 3.4.1 Purpose

The presented processes were developed to planarize the surface of various thicknesses of polycrystalline diamond films. This flat surface allows patterning of PhC with good accuracy. According to simulations, the typical thickness needed are between 200 and 400 nm and depends on the targeted wavelength. For thin films of this thickness, the fabrication of the 2D PhC can be realized. In the case of a few microns diamond films, I suppose that the use of bigger grains available on the top part of the film will induce less optical losses in the material, which will lead to better performances of the 2D PhC. Indeed, the growth of thicker diamond film will increase the grain sizes and also decrease the grain boundary

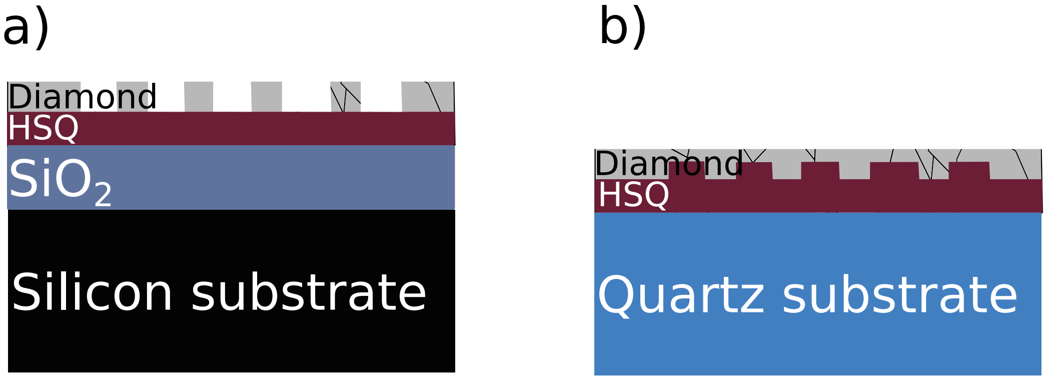

Figure 3.13: Two different strategies involved for the transfer of the diamond film onto a new substrate: a) with PhC on the surface for the final device; b) PhC encapsulated into the device with smooth diamond surface

density, leaving a more homogeneous structure. M. Lions ([99]) studied the influence of the diamond film thickness regarding the grain sizes and the grain boundary density. He proved that the density of the grain boundaries is inversely proportional to the grain size. For a 100-nm film, there is 4.2% of the entire diamond film composed by grain boundaries, assuming that the thickness of a grain boundary is 1 nm. In the case of 4 µm thick film, the ratio decreased to 1%([99]). Knowing that on the top part are the biggest grains and that for the proposed designs only 370-400 nm film are needed, the use of the top part of the film appears as a promising strategy for improving the diamond optical properties.

The aim of the PhD thesis is to realize a diamond optical biosensor working in the visible wavelength range. For that, multiple strategies are possible to fabricate the PhC: either on surface of the diamond film (Fig. 3.13 a), either integrated under a thin diamond film, as shown in Fig. 3.13 b). The first one consists in diamond film bonding to a new substrate, followed by etching of the initial silicon substrate, thinning of the diamond film at the desired thickness and then patterning the surface with Electron Beam Lithography (EBL) method, as shown in Fig. 3.14. The second strategy consists in patterning the surface with a PhC, then bonding to another wafer, followed by etching of the initial substrate and thinning at the desired thickness. The advantage of using the second strategy for bio-detection consists on the smooth and uniform diamond surface for functionalization and detection. In both proposed strategies, the development and optimization of the technological processes involved in the transfer are required.

The previously planarized 2-inch polycrystalline diamond samples were cleaved to obtain quarter of 2-inch wafers. C. Blin developed a protocol that lead to a homogeneous bonding on quarter of 2-inch wafers ([63]). The inconvenient of the process was that it uses benzocyclobutene (BCB) as bonding layer. The thermal conductivity of BCB ($0.29 \mathrm{W.m^{-1}.K^{-1}}$) is 4.5 smaller than the silica ($1.38 \mathrm{W.m^{-1}.K^{-1}}$). This insulating property of BCB lead to

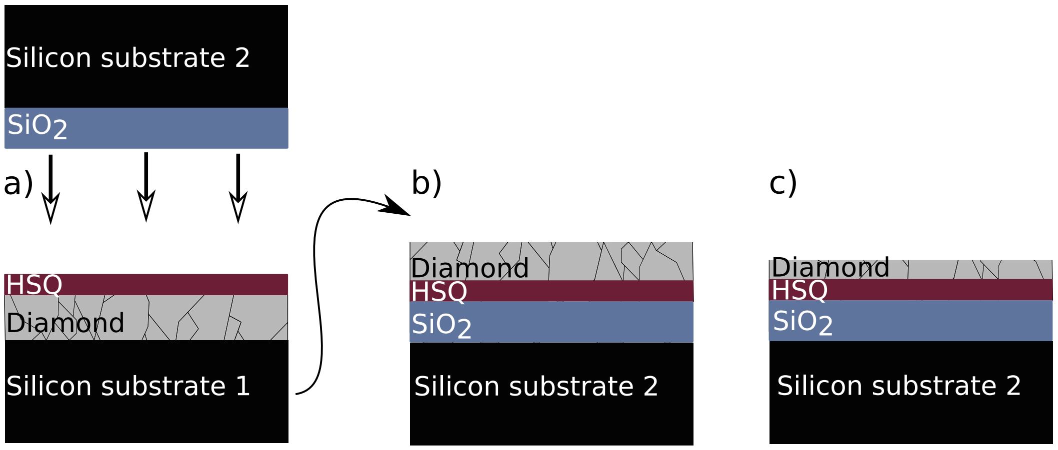

Figure 3.14: Transfer procedure of quarter of two-inch thick polycrystalline diamond sample to new silicon substrate. a) Bonding to Si wafer by applying pressure and rising the temperature; b) Etching the initial silicon substrate; c) diamond film thinning to the desired thickness.

heat dissipation problems on the diamond sample during the etching process. Also, BCB is not completely transparent in the visible wavelengths and has a refractive index different of quartz that may complicate the optical characterization when the PhC is probed with light from the substrate side. This method is based on the use of PECVD system, which was often out of order. As consequence, we changed the bonding layer with HSQ, taking advantage on the knowledge of spin-coating of uniform layers with this product.

HSQ, in the contrary, when baked, is equivalent to porous oxide. HSQ is an ideal candidate, having double role as bonding layer and optical support layer, establishing the Diamond-on-Insulator (DOI) configuration. During my thesis, I optimized the transfer of polycrystalline diamond films onto silicon and quartz wafers using HSQ.

### 3.4.2 Diamond bonding on silicon wafer

In the next paragraphs I will present in detail the first strategy shown in Fig. 3.14 with the main steps for diamond film transfer to silicon substrate.

During my thesis, I tried different strategies to transfer the diamond film onto silicon substrate, as follows :

- the planarized diamond sample with a HSQ layer on top is bonded to a silicon wafer with 2.5 µm of thermal silica on the surface, shown in Fig. 3.14;

- the deposition of silica by PECVD directly on diamond film, followed by spin-coating of HSQ resist on the surface and bonding with a silicon wafer;

- direct bonding of diamond sample with HSQ layer on the surface to a silicon wafer.

The presented configurations were tested to determine which one gives the best results. Almost the same bonding protocol was used in all the cases, as I will detail in further

| Parameters | Values |
|---|---|
| Temperature $1^{st}$ plateau °C | 200 |
| Temperature $2^{nd}$ plateau °C | 400 |
| Applied force N | 2000 |
| Pressure mbar | $10^{-4}$ |
| Plateau time min | 60 |

Table 3.5: Parameters used to bond silicon wafers

paragraphs.

After the bonding process, the initial silicon substrate is removed using a dry etching BOSCH process, followed by diamond film thinning at the desired thickness (Fig. 3.14 b) and c).

A preliminary experiment was realized to optimize the bonding parameters using HSQ resist. The test was done using two quarters of 2-inch silicon wafers. Both samples were cleaned in isopropanol and acetone solution, then immersed in isopropanol solution for 5 minutes with ultrasounds. Prior to bonding, the samples were dehydrated on a hot plate at 150°C for 5 minutes. A layer of 200 nm of XR 1541 6% was spin-coated to one of the two samples. Thicker layers can be spin-coated if the surface roughness increases by spin-coating of different HSQ layer i.e. FOX 15 (750 nm). In the articles ([100, 101]) the authors succeeded to bond 2 silicon substrates, using a hot plate at 150°C for 1 minute and 200°C for 1 minute to anneal the HSQ layer. I observed during different tests that 1 minute at 100°C and another one at 200°C were enough to remove the solvent, but to remain soft and to do not crack the HSQ film after the annealing step. The second quarter of 2-inch silicon sample was placed on top of the first one and introduced immediately into the bonding machine. The principle of this method is to apply simultaneously a high force (2000N) and a high temperature (400°C). Combining the two parameters lead to crushing of the eventual asperities and to a good bonding between the 2 layers. The bonding machine used in our studies is an EVG501, with the parameters of the bonding process listed in the Table 3.5. The temperature was raised 5°C/s until 200°C, temperature reached when XR 1541 was baked and a pre-bond step is reached. 2000N force is applied and the temperature is raised up until 400°C, then maintained for 1 hour. This heating combined with the applied force, hardens the XR 1541 and forms thermally stable bonds between the two surfaces ([101]). The applied force is maintained until the temperature drops under 150°C.

The bonded samples were characterized by near infrared camera. Silicon is transparent in this wavelength range and it is possible to see the quality of the bonding. Fig. 3.15 presents an image of the two silicon samples bonded with XR 1541 6%. The white spots represent non-bonded zones, meanwhile black spots are found on the back-side of the samples. These black spots are rests of the carbon layer used during the bonding process that remained

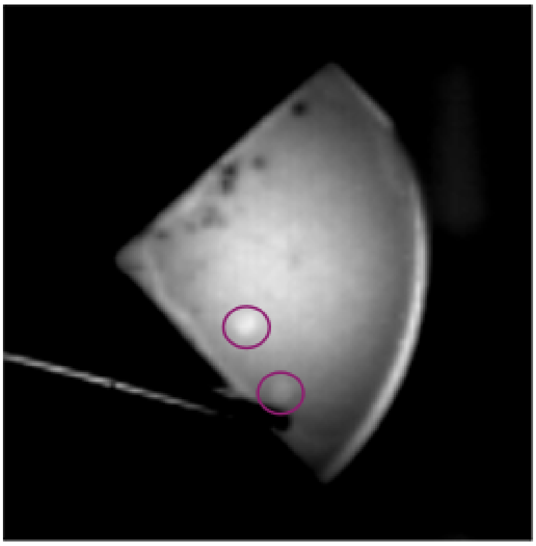

Figure 3.15: Infrared image of 2 quarter of silicon wafers bonded with XR 1541 6%. Red circles indicates the bonding defects

stuck to the sample. They can be removed using a cotton swab with BHF acid. Using the bonding recipe listed in Table 3.5, I succeeded to do a homogeneous bonding between two silicon wafers. Once the recipe validated, bonding of diamond samples was performed.

Prior to the bonding step, the polycrystalline diamond sample and the silicon sample were thoroughly cleaned in order to not have any contaminants before the deposition of HSQ or PECVD layers, any particles trapped at the interface can lead to defects in the further bonding process.

The first two presented strategies for diamond film transfer to another substrate uses silica layer (thermal or PECVD). This layer is frequently used in optics as a spacer between the material and substrate and will lead at an ease of fabrication of suspended membranes by under-etching using HF acid. In the case where $Si0_2$ layer is deposited by PECVD on the smooth diamond film, C. Blin optimized the process to have a good adhesion with diamond. The deposition of $SiO_2$ needs to be done by two recipes: the first layer $HFSiO_2$ (higher frequency $SiO_2$ - low deposition speed - 2 µm/h) with constraint of -275 MPa was deposited with 500 nm thickness and a second type, $LFSiO_2$ (low frequency $SiO_2$- higher deposition speed - 4 µm/h) with higher constraint coefficient of -370 MPa was deposited with a thickness of 1.5 µm ([55]).

In the presented bonding example of silicon wafers, XR 1541 6% layer was spin-coated to act as bonding layer with a thickness of 200 nm. In the case of diamond samples, there is a film inhomogeneity over the entire quarter of 2-inch diamond wafer, as explained in 3.2.2. To compensate this inhomogeneity, a thicker FOX 15 layer was spin-coated and annealed for 5 min at 150°C. The bonding parameters were kept the same, as presented in Table 3.5.

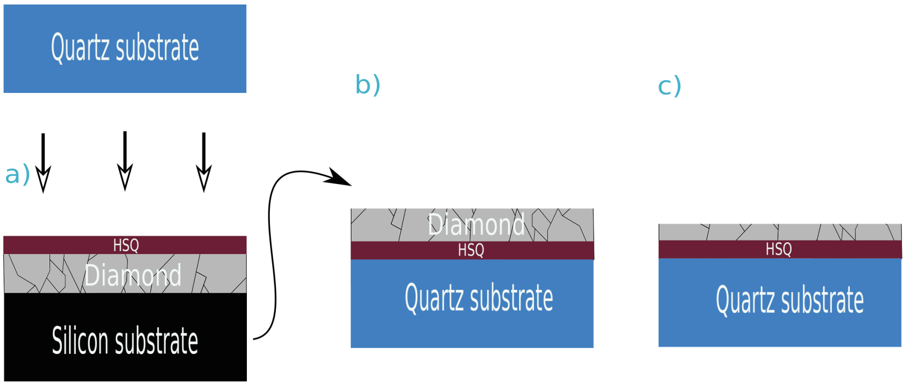

Figure 3.16: Transfer procedure of quarter of two-inch thick polycrystalline diamond sample to new squartz substrate. a) Bonding to $SiO_2$ wafer by applying pressure and rising the temperature; b) Etching the initial silicon substrate; c) diamond film thinning to the desired thickness.

### 3.4.3 Diamond bonding on quartz wafer

Diamond film transfer to quartz wafer (Fig. 3.16) represents the second recipe optimized during my thesis due to the quartz transparency in visible wavelengths range. As in the case of diamond film on silicon substrate, we want to use the top 400 nm of the diamond film, where the biggest grains of an initial diamond film of few microns thickness are located. The purpose for developing this method is to optically probe the diamond guided modes from the back side of the sample. This transfer on quartz wafer offers the possibility for the top part of the sample, where diamond is located, to be used for detection purpose only, while the light is injected from the backside. When the biodetection measurements will be performed, the top surface of the device (where the diamond is located) will be only for detection purposes. Both strategies presented in 3.4.1 were tested in fabrication.

Cleaning and spin-coating of HSQ layer was done using the same parameters as explained in 3.4.2. Bonding tests of quartz to diamond film on silicon wafer were performed using parameters of Table 3.5. Most of the times the quartz wafer broke during the bonding process. I suppose that this result was influenced by a series of factors. A different thermal expansion and material hardness between quartz and silicon could be an explanation. A second reason could have been a contaminant particle stuck at the interface of quartz / silicon big enough to create a defect in the bonding, which led to wafer cracking when the force is applied. Another cause could be that the diamond grown on silicon induced a curvature on the wafer or diamond film thickness inhomogeneity. All these explanations conduct to the idea of increasing the HSQ bonding layer thickness or to decrease the applied force during the process. FOX 15 was deposited at 740 nm thickness, but the quartz wafer cracked. A decrease in the applied force at 500 N was the optimum force to have a homogeneous bonding all over the quarter of 2-inch wafer. In Fig. 3.17 is presented an example of diamond sample

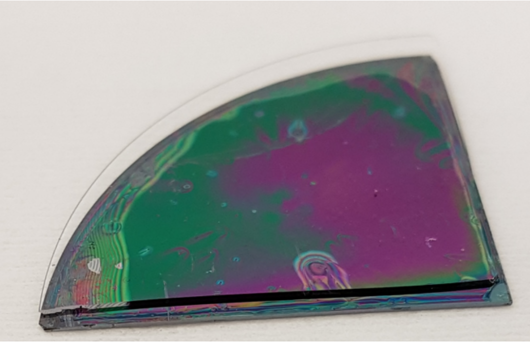

Figure 3.17: Image of quartz wafer bonded to diamond on silicon wafer

bonded to quartz wafer. It can be observed that the bonding is achieved in the most part of the sample, except the left corner of the sample. In the bottom middle part of the sample there is a defect in diamond film growth from a dust particle that was deposited on the surface of diamond film, which lead to this comet like shape when HSQ was deposited. The color change on the different zones of the sample indicates the different diamond thickness.

The obtained result of diamond bonding with quartz was satisfactory, with the possibility to use most of the sample surface to fabricate photonic crystals. The next process involved was the etching of the initial silicon substrate of the bonded wafers.

### 3.4.4 Silicon dry etch method

The next step of the process was to remove the initial silicon substrate. Silicon etching can be done by two etching methods: liquid phase or gas phase. In the liquid case, a series of methods are known in the literature ([102, 103]). In my case, the immersion of the sample in HF acid solution or KOH solution would cause silica etching (HSQ, thermal or PECVD silica) and consequently diamond film would delaminates from quartz / silicon substrate. Therefore, the use of dry etching using ICP method was preferred. Silicon is etched uniformly on the whole substrate and the other side of the sample is protected by the carrier wafer. Prior to dry etching, the substrate needs to be cleaned rigorously to remove unwanted contaminants that may block the etching, phenomenon known as micro-masking. These defects will be transferred to the diamond film, unwanted in our case to preserve the surface flatness. Contaminants can be HSQ solution leaked onto the back face when spin-coated. To remove them, I did a thorough cleaning with cotton swab dipped in HF, then acetone, isopropanol and water rinsing. Furthermore, a $O_2$ plasma was performed prior to silicon etching.

For the further step is needed an isotropic silicon dry etching process. On the SPTS ICP there was already available one recipe that matched our demands, namely the BOSCH method, which is frequently used in microelectronics for silicon dry etching. This process

| Parameters | Values |
|---|---|
| Pressure (mTorr) | 30 |
| $C_4F_8$ flow rate (sccm) | 400 |
| S$F_6$ flow rate (sccm) | 330 |
| Etch phase time (s) | 1.2 |
| Deposition phase time (s) | 1.5 |
| Etch/deposition phase Coil/ Platen (W) | 2500/10 |
| Temperature °C | 0 |
| Number of cycles | 270 |

Table 3.6: Dry etching BOSCH process parameters for 300 µm thick silicon substrate to remove

is composed of 2 alternating phases: isotropic etching using $SF_6$ gas, where fluorinated radicals react with silicon and form $SiF_4$ species; the second phase is the deposition phase or passivation with $C_4F_8$, where a layer of $C_xF_y$ polymer is deposited on the surface. This passivation step allows to keep the surface flatness for the first phase of BOSCH process. Alternating many times this cycle of etching / deposition, a deep anisotropic etch can be produced. The parameters used for removing the initial silicon substrate are presented in Table 3.6.

In the Fig. 3.18 a) is shown a $20 \times 20\,\mathrm{mm}^2$ diamond film sample bonded to silicon wafer and in Fig. 3.18 b) is depicted a 3 µm thick diamond film reported on a quarter of 2-inch quartz wafer, after the removing step of the initial silicon substrate by BOSCH process in both cases. It can be observed in Fig. 3.18 a) the homogeneity of the bonding process, with a small defect in the lower part of the diamond sample, where the diamond film was destroyed. The color change indicates the diamond film thickness change or silica layer compression. Because of this thickness difference from the border to the center of the sample, it is hard to determine the actual film thickness at any point of the sample. In Fig. 3.18 b) a non-bonded zone is found in the left corner of the sample. The black spots at the edges of the sample represents the non-etched silicon substrate after BOSCH process. The removal of these silicon remains can be done by exposing the sample to $XeF_2$ gas for several tens of seconds. The $XeF_2$ dry etching process is also isotropic. The difference to the BOSCH process is the slow etching speed of silicon, method that was not feasible for removing the entire ~ 300 µm silicon substrate. Due to the thickness change over the entire sample (a few tens of nanometers), I developed a strategy to diminish this inconvenient in order to realize PhC able to detect at the desired wavelengths and will be detailed in the section 3.5.

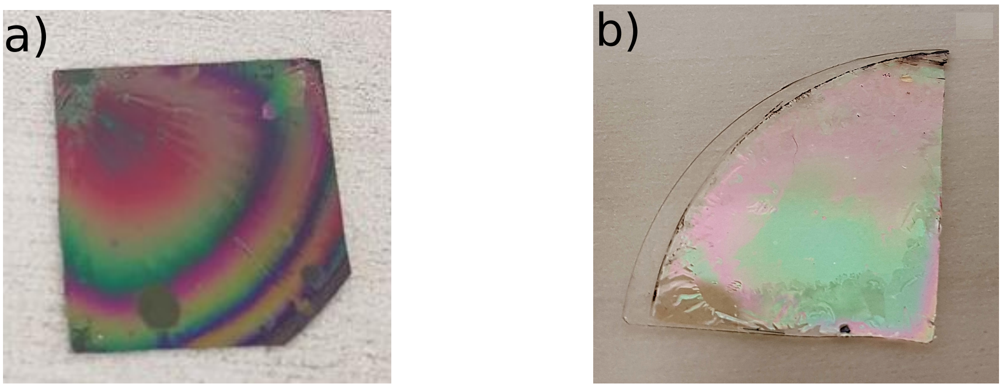

Figure 3.18: Polycrystalline diamond transfer to a) silicon substrate with $SiO_2$ PECVD and HSQ resist as intermediate layers; b) quartz substrate using HSQ as intermediate layer

### 3.4.5 Diamond thinning

The final step of the transfer process was the diamond thinning at desired thickness. Prior to the etching process, a new cleaning step was done to eliminate all possible residues that could be transferred on the surface during the diamond etching process. In consequence, the sample was immersed in piranha solution for 5 minutes to eliminate all possible organic residues and then in HF diluted 1:2 in DI water for 30 seconds to remove any eventual silica residues (it is true that the silica and HSQ layers will be etched, but the reaction not occur for a long period of time, resulting in a few micrometers under-etch).

With this sample configuration, the diamond morphology is not the same as compared to the previous cases from the 3.3.4.2. As explained, the first part to be etch is the nucleation layer, where nano-diamonds seeds are. Knowing that the density of grains is very high and the grain boundaries did not have typical characteristics of bulk diamond, the etching speed may be different. Adding that the reported film is now find in the configuration Diamond-on-Insulator (HSQ or silica intermediate layers to silicon wafer or HSQ on quartz wafer), the behavior of the plasma etching may not be the same as described in previous recipes. The idea to decrease the temperature of the carrier substrate was proposed previously in the C2N team, where the thermal effect due to the DOI configuration was minimized for a similar application ([63]).

First test for diamond thinning was performed on STS ICP machine, a recipe using only $O_2$ as etching gas, which is known to be the most effective gas that etches diamond, at low pressure and high platen acceleration to increase the etching rate of the diamond (Table 3.7)([104]). Apparition of unwanted holes on the surface, as shown in Fig. 3.19 a), destroys the smooth surface after the process. It can be observed that the majority of the

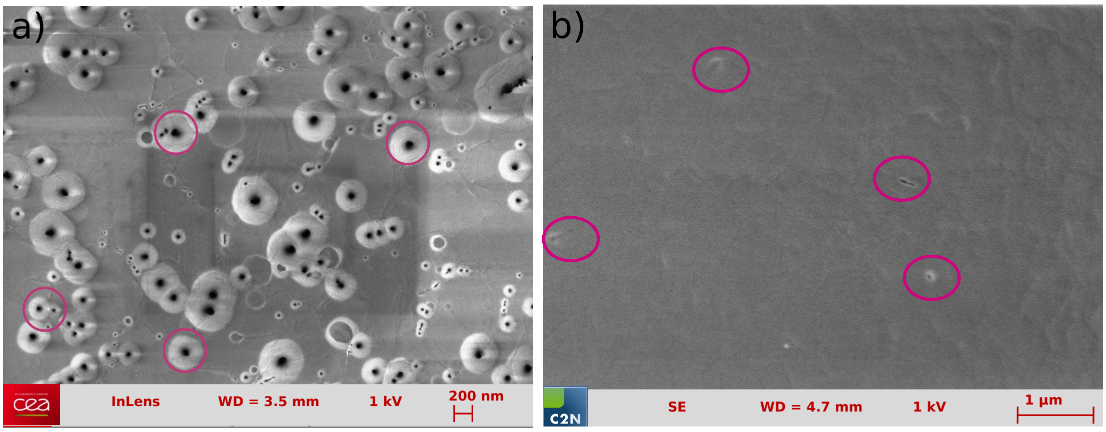

Figure 3.19: SEM images for a) fast Thinning Recipe STS ICP; b) Modified fast Recipe STS

holes are placed at the grain boundaries, where the material is easier to be etched (red circles from Fig. 3.19 a). A similar behavior was observed in the case of monocrystalline diamond etch by ICP method, where etch pits appear at the location of surface defects. It was a surprise that this phenomenon did not appeared for polycrystalline diamond samples processed before my arrival in our group.

The second test for thinning recipe was also optimized on STS ICP, starting from the "fast" recipe. When using the same recipe parameters listed in Table 3.4, holes appears on the diamond's surface at grain boundaries, as in the case of first thinning recipe developed. In the article ([98]), a decrease in the $O_2$ gas flow rate and an increase of Ar gas flow rate at a ratio close to 1:1 leads to a more homogeneous etching process. The best configuration for a homogeneous etching of the diamond film was found when $O_2$ gas flow rate was reduced and the carrier wafer cooled down to 10°C, parameters listed in 3.7 (Fig. 3.19 b). It can be observed that for $3.5 \times 2.5$ µm$^2$, only 4 defects (circled in red color) are found on the surface. This result was satisfactory to further process the samples. After the STS ICP broke down, the recipe transfer on the SPTS ICP was necessary.

For SPTS ICP machine, I tried to optimize the recipe keeping the same strategy as presented in STS ICP recipe optimization, but for all the performed tests, the presence of holes in the surface was found. Teii *et al* ([105]) offered an alternative to $O_2$ based recipes for diamond etching. The authors claimed that similar results can be attended using $SF_6$ gas. I started from the thinning recipe where I modified the gases used by adding $SF_6$ and Ar instead of $O_2$. The injected fluorinated gas is responsible to the diamond etching and Ar is known to flatten the diamond surface. The best conditions are listed in Table 3.7, recipe with 77 nm/min etch rate, value measured during the recipe optimization for diamond test samples on silicon wafer. When the optimized recipe was applied to diamond film transferred to a new substrate with DOI configuration, etching rates up to 82 nm/min were calculated

| Parameters ICP | Rapid Thinning Recipe STS | Modified Rapid Planarization Recipe STS | Thinning Recipe SPTS |
|---|---|---|---|
| $O_2$ flow rate (sccm) | 99 | 40 | - |
| Ar flow rate (sccm) | - | 30 | 80 |
| $C_4F_8$ flow rate (sccm) | - | 3 | - |
| $SF_6$ flow rate (sccm) | - | - | 40 |
| Coil Power (W) | 1800 | 1800 | 2000 |
| Platen Power (W) | 140 | 100 | 100 |
| Temperature (°C) | 10 | 10 | 0 |
| Etch rate (nm/min) | 120 | 65 | 77 |

Table 3.7: Parameters for diamond thinning recipes

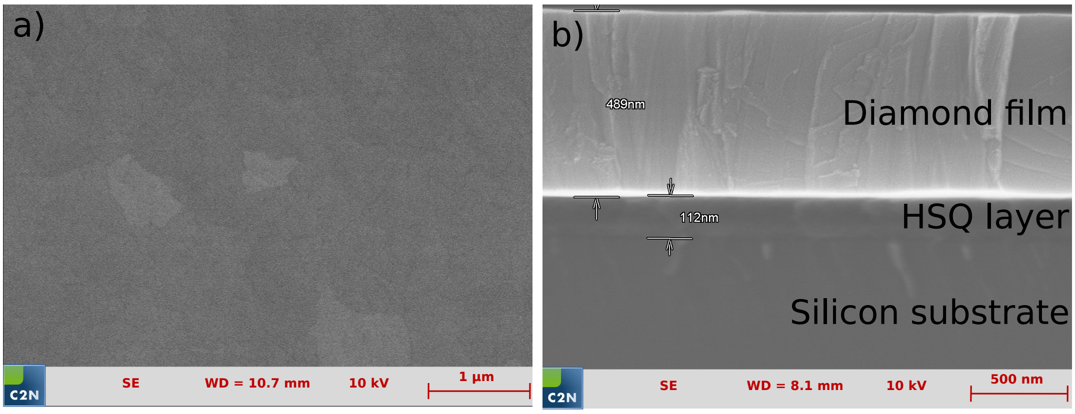

Figure 3.20: Diamond thinning using $SF_6$ recipe : a) top view; b) side view

when diamond etch process started (nucleation part of diamond film, formed by grain size of several tens of nanometers) and decreased to 71 nm/min when diamond grains became bigger. The surface was analyzed by SEM and it can be observed that the diamond was etched homogeneously, without any holes at the grain boundaries nor other defects on the surface (Fig. 3.20 a). The etching recipe was performed on transferred diamond films up to 5 µm, on quartz or silicon wafers and thinned down to 400 nm. In Fig. 3.20 b) is shown an example of a diamond film transferred onto silicon substrate with HSQ layer as bonding layer. It can be observed the uniform bonding process, as well as the homogeneous diamond film thinned down to 489 nm. The size of the grains observed by SEM is significantly bigger than in the case of a 400 nm thin film directly grown on silicon substrate. This may improve the optical quality of the diamond film, which, we think, will lead to better PhC performances.

I presented the successful transfer of a quarter of 2-inch thick diamond film to a new substrate, followed by etching of the initial silicon substrate and polycrystalline diamond film homogeneous thinning at the desired thickness. The bonding process was optimized

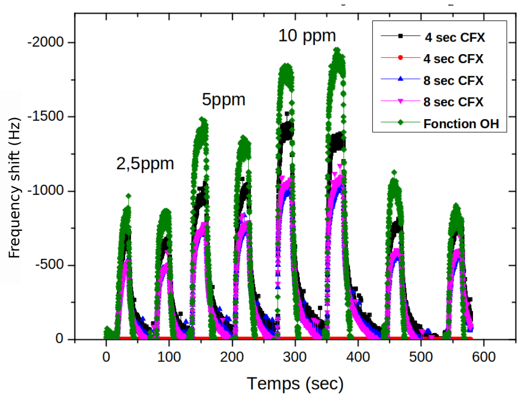

Figure 3.21: Frequency response of 5 different SAWs after different exposures under $NH_3$ gas

for a quarter of 2-inch samples using HSQ as bonding layer, using silicon or quartz wafer as bonding substrates. The removal of the initial silicon substrate was obtained by ICP dry etching. Successful diamond thinning of a few microns film at the desired thickness was optimized on two different ICP machines, with two completely different recipes.

Using all the processes discussed in this Chapter, the sample meets the conditions to fabricate high quality diamond photonic crystals.

### 3.4.6 Diamond surface influence for fluorine based plasma for SAW

During this PhD thesis, various new dry etching recipes were developed on SPTS ICP machine. Besides the etching recipes presented in this Chapter and although this is not the subject of this thesis, another recipe was developed for Surface Acoustic Wave (SAW) biosensor developed at LCD laboratory. The recipe was intended to change the diamond surface terminations by $CF_x$ groups, thus functionalizing the diamond surface. The recipe gases are Ar (30 sccm) and $C_4F_8$ (100 sccm), having a diamond etch rate of 15 nm / min. The SAW biosensors were processed for a few seconds (4 to 10 seconds) with the fluorinated based-plasma. The measurements of the SAW are represented in Fig. 3.21. The SAW devices were exposed to $NH_3$ gas. A binding event occurred at the surface of the biosensor will induce a frequency shift. The larger shift was measured when the diamond surface termination was changed to OH groups, method for which optimized protocols exists. In the case of SAW exposed to fluorinated based plasma, a frequency shift took place, sufficient to have a measurable signal. The diamond was etched up to 2 nm by the ICP recipe, apparently enough to change the surface terminations of the diamond film. These tests validate the possibility to functionalize the diamond surface with $CF_x$ groups. Optimization of the this recipe being necessary to give a more intense detection for SAW biosensors.

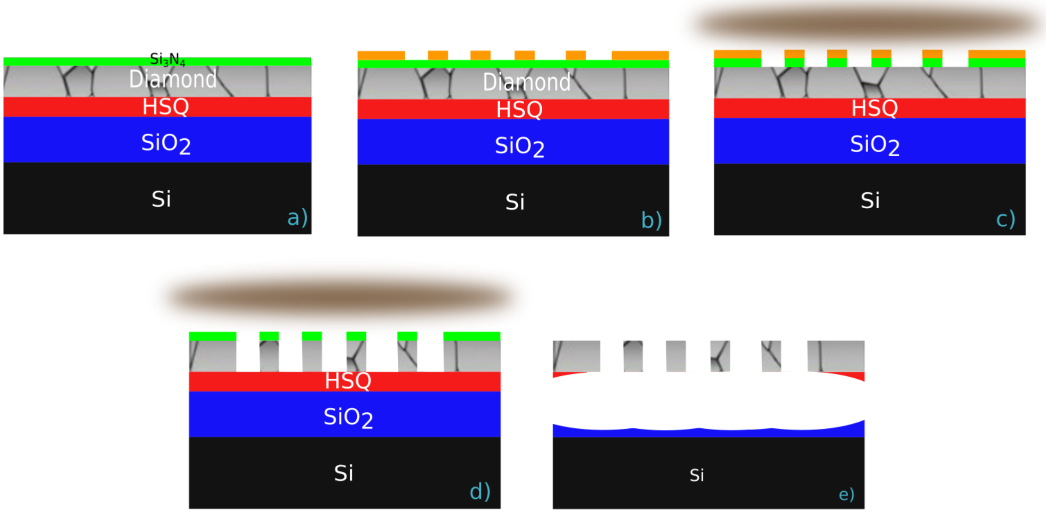

Figure 3.22: Diamond photonic crystal fabrication steps exemplified for the case mentioned in paragraph 1.4.2.1. a) Nitride mask deposition; b) Spin-coating of electronic beam resist, then electronic beam lithography exposure and solvent development; c) ICP recipe to etch the nitride mask; d) The pattern is transferred to the diamond film by ICP etching recipe; e) Under-etching of the HSQ and silica layers by HF acid.

## 3.5 Diamond 2D PhC fabrication

Once the diamond film is planarized and etched at the desired thickness, the sample is ready to be patterned with PhCs. Fabrication of PhCs consists in multiple steps, as shown for example in Fig. 3.22. Each phase of each process will be discussed in detail.

As presented in the section 3.4, multiple strategies were developed during my PhD thesis. In Fig. 3.22 is depicted a brief diagram for the example of polycrystalline diamond film transferred onto a thermal silica layer on silicon substrate, using HSQ as bonding layer, where the diamond film is thinned down to 370-400 nm.

A different strategy is to fabricate the PhC on thick diamond film (few microns, Fig. 3.13 b). The next technological process for this configuration is the bonding process with a quartz substrate, followed by initial silicon substrate removal and diamond film thinning. As final device, the PhC structures will be encapsulated onto the sample, leaving a smooth diamond surface for bio-detection.

PhC fabrication can be also realized on thin diamond films of 400 nm (diamond grown on silicon substrate for example), where the fabrication does require only the first planarization technological step without bonding.

The first step of PhC fabrication implies the deposition of a hard mask on the surface (Fig. 3.22 a), followed by spin-coating of an electronic lithography resist and surface patterning with photonic crystals using electronic beam lithography (EBL) technique. Afterwards, electronic resist development (Fig. 3.22 b), followed by hard mask (Fig. 3.22 c)

| Parameters | Values |
|---|---|
| $SiH_4/NH_3$ flow rate sccm | 3000/20 |
| Power W | 60 |
| Pressure mTorr | 550 |
| Temperature °C | 300 |

Table 3.8: Nitride mask deposition parameters using PECVD system

then diamond dry etch by ICP (Fig. 3.22 d) allows the transfer of the desired pattern into diamond film. The last step is to remove the remaining hard mask and under-etching the diamond by HF acid solution (Fig. 3.22 e). Intermediate or additional steps that are not depicted in Fig. 3.22 will be also discussed.

## 3.5.1 Sample preparation before electronic beam exposure

### 3.5.1.1 Nitride mask

Pattern transfer from the electronic beam resist onto diamond is realized by a dry etching method, adapted to etch diamond and hence carbon. Knowing that electronic resists are composed of carbon polymers, an ICP process for diamond etching will instantly destroy the resist film. For that, an intermediate layer needs to be deposited between diamond and resist. This intermediate layer needs to fill some requirements. The first one is to have a good adhesion on diamond. Secondly, the pattern transfer from the resist to the intermediate material must be realized with high fidelity by ICP etching (hole walls to be as straight as possible). Thirdly, ICP etching processes must be selective : rapid etch of the intermediate layer and slow etch of the resist for pattern transfer on the intermediate layer, and rapid etch of the diamond layer with a minimum etch of the intermediate layer for pattern transfer into diamond film. The etching processes will be discussed in detail in next section. These specific characteristics will conduct to an accurate transfer of the designed pattern into diamond film. Candidate materials are silica, silicon nitride or metallic layer. Based on the experiences done in our group prior to my arrival, I used silicon nitride deposited by PECVD technique ([63]). It is more resistant than silica when diamond etching process is performed and it can be deposited on thinner layers on diamond, increasing the theoretical resolution for pattern transfer. The recipe parameters for $Si_3N_4$ deposition are presented in Table 3.8.

#### 3.5.1.2 Electronic beam resist

The choice of the electronic beam resist is done considering the negative / positive type, the ultimate resolution possible and the hardness when processed by ICP technique. Among the available resists ( PMMA, HSQ or ZEP), for the ease of PhC patterning, a positive resist was chosen. ZEP 520A has better resistance when dry etching compared to PMMA, reason that counted in our choice.

The resist is diluted in anisole solution (methyl-benzene) with a ratio 1:1 for thinner film deposition, dilution that leads to better pattern accuracy. The mix is left for few minutes to settle in a beaker for avoiding air bubbles. The sample is placed on a hot plate at 180°C for 5 minutes to remove the eventual water accumulated on the surface caused by room humidity. When cooled down, the solution is spin-coated on the sample at 5000 rpm for 1 minute, then annealed for 2.5 minutes at 180°C for solvent evaporation and resist hardening. The final resist thickness obtained is 130 nm.

In the case of samples on quartz, an additional electronic resist is required. Quartz is an insulating material, as consequence the accelerated electrons will be deflected by accumulated charges, affecting the accuracy on pattern writing. To overcome that, a conductive resist is spin-coated on the surface, on top of ZEP resist. This conductive solution is Espacer 300Z. It is spin-coated at 4000 rpm for 1 minute, then annealed for 2 minutes at 95°C.

### 3.5.2 Electronic lithography

In Chapter 2, I described different designs that offers high theoretical sensitivity values for detection. Realizing these photonic crystal designs requires accuracy in fabrication at all levels. To fabricate PhCs in diamond with desired guided mode resonance in the visible wavelength range, holes need to be created in the diamond film, with diameter sizes of around 120 nm. Given the pattern sizes, we turned to the electronic beam lithography, a method to draw custom patterns with excellent accuracy. The cleanroom of C2N Orsay offers two EBL machines. The one that we used was Nanobeam 4, with theoretical resolution of 1 nm and spot size of 5 nm for 80 kV acceleration.

### 3.5.3 Pattern design

EBL systems uses a data format for pattern writing. Nanobeam 4, the available system in our laboratory, accepts masks in GDSII format. The masks are created using Python home-made code developed by X. Checoury, where all the pattern files are generated in this format. It provides pattern manipulation functions such as main-field or sub-field fracturing and dose settings. A process called fracturing is necessary before exposure and this fracturing translates the GDSII data into a machine-readable file named nanobeam job

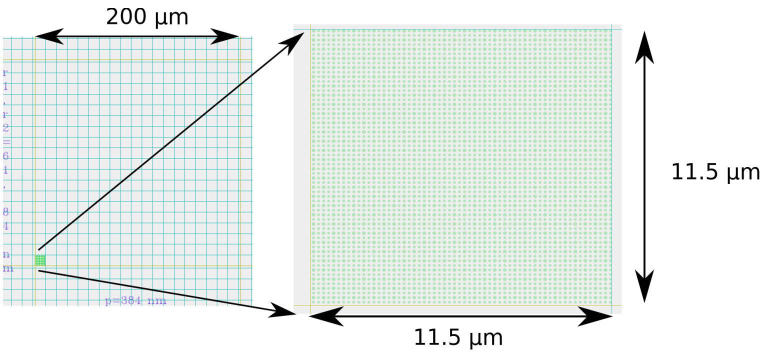

Figure 3.23: GDSII mask for fabrication of 200 × 200 µm$^2$ photonic crystal. The coded pattern is 30 × 30 fundamental lattice cell which delimits the size of a sub-field, depicted in blue color squares. Replication and shifting in x and y axis of the coded pattern will realize an homogeneous 200 × 200 µm$^2$ photonic crystal within a main-field, shown in yellow color square

file, which contains all the instructions that are needed to write the patterns. The values of different parameters such as injected doses, resist thickness etc, are modified slightly or not, starting from previous work done in our group ( [63, 106]).

### 3.5.4 Electronic beam exposure

The sample is exposed to high energy electron beam that will create the designed pattern on the electron beam resist. The maximum surface that can be patterned without mechanical move of the stage is 500 × 500 µm$^2$, called main-field. The main field is divided into sub-fields of 20 × 20 µm$^2$ surface area. The PhC size is 200 × 200 µm$^2$, meaning that the whole pattern is written in one main-field (yellow square in Fig. 3.23 ). The GDSII code pattern has the size of a sub-field (blue squares in Fig. 3.23), which represents typically 30 × 30 fundamental lattice cell. This pattern is replicated and shifted in such a way that, at the end, an homogeneous PhC of 200 × 200 µm$^2$ is realized without mechanical stage move.

In the case of a PhC of 200x200 µm$^2$ size, the writing time is around 1 minute. Depending on the density and the number of different patterns wanted on the quarter of 2-inch sample, the final time can be from several tens of minutes to a few hours.

### 3.5.5 Development after exposure

After exposure, the samples are immersed in ZED-N50 solvent solution for 1.5 min, then 20 s in isopropanol for stopping the reaction. ZEP 520 A is a positive resist, meaning that the exposed zones will be removed by the solvent, leaving behind the resist on the unexposed zones of the surface. The reaction time with the solvent needs to be precise in order to avoid over or under-development. The global pattern quality of the lithography is verified

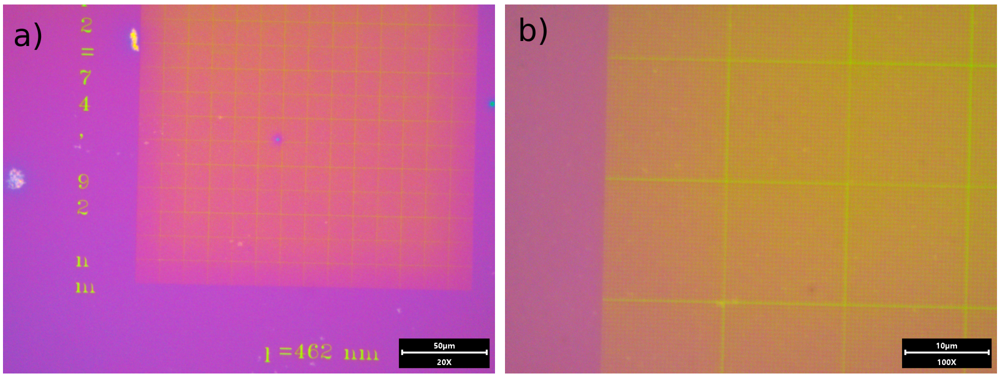

Figure 3.24: PhC obtained by EBL method after development in ZED-N50 solvent. Optical microscope images of the same PhC with different magnifications. Problems of EBL adjustements.

by optical microscope (Fig. 3.24 ). The pattern on the surface can be observed and the grid shape at the sub-field boundaries over the entire surface of the 200 × 200 µm$^2$ PhC, is a defect of the electronic lithography adjustments and should not appear when properly tuned.

### 3.5.6 Dry etching processes optimization for diamond 2D PhC fabrication

Once the patterns are realized on the samples, the next step is to transfer them from the resist to the diamond. For that, two recipes were developed for this purpose, the first one for etching the nitride mask and the second one for etching the diamond film. To accomplish high quality PhC structures, a crucial factor is the verticality of the sidewalls. From simulations, as explained on the previous Chapter, a guided mode (TE or TM) is designed to have a certain Q. If the desired Q is reached also in fabrication, the coupling of the incoming light with the structure will be maximal, increasing the intensity of the diamond optical resonant mode on the detector. In the following paragraphs, I will explain in detail the recipes optimization for nitride mask and diamond etching.

For samples fabricated before June 2017, the etching processes were realized by the STS ICP machine with recipes that were developed before my arrival. A good explanation and details of recipes can be found in Blin thesis ([63]). The break-down of the STS ICP machine forced me to transfer the recipe on the SPTS ICP machine. Using the same parameters as the ones of C. Blin recipes did not give the same results on the SPTS ICP machine. Each of the recipes needed to realize the PhC required an optimization onto the new machine. In the case of nitride mask etching recipe, the starting parameters were used from a silicon etching recipe developed by D. Néel ([107]) and were optimized to meet an accurate pattern transfer from the electronic beam resist to the nitride mask. For the diamond etch recipe,

| Parameters | Values |
|---|---|
| $SF_6/CF_4$ flow rate sccm | 160/160 |
| Coil Power W | 2000 |
| Platen Power W | 20 |
| Etching time s | 14 |

Table 3.9: Nitride mask etching parameters using SPTS ICP system

the parameters from the C Blin recipe were used as starting recipe and tuned to realize an anisotrope etch that implies an accurate pattern transfer from the nitride mask to diamond.

#### 3.5.6.1 Recipe for nitride mask etch

Depending on the thickness of diamond to be etched, the nitride mark requirements for an accurate pattern transfer are: to be as thin as possible to transfer the patterns from the resist to nitride film with good verticality of the sidewalls; the nitride etching recipe needs to have a selectivity higher than 1:1 for $Si_3N_4$ : ZEP; the nitride mask needs to resist for at least a 400 nm diamond etch process in order to keep the verticality of the sidewalls of the holes. Knowing all these requirements, a nitride mask was deposited by PECVD recipe (Table 3.8) with 105 nm thickness, that was measured by ellipsometry.

To obtain the optimal thickness for nitride mask, test samples were fabricated to optimize the nitride etch recipe on SPTS ICP system. Different tests were performed by changing one parameter at a time and SEM sample characterization to see the verticality of the sidewalls and the thickness of remaining ZEP resist after each process. Starting from decreasing platen power, the other parameters changed were gas flow ratio, coil / platen power and pressure. The final recipe parameters for the nitride mask etching recipe are listed in the Table 3.9, giving angles below 3° for sidewalls of 120 nm diameter holes and 5.41 nm/s nitride etch rate. It can be seen in Fig. 3.25 that the etching selectivity $Si_3N_4$: ZEP is 1:0.85. The sample was coated with 2 nm of gold to overcome the overcharging issue. The nitride etch result is comparable to the one developed by C. Blin on the STS ICP system.

#### 3.5.6.2 Recipe for diamond etch

Diamond etching for pattern transfer plays a critical role in PhC fabrication. The size of the holes needs to be the same as the simulated ones and can be adjusted in the GDSII mask in order to find the resonant modes at the desired frequency. Equally, a good verticality of the sidewalls conduct to better quality factors of PhC, approaching the theoretical expectations.

The hole sizes need to remain constant all along the depth of the holes which is around 400nm, with typical hole diameters around 120 nm for visible range detection, thus the ICP recipe requires anisotrope etching. Different groups, including our team, studied this

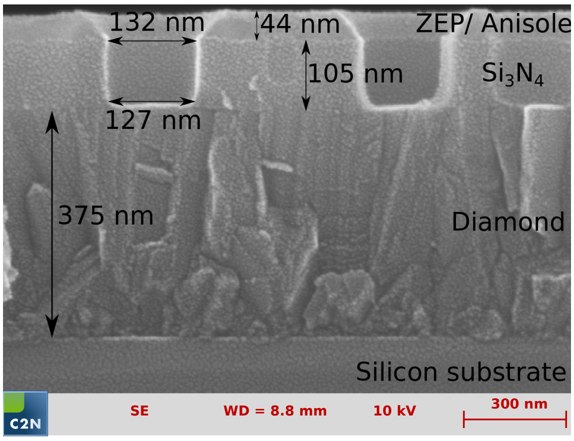

Figure 3.25: SEM image nitride mask etch. On the top part of the holes it can be seen the rest of the resist, meanwhile the nitride mask has sidewalls with a verticality better than 3°

technological challenging step and showed that ICP method, using $O_2$ gas mainly, is the best suited for uni-directional etching ([55, 108]).

Diamond etching recipe was optimized using test samples of 375 nm diamond grown on silicon substrate. The reason of choosing this type of sample was the easiest configuration for SEM image acquisition. In all other cases, the insulating substrate (quartz) or silicon oxide under the diamond make the image acquisition more complicated due to charges accumulated on the surface. A metalization process with gold of several nanometers solves this inconvenient, but the test sample cannot be further processed.

When I started developing the diamond etching recipe on SPTS ICP machine, the deposited nitride mask was 72 nm thick only, as in the case of C. Blin work. The same recipe parameters were used as in the STS ICP recipe developed by C. Blin (Table 3.10, with an increase of the $O_2$ gas flow rate from 99 sccm to 120 sccm) and the results lead to a too strong erosion of the nitride mask, increasing the hole radius transferred onto diamond (Fig. 3.26 a) and b). It can be stated that the smaller the hole diameter is, the better the mask tends to resist to the etching recipe. Different strategies were examined, changing one by one parameters as pressure, gas flow rate, carrier wafer temperature, coil power or platen power. The results indicate that the important parameters for this recipe are the pressure and the platen power. Knowing the hardness of diamond, the ions must be accelerated on the surface by applying high power to etch diamond and in the same time to be selective regarding the nitride mask. I observed that by increasing the process pressure, the diamond etching rate decreased and the nitride mask tends to be less destroyed after the process. Analyzing the SEM images after the process, I deduced that increasing the nitride mask thickness from 72 to 105 nm will be enough to resist etching 400 nm of diamond etching (Fig. 3.26 c).

In the Fig. 3.26 c) can be observed the successful transfer of the patterns on the diamond

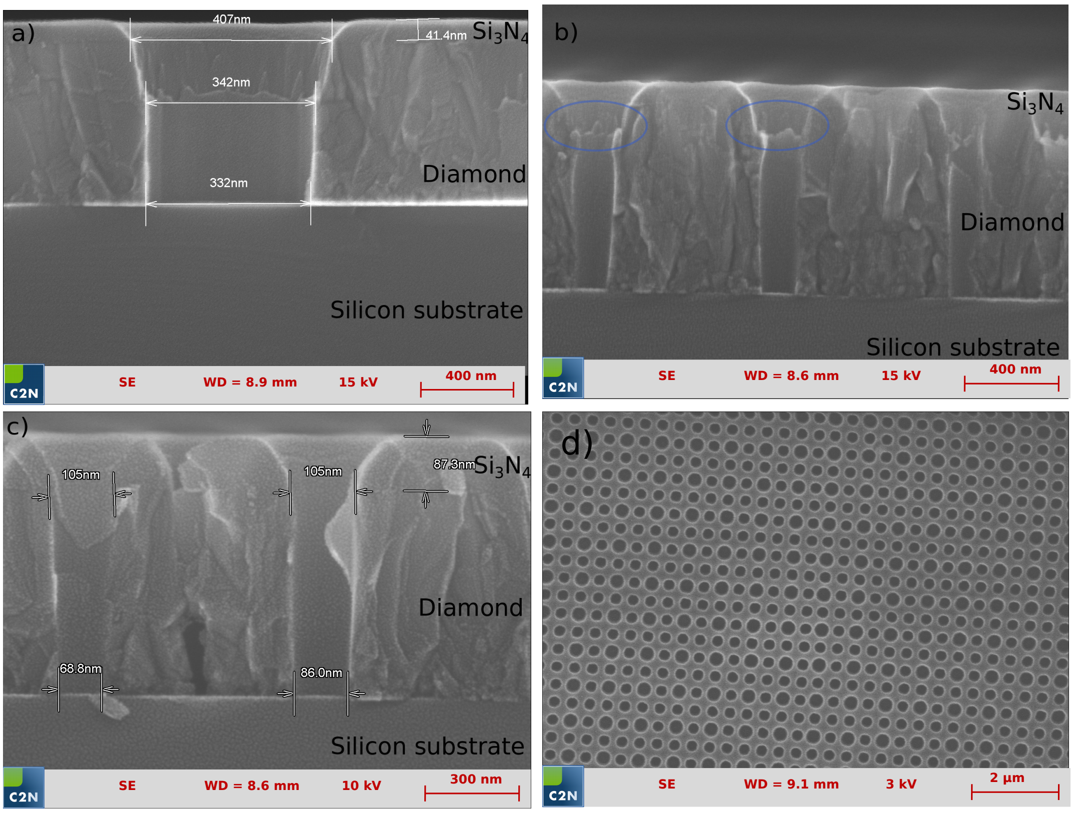

Figure 3.26: Diamond etching recipe optimization : a) and b) erosion of the mask for a $Si_3N_4$ film of 72 nm ; c) successful $Si_3N_4$ etch process for a mask film of 105 nm; d) top view of the PhC pattern transferred on diamond film after the nitride mask removal

| Parameters | Values |
|---|---|
| $O_2$ flow rate sccm | 120 |
| Coil Power W | 1800 |
| Platen Power W | 100 |
| Etch rate nm/min | 80 |

Table 3.10: ICP diamond etching parameters for PhC fabrication

film with a hole sidewall verticality better than 3° with a nitride mask of 105 nm. Different patterns were designed for diamond etching optimization, including hole diameters ranging from 90 nm to 340 nm. In Fig. 3.26 d) is shown the successful transfer of the desired pattern onto diamond, after nitride mask removal. The $Si_3N_4$ was removed by immersing the sample in HF acid diluted in DI water ratio 1:2 for 30 seconds.

The best configuration for diamond anisotrope etch for hole straight sidewalls fabrication and selective values over 1:18 for diamond : nitride mask are listed in the Table 3.10. The results are similar to C. Blin recipe on STS ICP.

Depending on sample substrate, two different cases are possible: complete etch of diamond film when the sample is grown / transferred on silicon, and the incomplete etch of diamond, in the case of quartz substrate. Both strategies will use the same nitride mask etch and diamond etch recipes.

### 3.5.7 Diamond 2D PhC realization on silicon substrate samples

Various strategies are conducted to find the best configuration of final optical biosensor. The optimized etching recipes presented in previous sub-sections are applicable to any structures on diamond (holes, waveguides, tapers etc).

After diamond etching, ZEP resist was destroyed by the ICP process, only the nitride mask is remaining on the diamond surface. In the configuration diamond on silicon substrate, the nitride layer can be removed by dipping the sample in HF solution 49% diluted in DI water ratio 1:2 for 30 seconds and washed in DI water. If we consider to realize suspended membranes, structure under-etch can be obtained by $XeF_2$ gas exposure, immediately after the sample immersion in acid, before the formation of native oxide on the silicon surface. $XeF_2$ gas is known in literature to etch silicon and to be inert for diamond, as well as for silicon dioxide or HSQ. The etch can be very rapid (a few hundreds of nanometers per second) and isotropic. In this way, the sample is not dipped in solution, eliminating the risk of film collapsing when under-etched. Fig. 3.27 a) shows an SEM image of a PhC cavity designed similar to the ones designed during the C. Blin thesis, where the sample was exposed to $XeF_2$ gas for a couple of tens of seconds to under-etch approximate 4 - 4.5 µm of silicon substrate (darker gray color). Higher magnification SEM image of the cavity

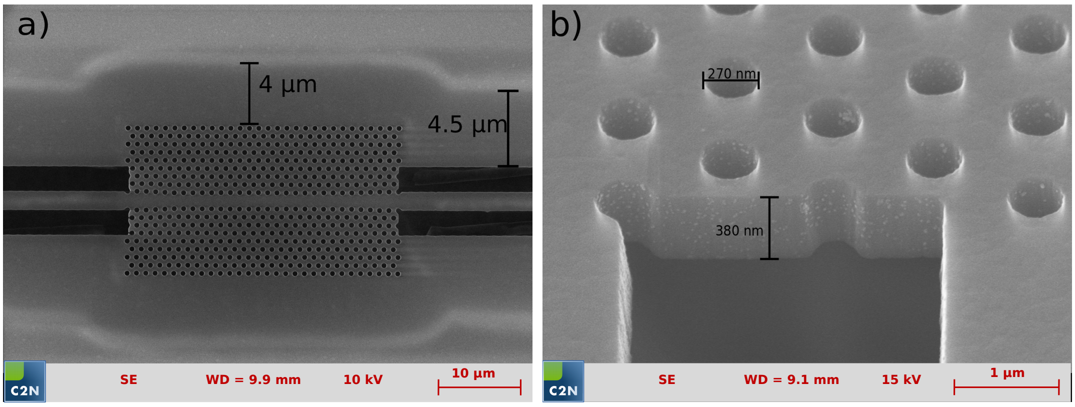

Figure 3.27: Diamond suspended membrane realized for designs proposed by C. Blin ([63]) a) top view ; b) 45° tilt

with a view at 45°, represented in Fig. 3.27 b), allow us to see the quality of the diamond etching process and also to measure the hole dimensions. The brighter spots on the holes sidewalls represents the gold nanoparticles remained from the metalization process from previous SEM acquisition.

In the case of diamond film transferred to silica on silicon substrate, under the diamond film are presented HSQ or silica layers. Dipping the sample into HF solution will remove the nitride mask, as well as the silica / HSQ under the diamond, with the possibility of diamond structure to collapse when dried using $N_2$ gas stream. The alternative method used is dry etching with HF acid vapors, where the etching reaction ends after the sample is removed from the HF vapors. The sample is placed a few centimeters above a HF container, vapors of the acid etching the remaining nitride mask, as well as HSQ / silica layers. The realization of suspended membranes is desired for device optical characterization in order to achieve higher Q factors. It is required that the diamond structure to be suspended in air at least 2.5 µm above the substrate. In the case where HSQ layer is placed under the diamond, followed by thermal silica and silicon substrate, I encountered the problem that the HSQ layer was etched more rapidly than the silica layer. I will recall that the HSQ layer is in general 200 nm thick and the silica layer was 2.5 µm thick. The under-etching using this configuration will rapidly etch laterally the HSQ layer and slowly etch vertically the thermal silica layer. The distance between two different structures can be as small as 25 µm, and as a consequence there is the possibility to delaminate the diamond film. To overcome this problem to establish an anisotropic etching, the HSQ film needs to be hardened. Studies demonstrates that by annealing the HSQ resist at high temperatures, the resist will be hardened and transformed into porous silicon dioxide ([89]). To achieve that, the sample is placed inside a oven under Ar gas closed environment. Different tests were performed to optimize the process temperature to have the same etch speed for HSQ

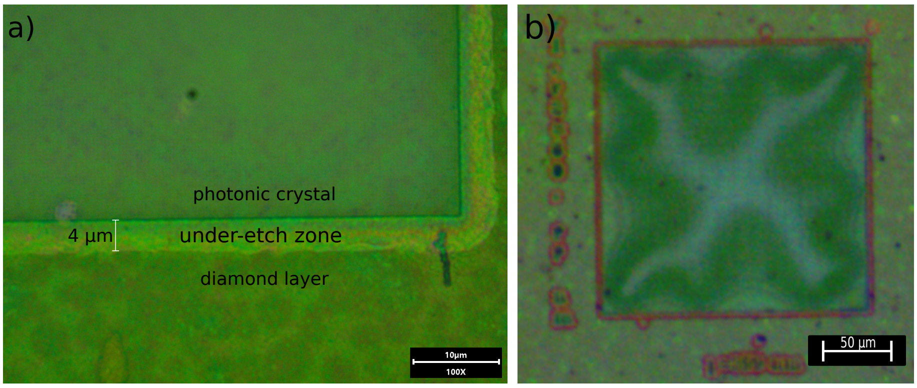

Figure 3.28: Optical microscope images showing the diamond sample under-etched, realized by annealing at 900°C and HF vapors exposure for 10 minutes. a) High magnification image showing the under-etched zone that surrounds the suspended photonic crystal ; b) Lower magnification image representing an entire PhC suspended in air.

and silica layers, while not damaging the diamond structures. The best results were found when the temperature was raised by 50°/ second and stabilized at 900°C for 1 minute, then cooled down. The sample was then placed above HF container for 10 minutes, resulting in a vertical etch rate of 50 nm/min and a lateral etching rate of 330 to 500 nm/min, showing an non-homogeneous under-etching with rough limits (Fig. 3.28 a) and b). I assume that the DOI configuration introduces constraints in the diamond film, from where the distortion of the diamond film, when suspended over a large surface area, as showed in Fig. 3.28 b). Due to the lack of time, I did not optimized further the design or try another strategy for realization of suspended structures on this kind of DOI. Further, the fabricated samples having this configuration were optically characterized without under-etching the HSQ and silica layers.

### 3.5.8 Diamond 2D PhC realization on quartz substrate samples

For diamond samples on quartz substrate (direct growth or transferred), part of the technological fabrication processes are optimized for these type of configurations (bonding method and additional conductive resist for EBL), but most of the processes involved in the device fabrication are compatible with the ones described for the silicon substrate (planarization, PhC patterning using EBL, etching or deposition). The device optical characterization is designed to probe the resonant modes of the diamond from the back side of the structure by light injection, leaving the top part of the sample for molecular interactions. There are two configurations considered for this PhD thesis : the first one includes similar strategy to realize PhC, as in the case of silicon substrate samples, with the difference that the diamond film is etched only half of the total thickness. This change was realized to eliminate the risk of trapping solution under the diamond film when liquid detection measurements are

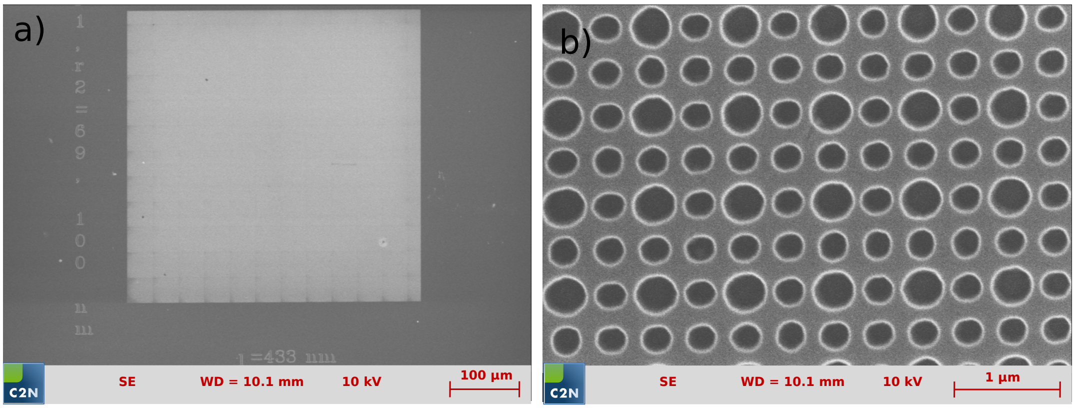

Figure 3.29: SEM images photonic crystals fabricated on quartz substrate (top view) : a) PhC overview representing the grid shape at the sub-field boundaries; b) Higher magnification SEM image showing the hole shape transferred onto diamond

performed. The second strategy considered is represented in Fig. 3.13 b), where the PhC is integrated under the diamond film. Unfortunately, due to the lack of time and unexpected delays, I did not succeed in realizing a final device using this configuration. In the next paragraphs I will present the first PhC realized on quartz substrate, with the diamond film grown directly on 1.2 mm thick quartz.

The diamond film thickness after surface planarization is 400 nm. Knowing that quartz substrate is an insulator, the DOI configuration makes the patterning with EBL difficult. Additional conducting layer was spin-coated prior to sample patterning to yield to a conductive surface. In the Fig. 3.29 a) is shown an SEM image of an entire $200 \times 200$ µm$^2$ PhC, where it can be observed the grid-shape at the sub-field boundaries. The same PhC with higher magnification is presented in Fig. 3.29 b) and it can be observed the pattern transferred on diamond film. The fabricated holes are not perfectly round, fact that, I presume is caused by the charge accumulation during the PhC writing. Nevertheless, the hole diameter realized in fabrication is equal to the coded one, with small holes diameters of 133-140 nm, big holes of 190-195 nm and a period of 424 nm. The distance between holes can be as small as 30 nm between a small and a big hole.

I think that the EBL process is not fully optimized for patterning PhC on quartz substrate, further tests needs to be done to fabricate with accuracy PhC on quartz, as we succeed to fabricate for diamond on silicon substrate. This first fabricated samples on quartz can serve to validate our hypothesis for optical characterization using light injection from the backside of the sample.

## 3.6 Validation of the fabrication recipes : micro-cavity photonic structures for infrared detection

The idea of fabricating the same photonic structures proposed by C. Blin, during her PhD thesis previously done in our group [63] was to verify the quality of the fabrication. As the polycrystalline diamond films are the same, we should achieve similar quality factors.

C. Blin proposed a 2D photonic crystal based on micro-cavity for near infrared detection on polycrystalline diamond. During my PhD thesis work, the PhC micro-fabrication processes were partly performed on different machines, thus including different recipes (see Chapter 3). The fabricated structures are the same as the designs proposed by the C. Blin. The realized PhC cavities were optically characterized and the results were compared to the ones reported by C. Blin.

The optical setup for PhC cavity measurement is composed from a tunable laser from 1500 to 1685 nm as light source, a photodiode which collect the light and direct it towards an oscilloscope that register the transmission spectrum and a polarizer at the exit of the sample to collect only the TE polarization. On top of the sample is placed a IR camera for sample positioning with the optical fibers.

The proposed design consists on a PhC cavity with a central slot and a local perturbation of the periodic hole arrangement (the position of several holes was modified). These introduced defects in the design lead to apparition of a defect mode in the photonic band gap of the PhC. Fig. 3.30 represents an example of transmission spectrum of a PhC cavity. The resonance of the cavity corresponds to the signal increase at the wavelength 1530.2 nm. The measured quality factor of this PhC cavity is around 6500, value similar with the one reported by C. Blin. It can be concluded that this are the maximum quality factor values for PhC cavities that can be achieved on ~ 400 nm polycrystalline diamond grown directly on silicon substrate.

## 3.7 Conclusion

Diamond, as material for photonic devices, is still facing some difficulties when speaking of realization of different designs over large surfaces with high reproducibility. The technological processes presented in this Chapter offers the possibility to fabricate various patterns on polycrystalline diamond. Micro-fabrication methods were developed and optimized for realization of photonic crystal structures on two different substrates, namely silicon and quartz.

Polycrystalline diamond smoothing protocol by spin-coating of a flowable oxide and dry etch ICP method were optimized to reduce the surface roughness RMS of films grown by

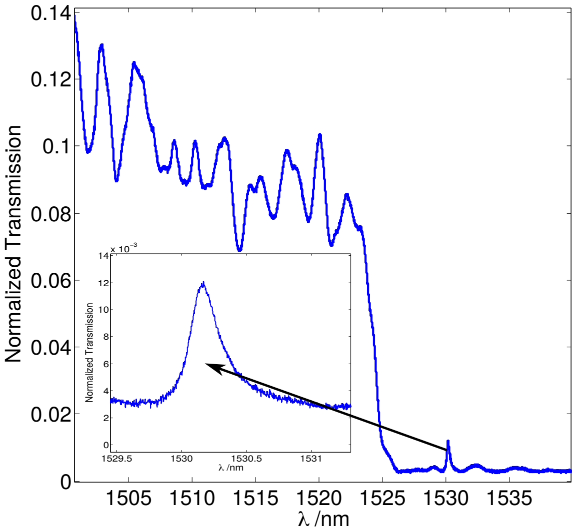

Figure 3.30: Transmission spectrum of a polycrystalline diamond slotted PhC cavity experiencing a quality factor of 6500. The inset represents a zoom of the resonance

MPCVD. This process can be applied to the polycrystalline diamond ranging from a few nanometer to several micrometer thickness films. As the diamond film thickness increases, the surface roughness also increases, reaching values up to 600 nm, with maximal peak-to-valley values of 1.2 µm for a 5 µm film. By applying the planarization processes, the surface roughness RMS can be reduced to 2.6 nm for a 5 µm thick film, values obtained by AFM measurements. In the case of thinner polycrystalline diamond films, AFM measurements show an roughness RMS value below one nanometer (724 pm and 449 pm). The planarization method result is rapid, does not require chemical mechanical polishing and the maximal rugosity that we can handle is twice the value that was reported previously in our group. Thanks to these results, the polycrystalline diamond films that can be processed increased to a maximal value of 5 µm.

Polycrystalline diamond film transfer method onto a new substrate was optimized. The goal of this method is to obtain thin films with better crystalline quality, with bigger diamond grains. In parallel to the transfer method, a dry etching ICP process was developed to thin the diamond films from a few microns to several hundreds of nanometers, resulting in thin films with large grains.

PhCs fabrication on diamond was realized using EBL method for different device configurations. In particular, optimization of nitride mask and ICP etching processes allowed us to realize vertical holes in diamond, with angles less than 3° for 120 to 340 nm holes diameter. The first PhCs realized on polycrystalline diamond film on quartz substrate show satisfactory results on HRSEM imaging.

# Chapter 4

# Optical characterization of diamond 2D PhC samples

## 4.1 Introduction

This Chapter deals with the optical characterization of the 2D polycrystalline diamond structures realized in the clean-room facilities and designed as described in the previous Chapters. As seen in the Chapter 2, the performances of the proposed PhC designs depend on a multitude of parameters (quality factor of the guided mode resonances, material absorption, light coupling strength from the free space to the PhC etc). Validation of the expected performances of the proposed biosensors are examined by different optical measurements. Firstly, the structure is analyzed by measuring the reflectivity spectra for various $\theta$ and $\phi$ polar angles, with a white light source and a spectrometer. These measurements will define the experimental band diagrams of the structure. The dispersion relations were studied to obtain the experimental device performances by testing different configurations : azimuthal angle changes to lower the group velocity for a desired resonant mode, temperature changes to vary the effective refractive index of the structure etc. A comparison between the fabricated and the theoretical dispersion relations can be obtained. After the examination of the structure with different configurations, the desired final measurement can be carried out to measure the real sensitivity value for the proposed device. The setup includes a visible wavelength laser, used as an external energy source, injected at a given angle, and the reflected light is detected by means of a camera. The actual performances values of the proposed PhC structures are calculated and the results are compared to the state of the art.

In the first part of the Chapter, the optical setup involved for measuring the band diagrams is detailed. The main parts of the setup will be presented, along with their main characteristics. The second part includes the interpretation and discussions of the measured band diagrams on the two different types of sample proposed, namely PhC structures realized on diamond film transferred to new silicon substrate with silica as intermediate layer and the PhC realized on diamond film grown on quartz substrate. Further, measurements at different temperatures are performed on one of the samples, which allow us to determine the PhC response to a refractive index variation, thus to calculate the sensitivity values of the proposed design. In the last part is presented the setup for the final sensitivity measurements and future perspectives.

## 4.2 Optical measurements for band diagram construction

The polycrystalline diamond structures obtained using micro-fabrication methods in cleanroom facilities were optically characterized by reflectivity spectra measurements. The results give the optical characteristics of the PhC and can be compared to the theoretical assumptions. The diamond biosensor was designed to detect at the limit of the visible wavelength range, more exactly at 795 nm. A preliminary study was performed to detect the overall optical properties of the structure by measuring the reflectivity spectra over a multitude of incidence and detection angles $\theta$ (from 20° to 80°). This study allows to construct the band diagrams of the device. To validate the assumption of decreasing group velocity of a targeted mode, measurements at different azimuthal angles were performed.

This section starts by describing the optical setup configuration used for the band diagram construction, followed by the representation and analysis of the reflectivity spectra.

### 4.2.1 Optical setup description

The setup used for measuring the optical characteristics of the 2D PhC is shown in Fig. 4.1. To measure the band diagram, the incidence and detection angles are simultaneously changed for a large $\theta$ angle range by means of two synchronized arms. Each arm have attached a polarizer and a collimator, through which the light coming from one side from a white light source is detected in the opposite side by a spectrometer. The sample is positioned to a rotary stage. The arms are controlled by a home made program and the acquired data from the spectrometer during the measurement are recorded in a computer for further treatment. In the next paragraphs I will detail each part of the setup.

#### 4.2.1.1 Light injection

Light is injected from a white source (360–2600 nm) ([109]). In Fig. 4.2 a) is represented the corresponding spectral power distribution of the source (blue line) compared to an ideal

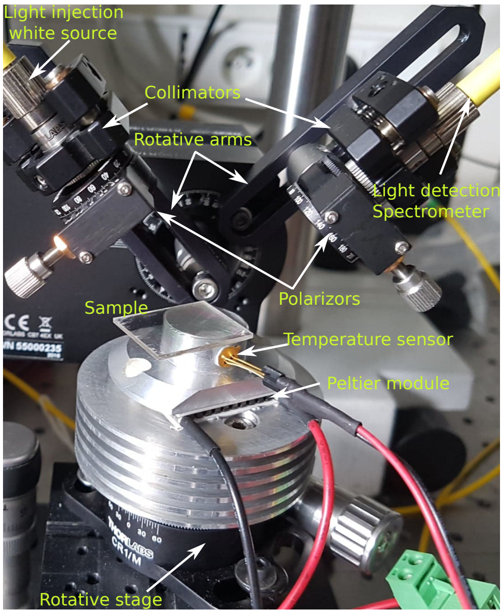

Figure 4.1: Side view image of the optical characterization setup for band diagram measurements of the fabricated photonic crystals structures

black body radiation at 1500 K. It can be observed that the light radiation is generated mostly in the IR region.

The light is directed through a optical fiber and a collimator to the sample. The optical fiber is a single-mode fiber at 780 nm which transmits the light from the light source to the sample. A collimator is used at the fiber output. The light spot size is around 100 µm in diameter for 20° incident angle and larger at higher incidence angles. A polarizer can be used to set s or p polarization of the incident light, where the s polarization will access TE GMRs and the p polarization will access the TM GMRs of the PhC structure under investigation.

#### 4.2.1.2 Spectrometer

At the opposite side of the light source is placed the detector. In the configuration shown in Fig. 4.1, another collimator, polarizer and optical fiber directs the light to a spectrometer. The wavelength range for detection is from 500 nm to 1000 nm, with a spectral resolution of 0.5 nm at 633 nm ([110]). The spectrometer is connected to a computer that will display the intensity of the signal detected at a given angle for a specified wavelength range. A reference spectrum was measured on silicon substrate for the white source, as shown in Fig. 4.2 b), spectrum which will be used to normalize the spectra of photonic crystal measurements.

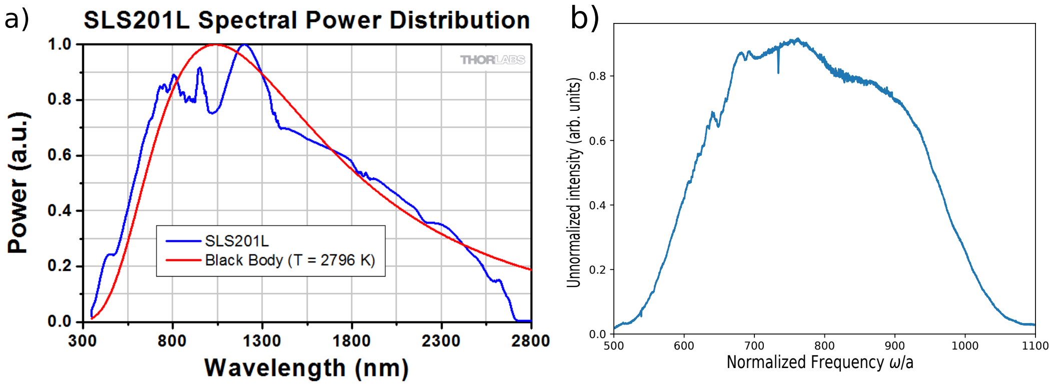

Figure 4.2: a) White light source reference spectrum from [109]; b) Measured spectrum with the white light source and the spectrometer for a Si wafer

#### 4.2.1.3 Rotative arms

The incidence angle is controlled by two arms with spep-by-step motors, which offers a theoretical accuracy of $3.44 \times 10^{-3}$ ° ([111]). The two arms share the same rotational axis, fact that allows to maintain the same detected light intensity for a large range of incident $\theta$ angles. The angle change is automatically controlled by a home made Python program. The collimators, the polarizers and the connectors for the optical fibers are fixed to the rotary arms identically.

#### 4.2.1.4 Rotative stage

The stage allows the manual displacement in the (x y) plane to move the sample to the desired photonic crystal for measurement. Taking into account the micrometric size of a PhC structure ($200 \times 200\ \mu m^2$), the precise positioning is executed by positioning an optical binocular above the sample.

The sample holder allows the rotation in the (x y) plane, which represents the azimuthal angle $\phi$. This rotation is performed for precise injection direction regarding the PhC axes. A tilt perpendicular to the injection / detection axis is also possible to adjust the sample position for a maximal signal detection.

#### 4.2.1.5 Setup adjustment

Prior to the optical measurements of a sample, the stage height is adjusted to maximize the signal intensity on the detector. The desired PhC structure on the sample is positioned at the plan of rotational axis of the two arms. We assure that the the two collimators (from the light injection and collection parts) are positioned accordingly to point the center of the rotation of arms, where the sample is placed.

#### 4.2.1.6 Different types of PhC designs measured using the presented setup

The dispersion relations at different incident $\theta$ angles can be measured for both types of samples proposed during this PhD thesis, namely polycrystalline diamond film transferred to a new silicon substrate and polycrystalline diamond film grown directly on quartz substrate.

In the case of diamond transferred onto another silicon substrate, the fabricated sample consists in a PhC realized in a diamond film of 385 nm thickness, an HSQ bonding layer of 400 nm just beneath, followed by a thermal silica layer of 2.5 µm and 300 µm of silicon as substrate. This configuration was used for optical measurements because the diamond film quality is better than other configurations (bigger diamond grain sizes, illustrated in Fig. 3.14). The PhC structures realized on diamond film were designed to be suspended in air by under-etching the HSQ and thermal silica layers. When the PhC structures were suspended by removing the silica layer underneath, we observed that the diamond film had visible distortions (Fig. 3.28). We assume that the diamond on insulator configuration constraints the material, which leads to the distortion of the diamond film. For all other realized samples on silicon substrate, the diamond layer has been left in contact with the underneath layers. This fact will introduce unwanted interferences when the optical measurements will be performed. Nevertheless, the guided mode resonances of the diamond photonic crystals will be visible on the reflectivity spectra measured, as it will be shown further in this Chapter.

A second PhC design is realized on diamond film (400 nm thickness) grown on quartz substrate (1.1 mm thick). The sample is characterized using the same optical setup as in the case of the silicon substrate sample.

This measurement describe the preliminary results that help us to verify that the fabricated structure has the same dispersion relations as in the corresponding numerical simulations.

### 4.2.2 Band diagram measurements for PhC structures realized on silicon substrate

#### 4.2.2.1 Numerical simulations for the fabricated PhC strucutres

The PhC designs realized on silicon substrate with silica as intermediate layer are measured using the described setup from Fig. 4.1. The numerical simulations provided in Chapter 2 shows the band diagrams of the PhC structure suspended in air, without any interference between the diamond GMRs and other layers under the diamond film, such as the silica or silicon substrate. On the contrary, on the realized samples configuration, the diamond film is not suspended in air, but rests on the silica layer. The presence of this layer under the diamond film induces the apparition of new modes and renders the band diagrams harder to deciphered. Additional numerical simulations were done with parameters from the realized samples, including the silica layer, silicon layer and the size of holes, to compare the band diagrams of the simulated PhC with the measured ones. In Fig. 4.3 a) is represented the band diagram calculated in the Γ X M Γ directions with the parameters from the fabricated PhC sample. To decrease the light speed propagation of a desired GMR, one have to find a suitable leaky mode that has the same frequency for two different wavevectors: one at the Γ point and the second one at some particular k wavevector between the high symmetry X and M points (the pointed out GMR by red arrow at 0.48 at Γ point in Fig. 4.3 a). The interrogation in that particular direction (here at $\phi = 26°$ from the Γ X direction) will modify the dispersion curves of all the modes of the structure and for the targeted GMR, the group velocity will be decreased, as illustrated in Fig. 4.3 b). The same structure was calculated as being suspended in air (Fig. 4.3 c). If we compare the results from the two cases for the same PhC structure, we observe that the GMR experiences a slight frequency change between the air suspended case and the SOI case. This result represent an asset of the proposed device, showing that the device experiences the same behavior for the GMRs in the configuration with silica and silicon layers under the diamond film, as in the case of PhC diamond suspended in air. By slightly changing the $\phi$ angle, we manage to correct the frequency difference for the targeted GMR to match a certain fixed frequency.

Further, the measured dispersion relations of the fabricated PhC samples will be discussed, presenting the physical phenomenon that take place once the light is injected into the PhC. The results will be compared to the numerical simulations at various light injection directions. Different setup configurations for light polarization will be presented, mentioning the advantages and drawbacks for each case.

#### 4.2.2.2 Fabry-Perot interferences

An example of the signal measured by the spectrometer at a given polar angle with light coming from a white light source is shown in Fig. 4.4. It can be observed intense interferences over the whole spectrum, which resembles to Fabry-Perot interferences. Superimposed to the first mentioned interferences, intensity dips of Fano type are present on the measured spectrum (pointed out by red color ellipses). We make the assumption that the Fabry-Perot interferences are related to the reflection occurring between the diamond film and the silicon substrate. The interference is maximally constructive when the optical path length between the reflected waves attains a phase difference $\delta$ that is an integer multiple of $2\pi$ with :

$$\delta = \left(\frac{2\pi}{\lambda}\right) 2 \text{ n l} \cos(\theta) \tag{4.1}$$

where $\theta$ is the angle of light with the normal in the silica, l is the thickness of silica, n is the refractive index. The free spectral range is given by :

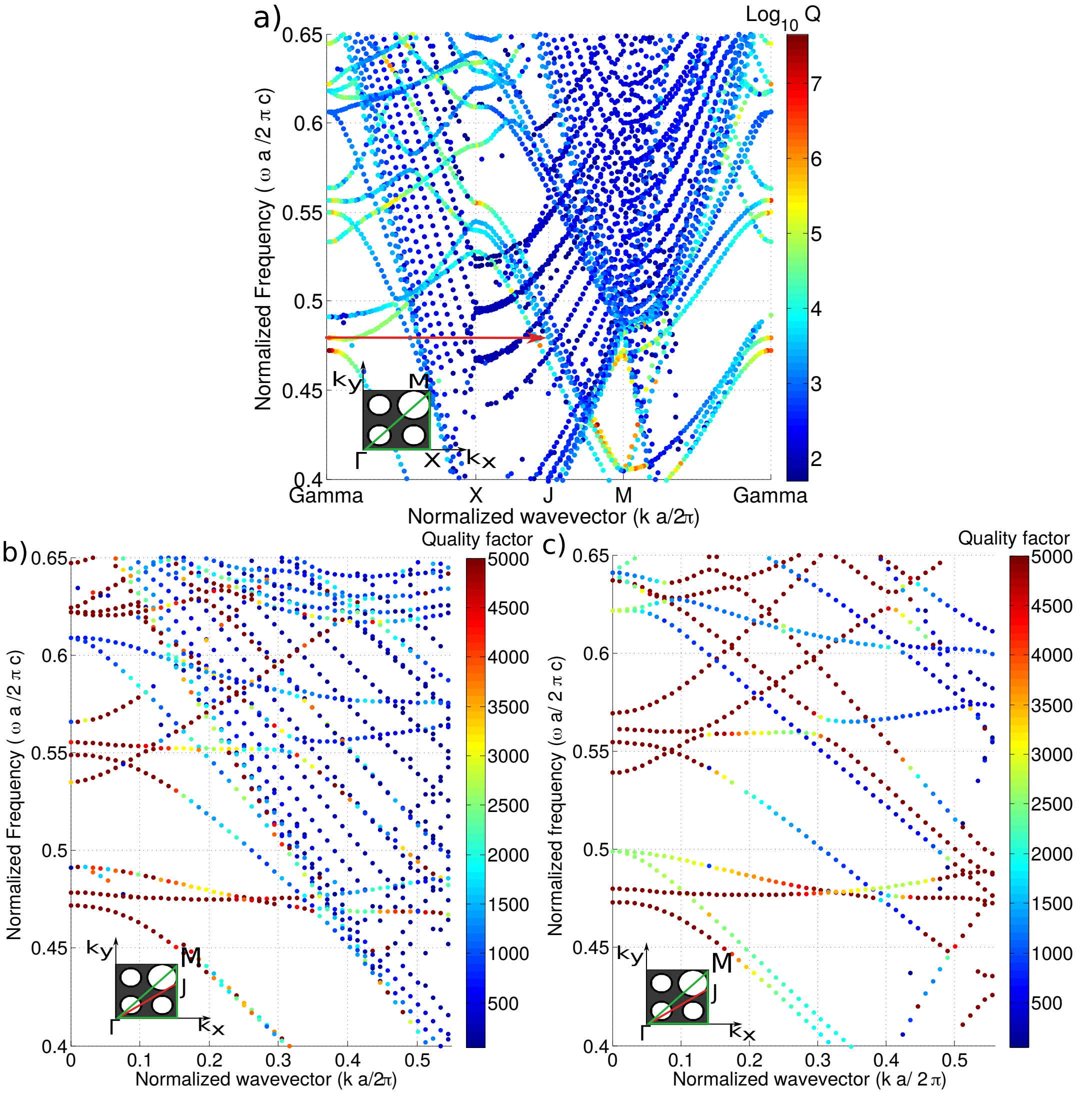

Figure 4.3: a) Band diagram calculation for TE modes with Q factors expressed on a logarithmic color scale. The inset represents the fundamental cell and the Brillouin zone Γ, X and M. The fundamental cell has four holes organized along a square lattice. The radius of the three similar holes is 0.14a, while the radius of the forth hole is 0.195a. The thickness of the slab is 1.02a. b) Band diagram calculation for TE modes along the specific direction $\Gamma$ J that makes an angle of 26° with the Γ X direction. The Q factors are represented on a linear scale with a maximum value of 5000 emphasing a value about 2500 near the light line for the targeted low group velocity mode, i.e for $\omega \approx 0.47$ and $k \approx 0.36$; c) Corresponding simulated band diagram for the same structure suspended in air

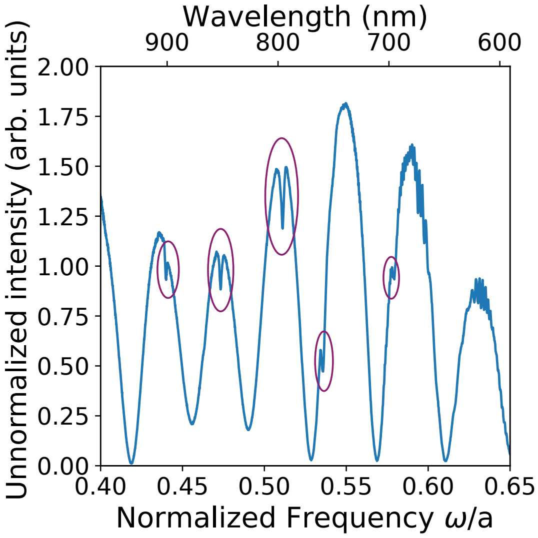

Figure 4.4: Typical measured signal by the spectrometer from the 2D PhC diamond sample for azimuthal $\phi = 26°$ and polar angle $\theta = 25°$.

$$\Delta\lambda = \frac{\lambda^2}{2 \times n_g \times L} \tag{4.2}$$

where $n_g$ is the group index ($n_g \sim 1.5$) and L is the product between the silica and HSQ layers multiplied by the cosine of the incident angle in material ($\mathrm{L = l \times \cos\theta}$). The calculated free spectral range $\Delta\lambda = 67\,\mathrm{nm}$ matches with measured $\Delta\lambda = 60\,\mathrm{nm}$, thus concluding that the Fabry-Perot fringes are related to the reflection occurring between the diamond film and the silicon substrate and passing through the silica and HSQ layers.

#### 4.2.2.3 Fano resonances

Superimposed on the background Fabry-Perot interferences, the spectra in the reflection also contains sharp resonances. These sharp features are Fano resonances related to the PhC diamond film. They are formed by the interference of two independent processes. The first one is a direct reflection / transmission on the slowly variation of the Fabry-Perot background. The second process is excitation of a guided mode resonances of the diamond PhC, because the light is first coupled to the PhC structure, propagates through the PhC and via second diffraction, the light leaves the PhC partly in the direction of the reflected beam and interferes with it. Fano resonances, in the case of photons coupling to the PhC leaky modes is given by ([112]):

$$\mathrm{R}(\omega) = \mathrm{R}_0 \left[1 + \frac{\mathrm{q}^2 - 1 + 4\mathrm{q}(\omega - \omega_0)/\gamma}{1 + 4\left(\omega - \omega_0\right)^2/\gamma^2}\right] \tag{4.3}$$

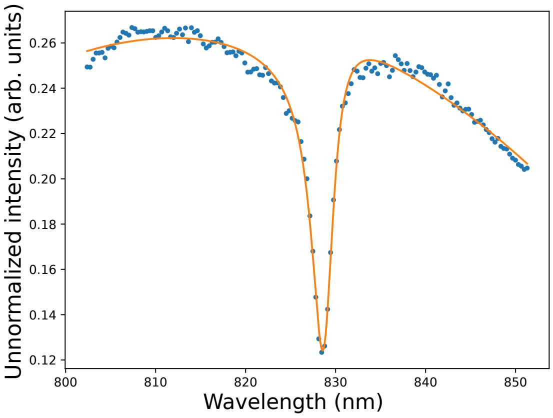

Figure 4.5: Fano-like feature measured at a given normalized frequency (blue dots) with the corresponding Fano fit (orange line)

where $\omega_0$ is the frequency of the mode, $\gamma$ is the resonance linewidth and q is a dimensionless parameter that describes the ratio between resonant and nonresonant transition amplitudes in the scattering process.

In Fig. 4.5 is shown a Fano feature for a GMR of a PhC, plotted in terms of wavelength versus the reflection intensity. Information about the guided modes can be extracted from this measurements, such as the spectral position $\omega_0$ and the spectral width $(\gamma, \mathrm{q})$. Here, $\omega_0$ =829.78 nm, $\gamma = 2.93$ nm which corresponds to a Q of 282. The energy leaks into the photonic crystal with a small phase shift (q = 0.163), which corresponds to an asymmetric intensity dip in the measured reflectivity spectrum. For q = 0, the GMR will present a symmetric shape, meanwhile for q with bigger value, the feature in the reflectivity spectrum will have a more pronounced asymmetric intensity dip shape compared with the example represented in Fig. 4.5, where the exact position of $\omega_0$ will be harder to determine without fitting the curve.

#### 4.2.2.4 Band diagram construction for $\Gamma$ X direction

The reflectivity measurement is repeated for a series of different angles from 20° to 80°, with a step of 0.1°. The resulting spectra are integrated to a single graphics, which represents the construction of the band diagram of the structure. In Fig. 4.6 a) is plotted the frequency in function of the colatitude $\theta$ angles, in the $\Gamma$ X direction. Here are represented the raw data, as measured, for s polarization configuration, setup configuration that will be explained later in this Chapter. In the reflectivity spectrum we can clearly observe the coupled guided mode resonances of the 2D diamond PhC, superimposed to Fabry-Perot fringes. At the angles where a GMR is found at a minima of the Fabry-Perot interference, the intensity of the scattered light is much lower than the one reflected by the Fabry-Perot effect and cannot be measured accurately.

To better represent only the dispersion relations of the diamond structure, a post processing of the data was applied. The Fabry-Perot was filtered by applying a notch filter that eliminates the slowly varying envelope of the Fabry-Perot effect. Even with the filtering, dispersion curves are hardly visible when at a minimum of the Fabry-Perot spectrum. The representation of the filtered data for the same PhC structure is shown in Fig. 4.6 b). The detected signal is expressing a high intensity over a large range of incidence angles, with a decrease of the detected resonant modes contrast over 75° from the normal incidence, due to the spot widening and the reflectivity dispersion of the light.

The fabricated structure was simulated to verify that the expected band diagram matches with the measured one, presented in the Fig. 4.6 a) and b). The simulation of the PhC was performed using the parameters from the measured structure : diamond film with thickness h=1.02a, the small holes 0.14a and the big hole 0.195a, silica under the diamond film with h=7a and silicon substrate h=a. The band diagram was calculated for $\Gamma$ X direction, and the result is plotted in terms of $\theta$ angle incidence versus the frequency (Fig. 4.6 c). The dispersion relations of the measured PhC structure fits well with the numerical simulation. One can observe two types of modes : the ones that are related to the PhC diamond and the ones related to the silica layer. To distinguish between the two types, simulation of the same PhC structure was calculated for a diamond membrane surrounded by air (Fig. 4.6 d). The presence of the silica layer under the diamond film in the fabricated sample increases the effective refractive index, thus lowering the energy of the diamond GMRs as compared to the GMRs of the diamond PhC membrane suspended in air. It can clearly be observed a decrease in the number of the modes, the additional resonances from Fig. 4.6 c) being related to the silica layer.

To conclude, the 2D PhC dispersion relations of the fabricated PhC can be measured with a good contrast of the diamond GMRs superimposed over Fabry-Perot interferences. The measured data can be filtered to remove the Fabry-Perot related to the silicon substrate and silica layer under the diamond film, while enhancing the Fano resonances related to diamond PhC structure. The presence of silica layer under the diamond film create additional resonances in the reflectivity spectrum. The structure was simulated using the fabricated parameters, and the result show a good match between the measured and calculated dispersion relations. Further, the structure was simulated in the configuration with the diamond film suspended in air to calculate only the GMRs related to the diamond PhC. The simulation of the PhC with silica layer under the diamond film increases the effective refractive index of the sample, thereby lowering the frequency of the GMRs as compared to the PhC suspended in air.

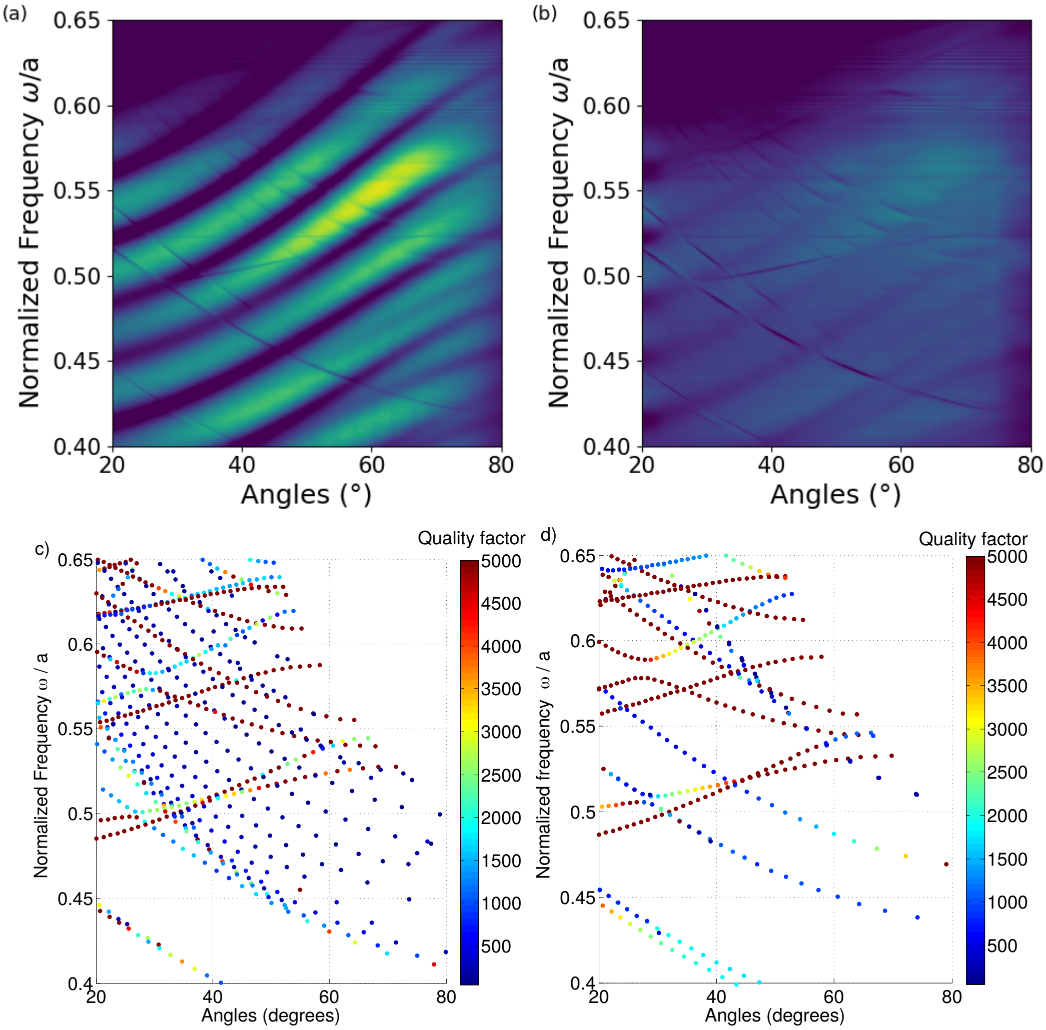

Figure 4.6: a) Measured band diagram corresponding to the PhC structure simulated in Fig. 4.3 a) .Here are represented the raw measured data in the $\Gamma$ X direction, for s polarization configuration; b) Corresponding measured spectrum with data filtered of Fabry-Perot interferences; c) Numerical simulation for the corresponding structure, including the silica layer and silicon substrate ; d) Numerical simulation for the corresponding structure suspended in air to highlight the diamond GMRs

#### 4.2.2.5 Low group velocity GMR measurement

In the previous paragraph, I described the band diagrams measured and simulated in $\Gamma$ X direction. One particularity of the proposed design is to decrease the group velocity of a desired GMR, property that allow us to overcome the expected sensitivity values found in the literature. This GMR behavior can be achieved by changing the azimuthal angle $\phi$ for light injection. According to the simulations, the targeted GMR can be slowed down by interrogating the PhC structure on a particular direction, different from the $\Gamma$ X or $\Gamma$ M directions. This implies for the optical setup the rotation of the sample carrier stage towards the diagonal direction of the squared PhC arrangement. The dispersion relations of the PhC are measured similarly as described for Fig. 4.6 a), with an in-plane interrogation direction of 26° from the $\Gamma$ X direction (Fig. 4.7 a). At this azimuthal angle $\phi = 26°$, the targeted leaky mode experience a group velocity as low as c / 100 for a large angle range from 60 to 63°. The measured data where filtered as mentioned in 4.2.2.4 to eliminate the Fabry-Perot interferences and to enhance the Fano resonances, as illustrated in Fig. 4.7 b). The targeted GMR was fitted by applying the Eq. 4.3 at different incident angles. At $\theta = 25°$, the Q was found to be 250, whereas Q around 500 were found at $\theta = 60°$.

The result of this measurement confirms the assumption of decreasing the group velocity of a targeted GMR when the light injection direction changes. The measured PhC is simulated with the parameters from the fabricated sample and represented in Fig. 4.7 c). It can be observed that the behavior of the targeted GMR experience a slow frequency variation over multiple $\phi$ angles of incidence, as in the case of the measured spectra. From Fig. 4.7 c) is calculated the group velocity of the structure when interrogated in this particular direction. The theoretical value of the group velocity for the targeted GMR's at $\theta = 60°$ is 0.003. The simulated quality factor of the targeted GMR at $\theta = 60°$ is around 2000. The difference from the two values (simulated and measured) can be related to the fabrication imperfections of the PhC and to the diamond absorption.

Fig. 4.8 illustrates only the band of GMR of interest at different $\phi$ injection directions. The example shown in Fig. 4.7 a) at $\phi = 26°$ is represented, along with measurements of different $\phi$ ranging from 20° to 30° from the $\Gamma$ X direction. These measurements were performed to determine the $\phi$ angles for which the targeted GMR experience a slow light propagation. Each set is fitted by a polynomial function of $\mathrm{k}_{||} = \frac{\omega}{\mathrm{c}} \sin\theta$. The derivative of the polynomial gives the value of $\frac{\mathrm{v_g}}{\mathrm{c}} = \frac{\mathrm{d}\omega}{\mathrm{dk}}$, which are depicted in colored log scale. The data is cut in several sets because of the contrast lost due to the Fabry-Perot. For the GMR interrogated at 26°, a group velocity of less than $\frac{\mathrm{c}}{100}$ was obtained and measured.

The frequency variation of the GMR as the $\phi$ angle changes represents an important feature of the proposed design. One can note that the GMR is expressing low group velocities over a large range of azimuthal angle. Unfortunately, the observation of a slow GMR at

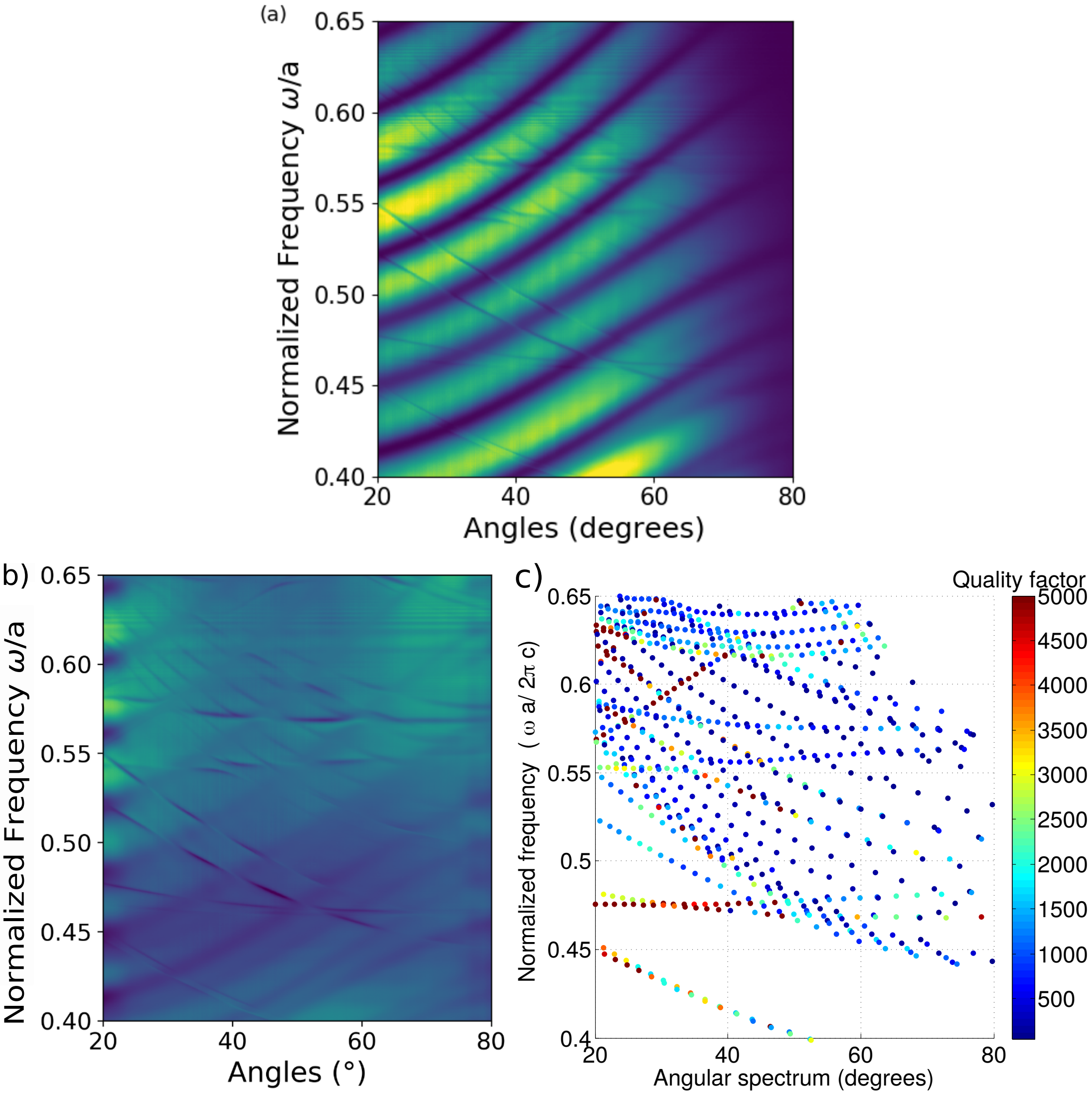

Figure 4.7: a) Band diagram of the same PhC structure measured in Fig. 4.6 a) as measured in the specific interrogation direction $\Gamma$ J (26° from the $\Gamma$ J direction) ; b) Corresponding measured spectrum with data filtered of Fabry-Perot interferences; c) Numerical simulation for the corresponding structure, including the silica layer and silicon substrate ;

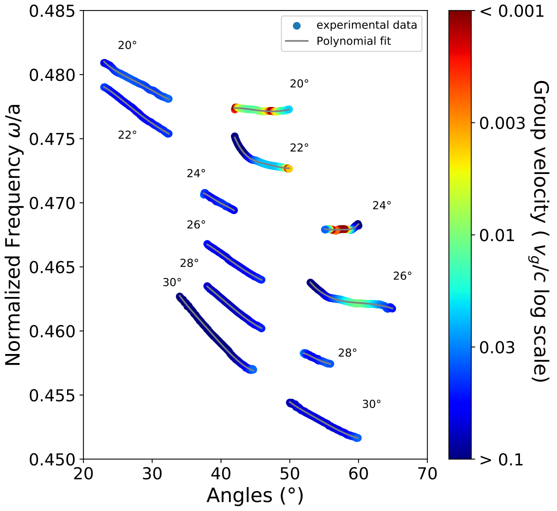

Figure 4.8: Normalized frequency of the mode as a function of the angle $\theta$ for various $\phi$ equal to 20°, 22°, 24°, 26°, 28° and 30°. Continuous lines correspond to the best polynomial fit and colors to the group velocity $v_g/c$.

$\phi = 30°$ is not possible for this PhC structure because of the minimum of the Fabry-Perot interference at high $\theta$ angles. The design offers an energy tuning of more than 5%, property that will be useful for the measurements using a fixed frequency, such as laser.

#### 4.2.2.6 Polarization influence

In the previous measurements, the band diagrams are measured without polarizers in Fig. 4.7 or with polarizers for s polarization in Fig. 4.6. In this subsection I will describe the influence of the light polarization on the different setup configurations that were tested.

In Fig. 4.9 a) is shown the same dispersion curves of a PhC structure as presented in Fig. 4.7 a), represented in terms of incidence angles versus the frequency. This setup configuration without polarizers can a priori measure both TE-like and TM-like GMR of the diamond PhC, as presented in subsection 4.2.2.5 in Fig. 4.7 c).

With the aid of the polarizers, it can be possible to detect only one polarization. Depending on the chosen polarization, it is possible to excite different GMRs, which corresponds to TE-like or TM-like GMRs. Fig. 4.9 b) represents the same band diagram measured for the same PhC structure and angles as in the case of Fig. 4.9 a) but with polarizers used to select s polarization only. The detected GMRs in the s light polarization are fewer than in the case without using a polarizer. The GMRs that are not present in the band diagram can be excited only using p polarization. Nevertheless, the targeted GMRs are detected in the reflectivity spectrum using this polarization configuration.

Another possible configuration of the setup is the cross-polarization, where the injected light is polarized, for example in s polarization, and the reflected light is detected for p po-

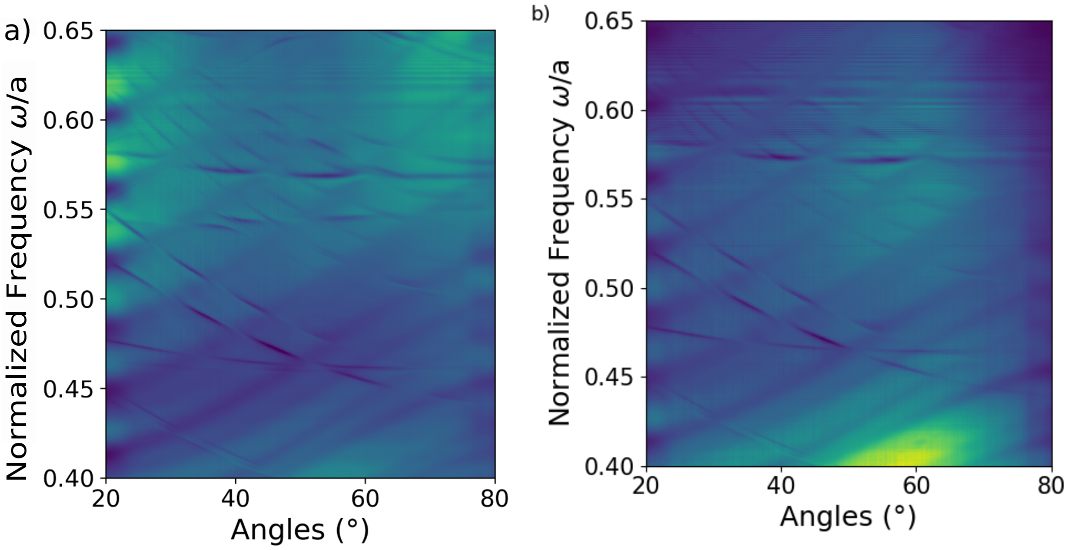

Figure 4.9: Band diagram of fabricated sample as measured in the interrogation direction $\Gamma J$ ($\phi = 26°$ from the $\Gamma X$ direction) a) without the use of any polarizers; b) with s polarization configuration.

larization. This setup configuration was measured for the same PhC structure as previously presented in Fig. 4.9. The reflectivity spectrum is shown in Fig. 4.10 a), with the mention that the interrogation direction was changed to $\phi = 28°$ from the $\Gamma X$ direction. The advantage of this strategy is that the Fabry-Perot interferences will no longer be detected, measuring only the diamond leaky modes, with high contrast (Fig. 4.10 b) represented for $\theta = 40°$). A drawback of this configuration is that the detected GMRs need to have the right symmetry, meanwhile the GMRs excited only for one polarization cannot be detected.

A last configuration was performed where the light was polarized at an intermediate value between s and p. However, the contrast was not improved for all angles of incidence due to what we presume to be a depolarization effect of the diamond on silica layers.

To conclude, in this part of the Chapter, I presented the optical setup that allowed the measurement of the band diagrams of the fabricated PhCs and to compare them with the simulations. The targeted GMR group velocity was decreased at low values when the interrogation direction was changed, thus validating our designs. An energy shift of more than 5% was achieved when the $\phi$ direction was changed, while maintaining the group velocity of the desired GMR at low values. Different setup configurations were tried in order to obtain the best contrast, advantages and drawbacks of each strategy being mentioned.

#### 4.2.2.7 PhC design for the detection of two GMRs at the same wavelength

The design was conceived to retrieve two different GMRs, eventually experiencing different group velocities for the targeted wavelength, angularly spaced. The reason to have two

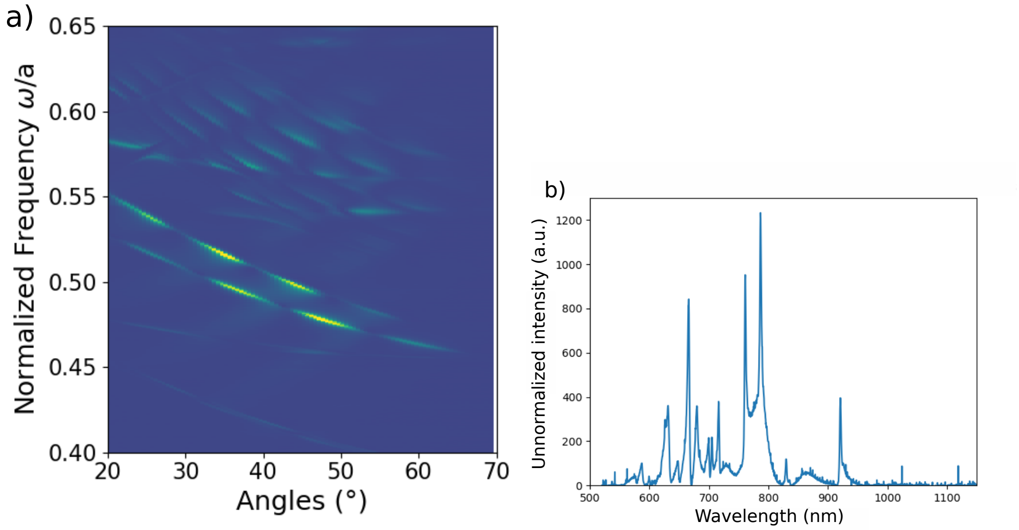

Figure 4.10: a) Band diagram of fabricated sample as measured in the interrogation direction $\Gamma J$ ($\phi = 28°$ from the $\Gamma X$ direction) using cross-polarization configuration ; b) Measured spectrum for azimuthal angle $\phi = 28°$ and polar angle $\theta = 40°$

leaky modes detection is for more precise measurements, two sets of data being available. Moreover, because the electromagnetic pattern of modes are different, we can expect that their penetration depth would be different and that we would be able to distinguish surface and background refractive index changes. As an example, for the measurements presented in Fig. 4.7, if we imagine an horizontal cut at the normalized frequency $\omega = a/\lambda$ of 0.47175, the resulting plot for all the angles have the features as shown in Fig. 4.11 a). The measured data include the Fabry-Perot interferences for this setup configuration. At the angles where the GMRs crosses this particular wavelength, a decrease in intensity is observed (pointed out in red ellipses). The features of the GMRs are not well defined in the raw data. If the Fabry-Perot interferences are subtracted from the data by applying a filter to the measured data, the remaining detected features will be those related to the GMRs detection, as represented in Fig. 4.11 b). The first dip feature at 26° represents the targeted slow GMR and the second feature detected at 46° is the rapid GMR. The two leaky modes can be tuned to be detected at closer $\theta$ angles by changing the azimuthal angle injection.

### 4.2.3 Band diagram measurements for PhC structures realized on quartz substrate

The PhC realized on diamond film with quartz as substrate are measured using the optical setup described in 4.2.1. The design was optimized starting by simulating the band diagrams in the Γ X M Γ directions, followed by calculating the dispersion relations in the direction where the targeted GMR express a low group velocity (see subsection 2.4.5.1). The

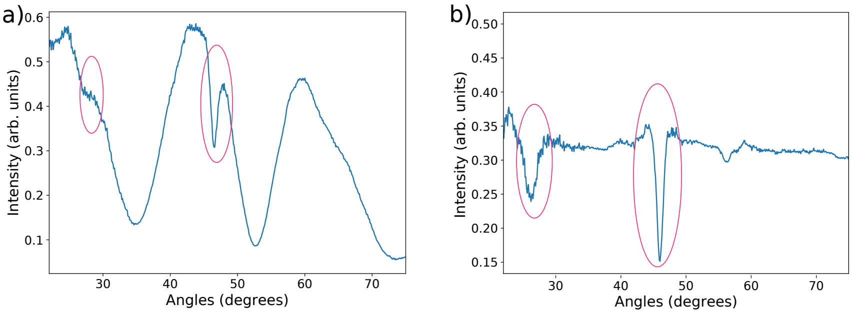

Figure 4.11: a) Angular reflectivity of the fabricated sample as measured at a fixed frequency interrogation $\omega = 0.47175$ in the interrogation direction $\Gamma J$ ($\phi = 26°$ from the $\Gamma X$ direction); b) Corresponding angular spectrum with data filtered of Fabry-Perot interferences

fabricated sample design is observed on HRSEM to compare the actual dimensions of the PhC (hole diameters, period, thickness etc) with the desired ones. It was observed that the holes diameters are smaller than coded, thus simulations with parameters from the realized sample were calculated.

The results obtained from the diamond PhC on silicon substrate allow us to perform measurements for the particular light injection direction where the desired GMR experience a low group velocity. The numerical simulations show that by changing the azimuthal angle light injection to $\phi = 30°$ from the Γ X direction, the targeted GMR will have a slow light propagation.

In the Fig. 4.12 a) are illustrated the dispersion relations of the diamond PhC structure on quartz substrate, as measured, interrogated in $\phi = 30°$ azimuthal angle from the Γ X direction. The measured dispersion relations are compared to the numerical simulations (Fig. 4.12 b). One can observe the good agreement between the two diagrams, with the mention that not all the simulated modes that appear in the diagram are well observed in the measurements. The design of the structure was optimized in order to have a low group velocity targeted GMR experiencing a Q of around 1000 at $\theta = 50°$.

Fano resonances related to the diamond PhC are clearly observed on the measured spectrum. The advantage of this configuration compared to the diamond on silicon substrate is that there are no intense Fabry-Perot interferences, the GMRs being visible over all the $\theta$ angles of the diagram. The detected signal is intense over a large range of incident $\theta$ angles. The contrast of the detected GMRs decreases over 70° from the normal incidence mainly due to the spot widening. The targeted GMR at $\omega = 0.53$ has a low group velocity as low as c / 100 over a large range of $\theta$ angles from 55° to 80°, thus validating the theoretical assumptions.

The spectrum measured at $\theta = 50°$ is represented in Fig. 4.12 c), from where it can be noticed the coupled diamond GMRs superimposed over a slowly varying background, related to the light source and spectrometer. The GMRs detected shapes in the reflectivity

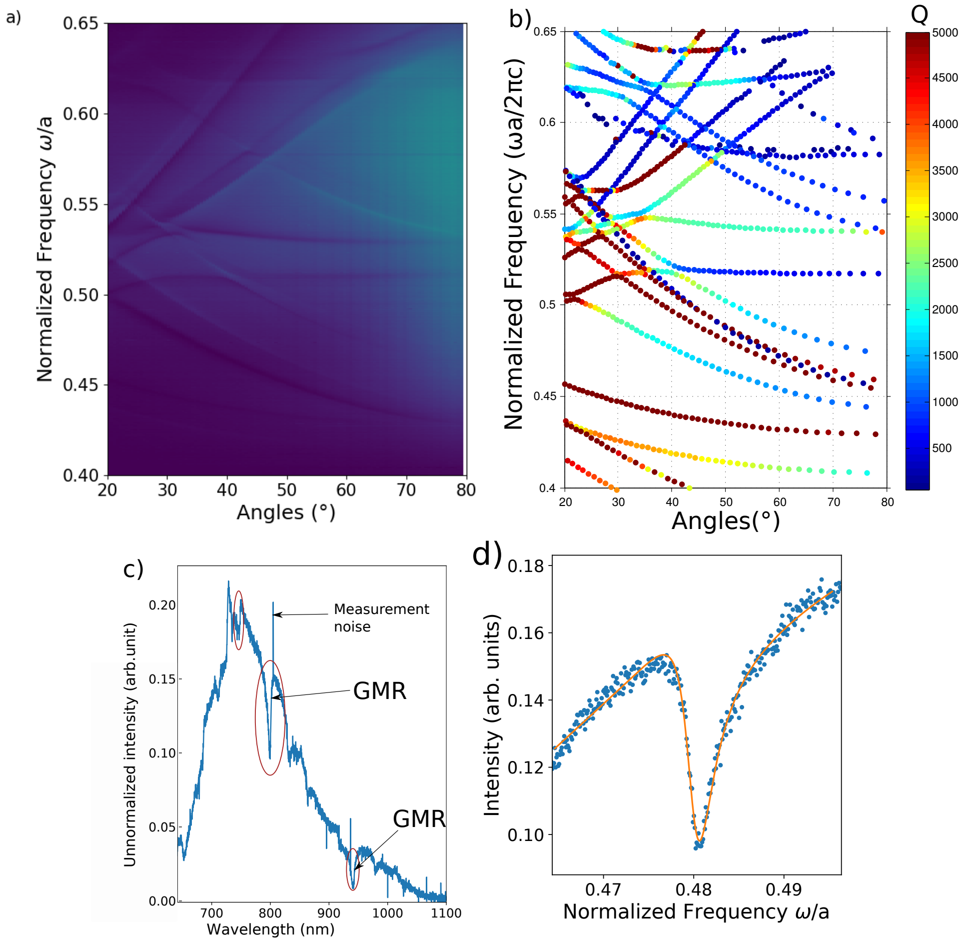

Figure 4.12: a) Band diagram of fabricated sample as measured in the specific interrogation direction $\Gamma J$ (30 ° from the $\Gamma X$ direction) ; b) Simulated band diagram for the corresponding structure from a) ; c) Measured spectrum for azimuthal angle $\phi = 30°$ and polar angle $\theta = 50°$; d) Fano-like feature measured (blue dots) and fitted by a Fano-feature (orange line) expressed in Eq. 4.3 for the GMR found at $\lambda = 884$ nm.

spectrum have Fano-like features. For example, the GMR found at 884 nm wavelength is fitted by a Fano-feature expressed in Eq. 4.3. The result is illustrated in Fig. 4.12 d) and shows a $\gamma = 3.4 \times 10^{-4}$, which corresponds to a Q of the detected leaky mode of 135. The factor q=2.7 corresponds to the asymmetric feature detected.

Compared to the measured results, the Q factor of the leaky mode from simulation has higher value. New losses related to lithography on a highly insulating material as quartz are added, fact that lowers the Q of the targeted GMR.

To summarize, the dispersion relations of two different sample configurations were measured, namely PhC diamond film transferred to a new silicon substrate with silica as intermediate layer and PhC diamond film on quartz substrate. The theoretical assumption for group velocity decrease was validated by changing the azimuthal $\phi$ angle for light injection for both configurations. The measured spectra are in good agreement with the corresponding band diagrams from the numerical simulations.

## 4.3 Sensing properties of diamond PhC

This part deals with the sensing characteristics of the PhC structure, which is one of the evaluation parameters of a biosensor. I will recall that a refractive index biosensor measures the shift of a GMR of a PhC structure (frequency change, expressed in nanometers or angular shift, expressed in degrees) when the refractive index of the surrounding medium is changed.

Due to the limited time and difficulties encountered during the fabrication of the samples, bio-detection tests for the fabricated samples were not realized during this PhD thesis.

The measurements realized for the diamond PhC samples shown in subsection 4.2.2 were performed in a controlled temperature environment. It is known that a temperature fluctuation induces an effective refractive index change of the measured structure, which translates to energy variation of the detected GMRs. Measurements of the same PhC structure at different temperatures were performed and the results allow us to calculate the expected sensitivity values of the proposed sensor.

In the next part I will present the temperature influence for the designed biosensor, followed by calculating the expected sensitivity values of different GMRs from the measured values. Further, the final optical setup for sensitivity measurements will be detailed and the optical characterization of the fabricated PhC will be analyzed.

### 4.3.1 Temperature change measurements

The measurements presented up to this moment were carried out in controlled temperature, to avoid any unwanted energy shift of the diamond leaky modes. In the next part I will focus on the behavior of the PhC structure when the temperature is changed in a controlled way. A comparison between a large and a low group velocity is presented, from where it can be pointed out the interest of a slow light propagation inside a targeted GMR.

The setup is basically the same as presented for previous measurements, shown in Fig 4.1. A thermoelectric device is inserted under the sample holder to control the temperature. A temperature sensor is placed just below the sample, incorporated into the aluminum piece. The temperature change is produced by a thermoelectric device that uses the Peltier effect, meaning that the device can be cooled down or heated up. The temperature is stabilized with the aid of a proportional- integral-derivative (PID) controller. The measurements were performed on the same PhC structure, following the targeted GMR behavior at different azimuthal angles, resulting on the measurement of various group velocities.

Before calculating the corresponding sensitivity values of this diamond PhC structure related to the temperature measurements, it is necessary to verify certain hypotheses that allowed us to formulate the sensitivity equation for the proposed design. The temperature derivative of the diamond and silica refractive indexes, namely the thermo-optic coefficients, is expressed as ${}^{dn}\!/\!{}_{dT}$, has a value of $9.8 \times 10^{-6}$/K at 589.3 nm for diamond ([113]) and $8 - 9 \times 10^{-6}$/K for silica ([**?**, **?**, **?**]). In the case of heating up the sample, the refractive index should increase, thus lowering the energy of the diamond guided mode resonances.

The second assumption is that the refractive index change of the structure is proportional to the frequency change of the GMRs. This relation was described by the perturbation theory from the Chapter 2 (Eq. 2.1).

The results from the measurements at different temperatures indeed induce a frequency change of the modes. In Fig.4.13 a) is represented the targeted GMR measured at $\phi = 30°$ from the $\Gamma$ X direction (Fig. 4.8 30°). The data were fitted similarly, as described for the data representation from Fig. 4.8. The fit is obtained by applying a third degree polynomial function in $k_{||}$ and the derivative of the polynomial gives the value of $v_g/c$, which are depicted in a colored scale. The temperature was changed at 35°C, 50°C and 80°C respectively, as shown in Fig. 4.13 a). It can be observed that the behavior of the GMR is not changed, only it's energy is shifted. An unexpected phenomenon for the detected leaky modes is produced : the frequencies of the GMRs increased once the temperature was raised, while the thermo-optic coefficient indicates the contrary. The sample was cleaned in isopropanol solution, then rinsed with DI water. The experiment was performed again, having the same result. A third measure was done by increasing the temperature from room-temperature to 65°C and maintained the sample for one hour at 65°C. The result was similar as in the other two cases, concluding that the measurements are reproducible. One explanation to this phenomenon can be the desorbption of absorbed molecules at the surface of the sample when the temperature was increased as shown in ([114]). We did not examined this issue further. For the further calculations, we consider that the refractive index change $\Delta$n as being proportional to the temperature variation $\Delta$T.

The $\Delta\omega$ related to temperature change from 35°C to 50°C for the angle for angle 40° is $1.22 \times 10^{-4}$. If the same PhC structure experience a greater temperature change, from 50°C to 80°C, the $\Delta\omega = 1.62 \times 10^{-4}$. In the case of determining the angle shift for a particular wavelength (for example $\omega = 0.459$ from Fig. 4.13. a), the GMR angle will be shifted by 0.236° when the temperature is raised from 35°C to 50°C. Similarly, for a bigger temperature raise from 50°C to 80°C, the coupling angle will be shifted by 0.309°.

In the first shown example of temperature change, the targeted GMR was monitored for a direction where it experienced a group velocity of $v_g/c = 0.115$. In the next example, the same targeted GMR of the same PhC is considered, but the light injection direction is changed to $\phi = 26°$ (Fig. 4.8), where the leaky mode experience a lower group velocity, namely $\mathrm{v_g/c} = 0.013$. The temperature measurements for this targeted GMR were performed at 65°C, and the temperature was varied by ±2.5°C, as depicted in Fig. 4.13. b). In the case where the temperature was raised from 62.5°C to 65°C, at $\theta = 45°$ incident angle, the $\Delta\omega$ is found $5 \times 10^{-5}$, whereas from the temperature changes from 65°C to 67.5°C, for the same $\theta$ angle, the frequency shift is $4 \times 10^{-5}$. For the described conditions, the targeted GMR express a 0.5° coupling angle shift for the $\omega = 0.47605$ for 2.5°C variation.

Figure 4.13. c) shows the angle variation $\Delta\theta$ of the same GMR interrogated in different directions (see Fig. 4.8) plotted against the temperature. The first mode ($\theta = 37°, \phi = 30°, \omega = 0.46$) presents a group velocity $\mathrm{v_g/c}$ of 0.08 (green squares), the second one ($\theta = 58°, \phi = 30°, \omega = 0.452$) a $v_g$ of 0.04 (red circles) and the third one ($\theta = 45, \phi = 22, \omega = 0.473$) a $v_g$ of 0.013 (purple triangles). The fastest mode experienced a shift of 1° over 60°C, the second one a shift of 2.5° over the same course. The slowest mode was interrogated only over 5°C from 62.5°C to 67.5°C and already showed a shift of 1°. The $\Delta\theta$ shift for the fastest GMR (green squares) is three times smaller than of the slowest GMR (purple triangles) measured from the temperature variations measurements. It can be concluded the interest for having a targeted GMR experiencing a low group velocity compared to a large group velocity one.

I will recall the proposed definition for the sensitivity for this type of biosensor, demonstrated in the Chapter 2, as :

$$\text{Sensitivity} = \frac{\Delta\theta}{\Delta \mathrm{n}} = \frac{\Delta\ \omega}{\mathrm{v_g}\ \Delta \mathrm{n}} \times \frac{1}{\omega \times \mathrm{n_{environment}}} \times \frac{1}{\cos\theta} \times \frac{180}{\pi}\ [°/\mathrm{RIU}] \tag{4.4}$$

where $\Delta\omega$ represents the normalized frequency change due to a refractive index change on the structure, $\Delta$n is the refractive index variation experienced by the PhC, $\omega$ is the normalized frequency of the GMR and $\theta$ is the colatitude angle from the surface normal direction.

From the Eq. 4.4, we deduce that, for small angle and refractive index changes, there exist a linear relationship between $\Delta\theta$ and ${}^{\Delta\,\omega}\!/\!_{(\omega\times\cos\theta)}$, with a proportionality factor of $\frac{180/\pi}{\mathrm{v_g}}$ .

To analyze this aspect, Fig. 4.14 shows the same angle shift as the one in Fig. 4.13. c) but with abscissa replaced with the relative frequency shift ${}^{\Delta\,\omega}\!/\!_{(\omega\times\cos\theta)}$.

As expected a good linearity relation is achieved between angle shift and the frequency shift (dotted lines). Moreover, in Fig. 4.14 are also represented straight lines with slopes equal to ${}^{1}\!/\!_{\mathrm{v_g}}$ calculated directly from the unperturbed band diagram. As can be seen the straight lines have almost the same slope as the one of a linear fit to the data. We show here two independent measures of the group velocity, one with a change of the coupling angle and frequency with the temperature through the Eq. 4.4, and one directly from a band diagram

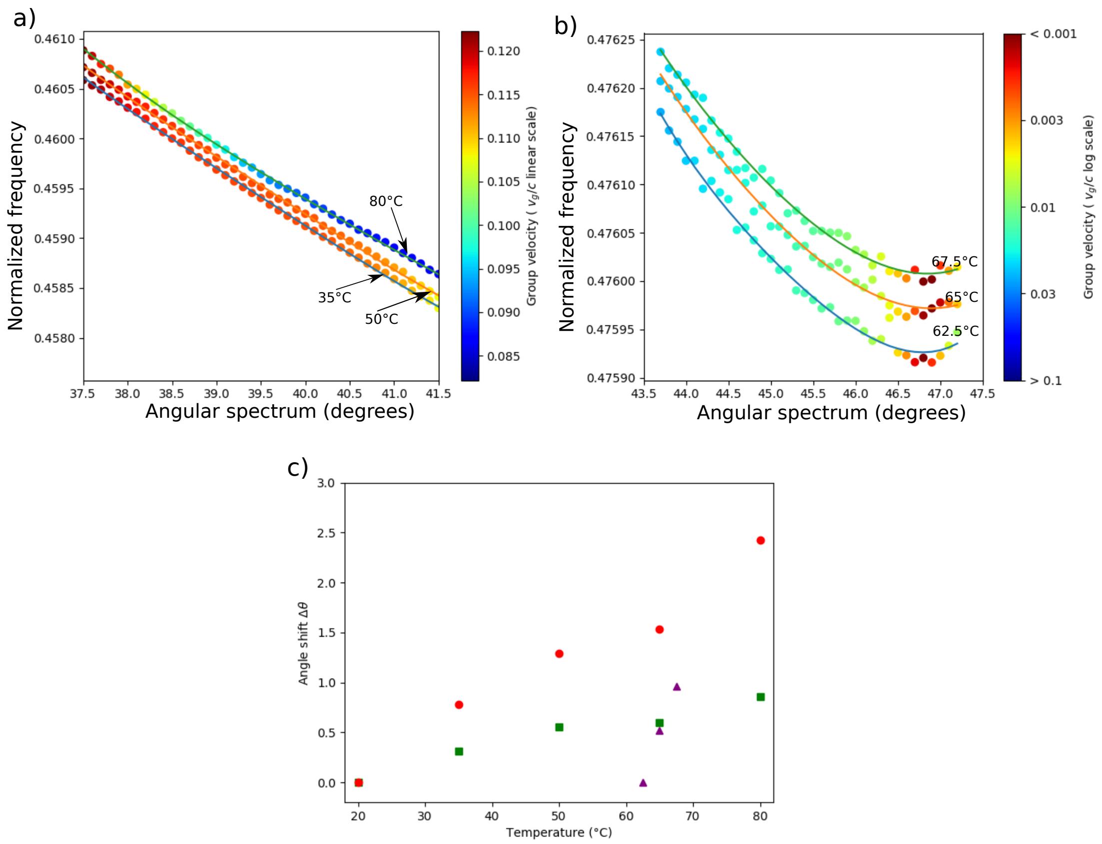

Figure 4.13: a) Frequency shift with the temperature change (35°C, 50°C and 80°C) for the same GMRs experiencing a $v_g/c = 0.115$ ; b) Frequency shift with the temperature change (62.5 to 67.5°C) for the same GMRs experiencing a $v_g/c = 0.013$ ; c) Angle shift with the temperature for three mode with three group velocities : $v_g/c = 0.08$ (green squares), 0.04 (red circles) and 0.013 (purple triangles)

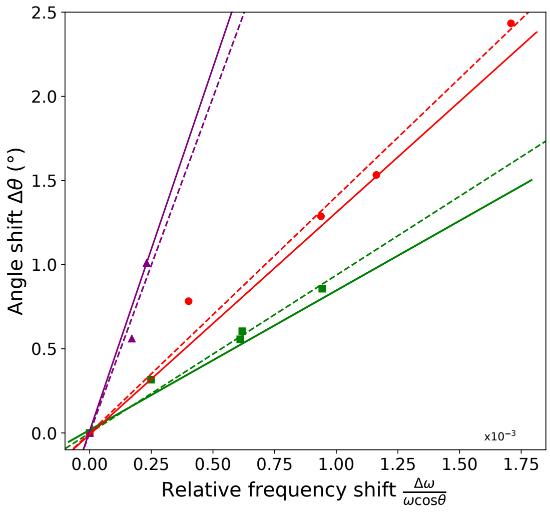

Figure 4.14: Angle shift as a function of the relative energy shift using same symbols as for Fig. 4.13 c). The lines have a slope of $1/v_g$ calculated from the unperturbed band diagram of corresponding mode.

measurement at a fixed temperature. These two measures are in good agreement, hence validating the model used (Eq. 4.4) to calculate the angular shift and the PhC sensitivity to refractive index change.

Using this optical setup, if we are capable to distinguish small angular shifts $\boldsymbol{\Delta}\theta$, then we obtain a temperature sensor capable to measure a thousandth of a degree temperature change.

## Discussion

In this measurements, the optical properties of the diamond PhC were analyzed using a white light source and a spectrometer. This configuration allowed us to understand the global optical characteristics of the photonic crystals and to compare them with the theoretical assumptions.

From the results of temperature measurements, we cannot link a temperature variation to a diamond refractive index change because multiple phenomena take place. The dominant event that occurs is probably the desorption phenomenon at the diamond PhC surface of the sample, fact that induces a blue shift.

In order to estimate the sensitivity in degree per RIU of the fabricated PhC to refractive index changes of the surrounding environment only, a FDTD simulation can be performed to relate the frequency shift measured for a 5 °C temperature elevation to the corresponding refractive index change of the bulk environment above the PhC. For the slowest mode, the measured frequency shift is , $\Delta\omega/\omega = 1.56 \times 10^{-4}$, due to an increase of 5°C has been evaluated to correspond to a variation of $2 \times 10^{-3}$ RIU in the surrounding environment and we deduce a sensitivity of 500°/RIU. This sensitivity is one order of magnitude higher than the one achieved by PhC based sensors [34, 33, 115] and similar to that achieved by best SPR sensors [35, 36]. As we measured group velocity much smaller than $c/100$ for some modes, we believe that sensitivities higher than 5000 °/RIU can be obtained and measured for PhCs with a higher quality factors.

In the next part, I will describe the final setup for measuring the sensitivity values of the fabricated biosensor.

## 4.3.2 Setup for sensitivity measurements

The aim of the biosensor is to offer an easy method to detect small refractive index variation in the closeness of the device. The experiment setup for sensitivity measurements includes light injection from a single frequency laser, in the visible regime, and the detection by means of a camera. The incoming light coupling with the targeted mode experiencing a low group velocity requires a precise fabrication process (hole diameters, diamond film thickness etc) in order to find the targeted GMR at that specific energy. Nevertheless, the possibility of slightly tuning in energy the slow mode to have a match with the laser by changing the azimuthal angle, represents an important characteristic of the proposed design. The preliminary measurements presented are necessary to detect the dispersion relations of the fabricated structure, to verify that the targeted GMR is found at the desired frequency. Another strategy involved to slightly modify the frequency of the targeted leaky mode is to realize multiple PhC structures and slightly vary the period size (typically between 5 and 10%). In such a way, the frequency of the mode can be lowered or increased at will, but requires the fabrication of many useless PhCs. A third option represents a post-processing step by exposing the sample to a light $O_2$ plasma in order to slightly increase the frequency of the targeted GMR. Using the three options to control the frequency of resonant mode, in particular the first one, the design is versatile regarding the positioning of the low group velocity mode at a desired frequency.

Furthermore, diamond does not absorb in the visible range as silicon does, an important advantage over the other proposed devices.

In Fig. 4.15 a) is shown the experimental setup conceived for sensitivity measurements of the device and in the Fig. 4.15 b) is represented the corresponding schematic of the optical setup.

The light is injected from a laser source from one side of the setup angularly dispersed and the reflected light is detected by means of a camera working in visible regime. In terms of laser source, the laboratory dispose of two single frequency lasers in the visible regime (one at 760 nm and the second one at 795 nm). Both lasers are commercially available at relative low prices, offering a single spectral and spatial mode with a circular beam profile. The lasers also offers a stable polarization, low operating current, high efficiency and a spectral stability.

In the opposite side of the setup is placed the detecting camera. It is a commercial available camera at low price, for visible light detection. The camera resolution is 2448×2048 pixels, with a pixel size of 3.5 µm. By placing the camera at 100 mm distance from the sample, we can expect to detect $\Delta\theta = \pm 2.5°$ from the central position, one pixel representing 0.002°. In practice, one can detect less than 0.2 pixel shift, thus the resolution (R) will be $4 \times 10^{-4}\,°$. In literature, similar setups give at least 0.001°. The limit of detection (LOD) is calculated by multiplying the resolution (R) with the sensitivity (S). For a sensitivity of $10^{3}\,°$/RIU, the LOD will be $4 \times 10^{-7}$.

The stage allows manual rotational and displacement movements in (x, y) plane. It will be used to change the azimuthal angle $\phi$ and to target a specific PhC on the sample, respectively. The data registered from the dispersion relations measurements give us all the information needed to optically characterize the fabricated PhC diamond structures, such

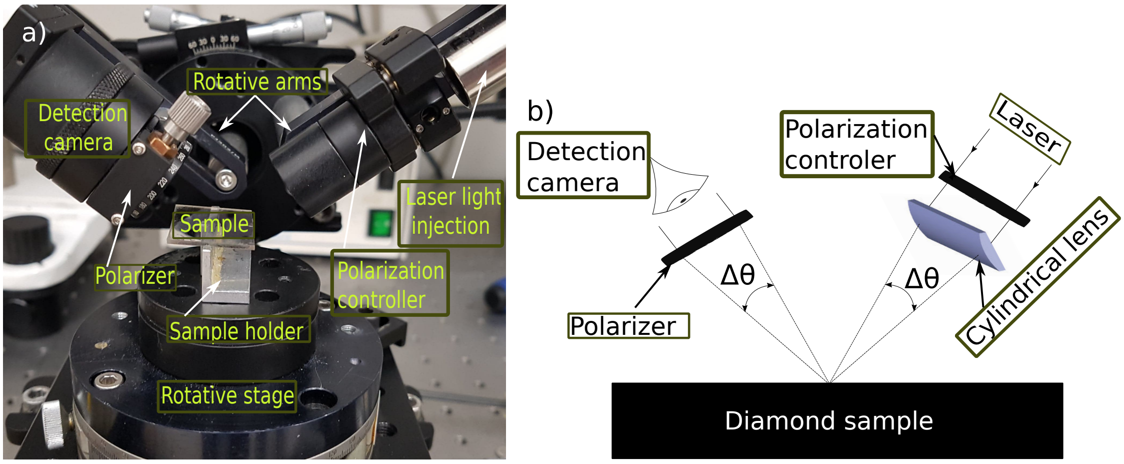

Figure 4.15: b) Side view image of the optical characterization setup for sensitivity measurements of the fabricated photonic crystals structures; b) Schematic representation of the corresponding optical setup

as the incident / detection angles, azimuthal angle direction for low group velocity GMR. The measurements will be performed in cross-polarization configuration, where the light is s polarized, as an example, and the reflected light will be detected for the p polarization.

Due to multiple delays encountered during this PhD thesis, the setup for sensitivity measurements was not optimized in time to measure the fabricated samples, the first measurement being done while finishing the writing of this manuscript. Using this setup we expect to validate the assumptions for the sensitivity values that can be detected for our proposed designs.

## 4.4 Limits and perspectives (gas detection, test molecules detection)

The further step after the setup optimization is to perform detection experiments. For that, two configurations are considered : the first one aim for gas detection and the second one for detection in the liquid environment. The firsts intended tests will be calibration experiments, where known amounts of gas / test molecules will be introduced for detection. In the case of gas detection, the setup needs to be in a closed environment, where the gas concentration is precisely known. For the detection in liquid phase, the sample will be encapsulated in a transparent microfluidic chamber, from where the liquids are injected to the PhC structures. Prior to the gas / liquid phase detection, the diamond surface will be functionalized accordingly for detection of targets. Several diamond functionalization protocols were optimized in our group ([63, 116, 117]) for pentane and hexanol gas detection, whereas for liquid phase detection, test molecule such as biotin / avidin are available.

The second type of proposed designs is the diamond film on quartz substrate. The advantage of this sample configuration is that the sensitivity measurements can be performed as in the case of silicon samples or the light injection can be done from the backside of the sample, case where the optical setup needs to be changed. The light interrogation from the backside of the sample offers an important improvement for liquid phase detection, leaving the top part of the diamond sample only for detection purposes.

## 4.5 Conclusion

This Chapter describes the optical characterization of the diamond photonic crystal structures for bio-detection. In the first part, the dispersion relations of the fabricated samples were measured for a large range of incident angles. Measurements were performed on two different types of sample configuration, namely polycrystalline diamond film transferred to a new silicon substrate and polycrystalline diamond film grown directly on quartz substrate. For the PhC structures realized on silicon substrate samples, the reflectivity spectrum detected Fano-shape features related to the diamond PhC structures, superimposed over Fabry-Perot interferences related to silica and silicon under the diamond film. In the case of diamond PhC realized on quartz samples, the Fano-shape features were related to the coupled diamond GMRs superimposed over a slowly varying background, related to the light source and spectrometer. The results show a good agreement with the numerical simulations.

The hypothesis for slowing light propagation for one targeted GMR was validated by changing the interrogation direction on the PhC. It was observed that the targeted GMR is experiencing low group velocity over a large range of azimuthal angles, from 20° to 30° from the $\Gamma$ X direction. The fabricated PhC in polycrystalline diamond experience a group velocity below $c/100$ for certain injection direction. An important characteristic of the proposed design is the energy tuning of the desired GMR of more than 5%, property that will be useful for the sensitivity measurements, where the light is injected at a fixed frequency. Various polarization configurations were tested and for each case the influence on the GMRs detection has been shown.

If angle shift measurements are done at a fixed frequency, we have shown that the angular sensitivity is inversely proportional to the group velocity of the GMR. Measurements at different temperatures caused an angle shift in the coupling of the targeted GMR with the incoming light. We demonstrated an increase of the sensitivity proportional to the group velocity and inferred an angular sensitivity of the sensor equal to 500°/RIU, i.e. one order of magnitude higher than previously reported PhC based sensors.

These results represent a first step toward a more involved highly sensitive biosensor, including surface functionalization of the diamond surface for specific target recognition.

# General conclusion

The use of photonic crystals as transducers for optical label-free biosensors offers the possibility of fabricating structures with high quality factors and small modal volume and therefore, an improved light and matter interactions, desirable properties for biosensors. Diamond represents a reliable candidate as transducer material, due to its physico-chemical properties desired for biosensing : its transparency from the UV until IR, its biocompatibility, its possibility for surface functionalization with probes by covalent bonds, offering a stable interface, and the possibility to realize photonic crystal structures on the material. This PhD thesis propose innovative designs of photonic crystal for optical label-free sensing based on guided mode resonance detection at the limit of the visible wavelength range. In this context, the work was divided in three main axis, namely the conception of the proposed designs by numerical simulations, two dimensional photonic crystals fabrication onto polycrystalline diamond by micro-fabrication technologies and optical characterization of the fabricated polycrystalline diamond photonic crystal structures.

The state of the art of proposed technologies in the optical label-free biosensors field allow us to position the performances of the different types of PhC devices compared to the SPR method, which is the reference technology in this domain.

The proposed design rely in the interrogation of an in-plane guided mode resonance with an outside collimated light source, at a desired angle of incidence. This configuration simplifies the detection method, a spectrum analyzer is no longer needed. This proposed design wants to overpass the angular sensitivity values found in literature for this type of GMR sensors, which are around 60° / RIU for PhC sensors or 500° / RIU for SPR sensors.

It was shown that angular sensitivity for this kind of PhC sensors is proportional with the $^{1}/_{v_g}$, thus from here the interest of slowing the light propagation inside a desired GMR. At the same time, the quality factor of the targeted GMR needs to be controlled at high values, fact that is not achieved for standard PhC. For that, we gave some design rules for 2D PhC to achieve GMR with controlled values of quality factor and low group velocity, while maintaining a intense coupling in the reflectivity spectrum. Numerical simulations were performed to define the geometrical parameters of the 2D PhC structures in order to achieve the mentioned requirements. We optimized two types of designs : the first one based on a 2D PhC suspended in air and the second one based on 2D PhC in contact with a transparent substrate, namely quartz substrate. The estimated theoretical angular sensitivities can reach values up to 3100° / RIU, values that surpass the other reported values from the literature by an order of magnitude.

From the technological point of view, the PhD thesis work involved the growth of polycrystalline diamond films on two different substrates, namely silicon and quartz substrates. In the same time, optimization of the existing micro-fabrication methods and the development of new processes suitable for our designs were performed, in order to achieve high quality factor PhCs.

Polycrystalline diamond film was deposited by MPCVD process, with film thicknesses ranging from a few nanometers to several micrometers. In the case of polycrystalline film deposition on silicon substrate, classic growth conditions were applied, which promote a selective growth. In the case of polycrystalline diamond film deposition on quartz substrate, the growth conditions were changed to decrease the growth temperature, in order to prevent film cracking or delamination. As the film thickness increases, the surface roughness RMS increases as well, reaching up to 600 nm values, with peak-to-valley values of 1.2 µm. Surface roughness RMS decrease was tried directly during the growth process by applying growth conditions to a polycrystalline diamond film deposited with classical parameters. The modification of the morphology was done by changing the temperature of the deposition process. The surface roughness RMS was decreased, as observed by HRSEM, but unfortunately not enough to expect high quality factor PhC.

Due to the fact that the proposed biosensor is designed to detect at visible wavelengths, it implies that the fabricated structures needs to be smaller than the ones reported in our group for near infrared detection. To achieve the desired device, holes in the order of one hundred nanometers needs to be patterned onto polycrystalline diamond film, for a film thickness of around four hundred nanometers.

Polycrystalline diamond films, in order to be compatible with the electronic beam lithography technique for fabricating high quality factor PhCs, a surface planarization was required. Part of samples were processed with the recipes already in place for surface planarization, but unfortunately ICP machine had broken down during the PhD work. The transfer of the recipes onto a new dry etching system was required. In parallel, the deposition of the flowable oxide was improved, with the possibility of depositing a maximum thickness of 1.5 µm, thickness enabling the smoothing of the roughness RMS of 5 µm thick polycrystalline diamond film. By combining the flowable oxide deposition and dry etching process, the surface roughness RMS can be decreased at less than one nanometer, values confirmed by AFM measurements. This planarization protocol is general and valid for polycrystalline diamond deposited on different substrates (here tested on silicon and quartz substrates with similar results) and can be used beyond this work.

Insofar as we supposed that the presence of high percentage of grain boundaries for thin films limit the maximal quality factor that can be achieved with 2D PhC, the development of a transfer procedure onto a different substrate has been set up. By keeping only the top 400 nm part of an initial 5µm thick polycrystalline diamond film, the percentage of the grain boundaries was decreased several times. This procedure increases the diamond quality film and opens the way to new designs that require better crystalline quality. The procedure was optimized for film transfers onto silica layer with silicon as substrate, and for film transfer on quartz substrate. The results from previous works achieved a quality factor of 6500 for PhC structures for detecting at 1.55 µm with a polycrystalline diamond film of 400 nm. The fabrication of the same structures could confirm the interest of developing the transfer procedure for lowering the grain boundaries.

The film thinning from 5 µm to 400 nm was realized by a new developed dry etching method that etches isotropically the diamond film transferred to an insulating material.

At the same time, a new etching recipe was intended to change the diamond surface terminations by $CF_x$ groups, thus functionalizing the diamond surface. The recipe was performed on SAW biosensors in the frame of exterior collaborations. The devices were processed for a few seconds with the fluorinated based-plasma and the characterization results shown the surface change with $CF_x$ groups. This result is promising, further optimization protocols being needed.

The PhC fabrication on diamond films with different configurations was realized. Optimization of nitride mask and of dry etching processes allowed us to realize vertical holes in diamond, with an angle inferior of 3° for 120 to 340 nm holes diameter.

The firsts PhC structures were realized on polycrystalline diamond film deposited on quartz substrate. Due to the lack of time, we did not had time to fabricate all the desired configurations. Nevertheless, the first results showed satisfactory results.

From the optical characterization point of view, the novelty of the proposed design required the establishment in the laboratory of a new setup. The realized diamond PhC structures were optically characterized at first for a large range of incident angles. This reflectivity measurements allowed us to construct the band diagrams of the PhC structure. The results showed a good agreement with the numerical simulations.

The assumption of decreasing the group velocity for a targeted GMR when the light is injected at a specific direction was validated. It was observed that the targeted leaky mode was experiencing low group velocities as low as c/ 100, for a large range of interrogation directions. This fact represents an asset of the proposed design. At the same time, if the light injection direction is changed, the energy of the targeted GMR is also varied, with an energy tuning of more than 5% while keeping a small group velocity.

For the measurements at fixed frequency, the angular sensitivity was described as being proportional with $^1/_{v_g}$ of the GMR. By varying the environmental temperature, the refractive index of the diamond will vary, implicitly the frequency of the GMRs. Experiments at different temperatures induced angle shifts in the coupling of the targeted GMR with the incoming light. The results shown that for a low group velocity GMR of c / 80, a 5°C temperature variation induced an angular shift of 1°. Meanwhile, for higher group velocity modes, lower angular shifts were measured. The proportionality relation between the angular sensitivity and $^1/_{v_g}$ has been verified. We deduced, thanks to numerical simulations an angular sensitivity of 526° / RIU. This value represents an order of magnitude improvement compared to PhC sensors and similar values when compared to the best SPR sensors.

The results accomplished during this PhD thesis represents a step forward of the optical biosensors field : the innovative proposed design, micro-fabrication processes developed and also the proposed optical setups.

From the fabrication point of view, the further steps for short term can be the realization of all the proposed configurations during this PhD thesis. The optimization of 2D PhC fabrication on quartz substrates is required to achieve better quality factors. Realization of the same PhC structures on diamond film transferred onto new substrate and another one on a classical thin film as grown, will allow the validation of the transfer method.

From the optical characterization point of view, for the short term expectations, will be the validation of the expected angular sensitivity values with the variation of the refractive index of the surrounding of the PhC for example by varying the gas composition instead of air. The first measurements with the optical setup with a single frequency light source and a camera as detector are obtained. A further step include the diamond surface simple functionalization with test molecules and the measurement of the angular sensitivity induced. After the device validation, the detection of real biological targets will be desired.

The configuration with diamond film on quartz substrate offers the possibility of light injection and detection from the backside of the sample, with the top surface, where the diamond is placed, only for bio-detection purposes. The optical setup realization is expected for mid term period, with similar strategy for angular sensitivity validation.

Also for the mid term period experiences, the realization of new PhC samples with the designs arranged in such a way to perform the detection on multiple PhC structures simultaneously. At the same time, different diamond surface functionalization for each PhC structure to be realized in order to detect different molecules or even further, to detect different conformations of the same molecule.

For the long term period, the proposal of a compact portable device disposing with an user friendly interface, an easy readable result and a simple sample manipulation can be considered.

# Résumé

Lors de ces dernières années, on a pu assister à des progrès technologiques en fabrication et à une meilleure compréhension des phénomènes physiques de confinement de la lumière et de son interaction avec la matière. Ceux-ci ont permis l'amélioration des performances des bio-capteurs optiques, avec la possibilité de les intégrer dans des systèmes compacts et portables. Les bio-capteurs optiques sans marquage offrent une détection directe du signal liée à une reconnaissance moléculaire entre une molécule cible et une molécule sonde. La procédure de détection est simplifiée par rapport à la détection avec marquage, où il y a besoin d'étiqueter la molécule cible, par exemple avec une molécule fluorescente. Le principe de fonctionnement d'un bio-capteur optique est basé sur un changement d'une propriété de la lumière, comme, par exemple, la fréquence de résonance d'un mode optique lors de la reconnaissance de molécules cibles. Typiquement, on détecte un changement d'indice de réfraction du - milieu extérieur au capteur grâce à l'interaction des molécules avec la partie évanescente du champ d'un mode optique du bio-capteur. Parmi toutes les méthodes proposées, les cristaux photoniques bi-dimensionnels (CPh) offrent une alternative intéressante aux technologies déjà existantes. Les propriétés optiques des CPh ont conduit au développement de nouveaux dispositifs dans des domaines comme les télécommunications et l'optoélectronique et plus récemment, la bio-détection. Les CPh offrent la possibilité de fabriquer des structures avec de forts facteurs de qualité (Q), de volumes modaux petits et, en conséquence, des interactions lumière - matière renforcées, propriétés désirables pour atteindre des sensibilités élevées et des dispositifs compacts. Typiquement, les capteurs à cristaux photoniques sont basés sur la mesure des modes confinés à fort facteur de qualité d'une micro-cavité résonante, avec des valeurs typiques de sensibilité d'environ 700 nm par unité d'indice de réfraction (nm/RIU). Les inconvénients de cette approche sont l'injection et la collection de la lumière, qui nécessitent des éléments de mesure spécifiques, avec un alignement précis; et la difficulté d'amener les molécules cibles uniquement dans la cavité. Les capteurs à CPh peuvent également reposer sur les modes résonants rayonnants et faiblement guidés dans le plan du CPh, nommés résonances de mode guidé (RMG). Cette approche permet un couplage facile de l'extérieur avec une lumière collimatée, souvent en incidence normale. Un deuxième avantage est la fonctionnalisation plus facile, car la surface

de CPh est plus grande par rapport à celle d'une cavité. L'inconvénient est que les valeurs de sensibilité reportées dans la littérature sont dix fois plus faibles que celles des cavités à CPh. A l'heure actuelle, la majorité des composants photoniques sont basés sur les technologies du silicium ou des semi-conducteurs III-V. Les matériaux utilisés comme transducteurs sont importants dans la structure d'un capteur, puisque l'efficacité d'immobilisation des molécules sondes sur la surface et la compatibilité avec la biochimie vont être décisives pour les performances finales. Durant cette thèse, nous avons choisi d'utiliser du diamant polycristallin car il permet une fonctionnalisation simple, rapide, robuste et efficace en milieu aqueux. La combinaison des propriétés optiques des cristaux photoniques et les propriétés de fonctionnalisation du diamant permettront de réaliser des capteurs à cristaux photoniques très sensibles, sélectifs et spécifiques.

Le deuxième chapitre présente la conception et la modélisation de la structure à cristaux photoniques pour maximiser les performances du capteur, notamment la sensibilité. Comme indiqué précédemment, on est intéressé par la détection d'un RMG, avec une injection angulaire d'une lumière collimatée. Pour repérer cette incidence, on a deux angles : $\theta$ par rapport à l'incidence normale et $\phi$ par rapport à la maille de cristal. Le couplage entre le mode guidé du CPh et une lumière incidente d'une fréquence donnée va avoir lieu pour un vecteur d'onde particulier. Ce vecteur d'onde correspond à un angle de couplage particulier dans le spectre en réflexion, avec l'apparition d'une résonance spécifique, qui prend la forme d'une résonance de Fano. Lorsqu'une reconnaissance moléculaire va avoir lieu à la surface du CPh, l'indice de réfraction va être augmenté légèrement, ce qui va correspondre à une diminution de la fréquence du RMG. Le couplage avec la lumière de l'extérieur à la même fréquence donnée va avoir lieu avec un vecteur d'onde différent, ce qui implique un changement de l'angle de couplage dans le spectre en réflexion. Le décalage en vecteur d'onde et, donc, en angle de couplage va être augmenté dans le cas où la pente du mode est plus douce, ce qui correspond à une vitesse de groupe ($v_g$) plus faible. Nous avons montré pendant cette thèse pour une configuration avec une injection de la lumière non-normale que la sensibilité est proportionnelle avec ${}^{1}\!/_{(v_g \cos\theta)}$. On a donc intérêt à travailler avec de grands angles d'incidence $\theta$, mais en pratique on est limité par la taille du spot sur le CPh. Le facteur qui peut être modifié pour avoir des sensibilités très élevée est la vitesse de groupe. Elle va nous permettre d'avoir de sensibilités record pour ce type d'approche. Généralement, on trouve des modes avec une vitesse de groupe très faible pour des vecteurs d'onde particuliers à une fréquence bien déterminée, qui correspond à des points de haute symétrie dans la zone de Brillouin de CPh. Nous proposons une approche innovante pour ralentir la lumière d'un mode choisi (réduire sa vitesse de groupe) pour une large plage de vecteurs d'onde et angles de couplage $\theta$. Des simulations numériques ont été effectuées pour déterminer les diagrammes de bandes, selon les directions de haute symétrie du CPh.

Les courbes de dispersion ont été calculées pour une géométrie composée d'un arrangement carré de trous d'air circulaires, avec un trou dans la maille fondamentale. On remarque qu'il existe des modes qui ont la même fréquence pour deux vecteurs d'onde particuliers : le premier au centre de la zone de Brillouin (point Γ) et le deuxième à un vecteur d'onde particulier entre les points de haute symétrie à la limite de la zone de Brillouin (points X et M). En raison de la continuité de la courbe de dispersion du mode et du fait que les extrémités du mode ont la même fréquence, la vitesse de groupe doit s'annuler pour un vecteur d'onde $k$ dans cette direction particulière. Le calcul de diagramme de bandes pour le CPh proposé, lorsqu'il a été interrogé en cette direction particulière, valide l'hypothèse de diminuer la vitesse de groupe pour le RMG désiré. Ces modes se trouvent au-dessus du cône de lumière, et offrent, en général, pour des modes radiatifs des facteurs de qualités (Q) assez faibles, donc un mauvais contraste et des résonances angulairement larges dans le spectre en réflexion. Une méthode pour atteindre des Q élevés pour les RMG désirés consiste à effectuer un repliement du diagramme de bande du CPh pour amener au-dessus du cône de lumière des modes qui se trouvent initialement sous le cône de lumière. Une possibilité consiste à imposer une deuxième période du CPh et ainsi des vrais modes guidés du CPh deviendraient des RMG accessibles avec la possibilité d'une interrogation hors du plan. Si l'on considère le cas dequatre trous de la même taille dans la maille fondamentale, on a des modes avec des Q quasiment infinis, et quasiment sans couplage avec la lumière extérieure. En changeant la taille d'un trou parmi les quatre, le facteur de qualité peut être diminué et contrôlé avec précision, en augmentant le couplage avec la lumière de l'extérieur. En augmentant la différence entre la taille de trous dans la maille fondamentale, on diminue le Q du mode désiré à une valeur souhaitée. Du point de vue de la fabrication, la réalisation de forts Q en diamant polycristallin est difficile puisque l'absorption résiduelle du matériau et les imperfections de fabrication peuvent réduire considérablement la valeur voulue. Dans ce cas-là, afin d'avoir une forte intensité dans le spectre en réflexion, il est souhaitable de concevoir une structure avec une valeur Q qui est proche de la valeur attendue en fabrication avec les pertes extrinsèques afin d'approcher le couplage critique avec la lumière entrante. Les valeurs de Q reportées sur diamant polycristallin pour la détection dans le proche-infrarouge sont de 6500 à λ =1550 nm ([63]). Les designs proposés ont un facteur de qualité pour le RMG entre 1000 et 5000, compte tenu du fait que les pertes sont plus élevées à une longueur d'onde de 800 nm qu'à 1500 nm.

Un point fort de la structure proposée est qu'en changeant la direction d'injection de la lumière $\phi$ de quelques degrés, on peut toujours trouver un mode dont la vitesse de groupe s'annule. Cette annulation est obtenue à différentes fréquences et à différents angles d'incidence $\theta$ quand on change la direction $\phi$. Cette propriété est importante pour la détection à une fréquence donnée. Une fois le PhC réalisé, on peut changer la fréquence à laquelle on va avoir l'annulation, avec la possibilité de varier d'environ 5% la fréquence du mode désiré.

Une fois la géométrie du CPh établie pour avoir une vitesse de groupe faible et un Q contrôlé, les performances du capteur proposé peuvent être déduites. En appliquant la formule spécifique de sensibilité, on trouve pour un RMG avec $v_g = 0.25$ une sensibilité de 62° /RIU (degrés par unité d'indice de réfraction). Cette valeur est similaire avec des valeurs reportées dans la littérature pour le même type d'approche. Si on regarde un RMG avec $v_g = 0.003$, on obtient une valeur de sensibilité de 3100° /RIU, valeur qui est cent fois plus grande que les autres RMG dans la littérature et dix fois plus grande que les résonateurs à plasmons de surface.

Avec des valeurs théoriques extraordinaires en terme de sensibilité obtenues pour le capteur proposé, dans le chapitre trois est présenté le travail sur la fabrication des cristaux photoniques en diamant. Les structures simulées ont été fabriquées dans la salle blanche du C2N-Orsay. Les films de diamant polycristallin ont été déposés sur deux substrats différents : silicium et quartz. Dans les deux cas, la croissance des films de diamant polycristallin est bien connue par l'équipe du Laboratoire Capteurs Diamant (LCD) du CEA. Le diamant polycristallin a été préféré au diamant monocristallin puisqu'il est possible de faire croître des films de diamant polycristallin sur des grandes surfaces (de 2 pouces dans notre cas), avec un coût relativement bas et avec des épaisseurs allant de quelques centaines de nanomètres à quelques micromètres. Après la croissance du film de diamant polycristallin, la rugosité du film est trop importante pour pouvoir réaliser des CPh pour la détection à 800 nm (diamètre des trous d'environ 120 nm). Pour une épaisseur de 470 nm, la rugosité RMS est estimée à 40 nm, avec un pic à pic de plus de 100 nm, et dans le cas d'un film avec une épaisseur du 5 µm, une rugosité de 600 nm et un pic à pic de plus de 1.2 µm. Cette rugosité est liée au fait que la croissance est sélective en direction et sensible à la morphologie des grains du diamant. Une première méthode pour réduire la rugosité RMS a été employée directement lors de la croissance du film en changeant les paramètres de croissance pour ouvrir les faces (100). Malgré une réduction importante de la rugosité, les valeurs obtenues ne sont pas suffisantes pour nos besoins. De plus, on a rencontré un problème de délamination du film de diamant du substrat. En conséquence, j'ai cherché une autre voie pour diminuer la rugosité de surface. Un procédé de lissage a été développé précédemment dans l'équipe C2N, consistant en un transfert de la planéité d'une couche lisse en silice liquide (HSQ) recouvrant le diamant en utilisant des méthodes de gravure plasma à induction couplée (ICP)([114, 84]). J'ai optimisé ce procédé afin de pouvoir travailler avec des films de diamant plus épais, donc des rugosités plus importantes. J'ai optimisé le procédé de dépôt et de recuit de la résine HSQ (deux fois plus épais qu'avant cette thèse $\sim$ 1.5 µm) et une nouvelle recette de gravure ICP sur une autre machine de gravure. Les valeurs des rugosités RMS ont été mesurées au microscope à force atomique (AFM) sur des surfaces 10x10µm$^2$. Pour un film d'une épaisseur initiale de $\sim$ 500 nm, la rugosité RMS est de 0.45 nm, et pour un film d'une épaisseur initiale de $\sim$ 5µm, la rugosité RMS est de 2.8 nm. Ces valeurs sont similaires avec des valeurs de rugosité d'autres matériaux, ce qui nous permet désormais d'utiliser des techniques standard de fabrication des cristaux photoniques sur cette surface de diamant. Pour améliorer la qualité cristalline du diamant polycristallin et obtenir des Q plus élevés, on a intérêt à faire croître des couches de diamant plus épaisses. À la surface d'une couche de 5 µm d'épaisseur, on a beaucoup moins de joints de grains par rapport à une couche de diamant de 500 nm. Pour la réalisation de notre structure photonique, selon les simulations numériques, on a besoin d'une couche de diamant de 400 nm. Pour pouvoir utiliser la partie haute d'un film de 5 µm, j'ai développé une méthode de collage avec un autre substrat. Avec une recette de gravure ICP, j'ai retiré le substrat initial de silicium. Les petits grains se trouvent ainsi en partie haute de l'échantillon. Avec une nouvelle recette ICP développée, j'ai réussi à amincir des couches de diamant polycristallin de 5 µm jusqu'à 400 nm sans ajouter des défauts de gravure. Les films de diamant sont plus uniformes qu'un film de 400 nm après la croissance directe, avec de meilleures propriétés optiques.

La réalisation des structures photoniques sur le film diamant polycristallin, reporté sur un autre substrat ou non, est ensuite effectuée. A cause d'un changement de machine de gravure ICP (l'ancienne machine était tombée en panne), les épaisseurs des couches de résine électronique et des masques de nitrure, ainsi que les recettes de gravure ont été optimisées. Les CPhs conçus font 200x200 µm$^2$, avec des trous de diamètre d'environ 120nm. La verticalité des trous gravés dans la couche de diamant est inférieure à trois degré, valeur qui est à l'état de l'art sur le diamant. En conclusion, j'ai réussi a réaliser des CPh sur une couche de diamant sur un substrat de silicium.

Une deuxième approche a été élaborée pendant cette thèse sur substrat de quartz. Un des avantages de cette configuration est que le film de diamant n'est pas complètement gravé, ce qui donne une fonctionalisation plus uniforme en surface (les molécules vont être en contact seulement avec le diamant). Un deuxième avantage est la possibilité d'injecter la lumière par la face arrière de l'échantillon, en laissant la partie où se trouve le diamant pour la fonctionalisation bio-chimique. Les premières structures photoniques ont été réalisées sur une couche de diamant sur quartz. La difficulté rencontrée est que le substrat (quartz) est isolant, ce qui rend la lithographie électronique plus compliquée. Une première optimisation a été faite en utilisant une résine conductrice pour limiter les effets de charge en surface. En conclusion, les premières structures photoniques en diamant sur quartz ont été réalisées.

Le dernier chapitre se focalise sur la caractérisation expérimentale des structures fabriquées. Les échantillons dans les différentes configurations proposées ont été mesurés avec un système de détection composé de deux bras synchronisés, qui permettent de changer l'angle d'incidence et de détection de la lumière (angle $\theta$), et une platine, pour changer la direction d'injection par rapport au CPh (angle $\phi$). Sur les deux bras se trouvent des fibres optiques qui guident la lumière, des collimateurs et des polariseurs. D'une côté est injecté la lumière depuis une source blanche de lumière (360-2600 nm) et dans la partie opposé se trouve le spectromètre (500-1000 nm).

Les mesures optiques ont été faites pour une configuration de CPh comportant une couche de diamant transféré sur un substrat de silicium avec une couche intermédiare de silice; et une deuxième configuration avec la couche de diamant sur substrat de quartz.

Pour la première configuration mentionnée, le spectre de réflectivité pour un angle $\theta$ d'incidence est composé en larges interférences Fabry-Perot liées à la couche de silice en dessous de diamant, et de petites diminutions locales en intensité qui sont liées à des modes de CPh. La mesure des spectres pour une large plage d'angles d'incidence $\theta$ (20 - 80°) rend possible l'obtention du diagramme de bandes de CPh pour une direction donnée du cristal. Avec un filtrage numérique post-mesure, on peut supprimer ces interférences Fabry-Perot, où on peut utiliser un filtre pour exalter des modes de PhC et avoir un meilleur contraste.

Le changement de la direction de la lumière selon un angle $\phi$ particulier diminue la vitesse de groupe pour un mode particulier. Le diagramme de bandes mesuré selon cette direction particulière correspond à la simulation numérique pour cette structure mesurée. Si on varie la direction d'injection de la lumière selon différents angles $\phi$, on obtient des vitesses de groupe faibles pour différents angles d'incidence $\theta$ et aussi avec la variation en fréquence du mode du CPh, comme indiqué par la théorie.

La validation de l'hypothèse de changement la direction $\phi$ pour réduire la vitesse de groupe a été faite aussi pour la configuration avec la couche de diamant sur quartz, avec des trous pas complètement gravés dans le diamant. Dans ce cas-là, il n'y a pas des inferferences Fabry-Perot. Dans le spectre en réflection on mesure seulement les modes du CPh.

Le but de cette thèse est de faire un capteur sensible à de faibles changements d'indice de réfraction. Un moyen simple de faire varier l'indice est le changement en température. Avec ces mesures, la formule de sensibilité proposée peut être validée.

Le décalage angulaire a été suivi pour des modes avec différentes vitesses de groupe. On a observé que pour une vitesse de groupe rapide (c/12), pour une variation de 60°C on obtient un décalage angulaire de 0.8°. Pour un mode plus lent (c/80), pour une changement de 5°C en température, on a un décalage angulaire de 2.5°.

La formule théorique de sensibilité donne une relation entre le $\Delta\theta$ en fonction de ${}^{\Delta\omega}/_{\omega\cos\theta}$. Cette relation est une relation linéaire avec un coefficient proportionnel à $1/v_g$ vérifiée expérimentalement et validant ainsi la formule théoriquede sensibilité proposée durant cette thèse.

En termes de performances pour le capteur fabriqué, avec l'aide de simulations FDTD on peut relier le changement en température à un changement d'indice de réfraction autour de CPh. On trouve pour le mode lent (c/80) une valeur de sensibilité d'environ 500°/RIU. Cette valeur est 10 fois meilleure que celle des autres cristaux photoniques basés sur les résonances de modes guidés. Cette valeur est proche de celle de capteurs à plasmons de surface. C'est une valeur préliminaire, qui peut être amélioré en optimisant des procédés de fabrication et en changeant le système de détection. Une deuxième configuration pour la mesure optique des échantillons est en cours de validation, où la source de lumière injectée est monochromatique et le détecteur est une caméra. C'est un système de détection plus simple (il n'y a pas besoin de spectromètre) pour se rapprocher d'un bio-capteur avec une méthode de mesure plus pratique.

Les résultats obtenus pendant cette thèse de doctorat represent un avancement dans le domaine des capteurs optiques sans marquage. On a proposé un nouveau concept de capteur bassé sur la détection du RMG. Le design a été réalisé et des mesures optiques valident la travail théorique.

Les prochaines étapes sont, d'un point de vue fabrication, la réalisation de toutes les configurations proposées pendant cette thèse. Ensuite, la validation du capteur proposé pour de vrais molécules biologiques est envisagée, avec la possibilité de faire de multiples détections simultanément.

# Bibliography

[1] Nikhil Bhalla, Pawan Jolly, Nello Formisano, and Pedro Estrela. Introduction to biosensors. *Essays in biochemistry*, 60(1):1–8, June 2016.

[2] Jose Juan Colas. *Dual-Mode Electro-photonic Silicon Biosensors: Recognizing Outstanding Ph.D. Research*, volume 1 of *Springer Theses*. Springer, 2017 edition, 2017.

[3] Amir Syahir, Kenji Usui, Kin-ya Tomizaki, Kotaro Kajikawa, and Hisakazu Mihara. Label and label-free detection techniques for protein microarrays. *Microarrays*, 4(2):228–244, 2015.

[4] Zongfu Yu and Shanhui Fan. Extraordinarily high spectral sensitivity in refractive index sensors using multiple optical modes. *Opt. Express*, 19(11):10029–10040, May 2011.

[5] Pavel Damborsky, Juraj Svitel, and Jaroslav Katrlik. Optical biosensors. *Essays Biochem*, 60(1):91, June 2016.

[6] D. Dey and T. Goswami. Optical biosensors: A revolution towards quantum nanoscale electronics device fabrication, 2011.

[7] Frank Vollmer and Lan Yang. Label-free detection with high-q microcavities: a review of biosensing mechanisms for integrated devices. *Nanophotonics*, 1(3-4):267–291, December 2012.

[8] Enxiao Luan, Hossam Shoman, Daniel M. Ratner, Karen C. Cheung, and Lukas Chrostowski. Silicon photonic biosensors using label-free detection. *Sensors*, 18(10), 2018.

[9] Giuliano Zanchetta, Roberta Lanfranco, Fabio Giavazzi, Tommaso Bellini, and Marco Buscaglia. Emerging applications of label-free optical biosensors. *Nanophotonics*, 6, 01 2017.

[10] Eli Yablonovitch. Inhibited spontaneous emission in solid-state physics and electronics. *Phys. Rev. Lett.*, 58(20):2059–2062, May 1987.

[11] John D. Joannopoulos Steven G. Johnson Joshua N. Winn Robert D. Meade. *Photonic Crystals Molding the Flow of Light.* Princeton University Press Princeton and Oxford, 2008.

[12] Jean-Michel Lourtioz, Henri Benisty, Jean-Michel Gérard, Daniel Maystre, and Alexei Chelnokov. *Photonic crystals, towards nanoscale photonic devices (second edition).* Springer-Verlag Berlin Heidelberg, 01 2008.

[13] Ming-Chieh Lin and Ruei-Fu Jao. Finite element analysis of photon density of states for two-dimensional photonic crystals with in-plane light propagation. *Opt. Express*, 15(1):207–218, Jan 2007.

[14] Giampaolo Pitruzzello and Thomas F Krauss. Photonic crystal resonances for sensing and imaging. *Journal of Optics*, 20(7):073004, 2018.

[15] Hoang Hiep Nguyen, Jeho Park, Sebyung Kang, and Moonil Kim. Surface plasmon resonance: A versatile technique for biosensor applications. *Sensors*, 15(5):10481–10510, 2015.

[16] Ya nan Zhang, Yong Zhao, and Ri qing Lv. A review for optical sensors based on photonic crystal cavities. *Sensors and Actuators A: Physical*, 233:374 – 389, 2015.

[17] Christoph Fenzl, Thomas Hirsch, and Otto S. Wolfbeis. Photonic crystals for chemical sensing and biosensing. *Angewandte Chemie International Edition*, 53(13):3318–3335, 2014.

[18] Yildiz Uludag and Ibtisam E. Tothill. Cancer biomarker detection in serum samples using surface plasmon resonance and quartz crystal microbalance sensors with nanoparticle signal amplification. *Analytical Chemistry*, 84(14):5898–5904, 2012. PMID: 22681722.

[19] A. K. Sharma, R. Jha, and B. D. Gupta. Fiber-optic sensors based on surface plasmon resonance: A comprehensive review. *IEEE Sensors Journal*, 2007.

[20] BIACORE. Biacore. Technical report, www.biacore.com, 2018.

[21] M. Notomi. Strong light confinement with periodicity. *Proceedings of the IEEE*, 2011.

[22] E. Chow, A. Grot, L. W. Mirkarimi, M. Sigalas, and G. Girolami. Ultracompact biochemical sensor built with two-dimensional photonic crystal microcavity. *Opt. Lett.*, 29(10):1093–1095, May 2004.

[23] A. Di Falco, L. O'Faolain, and T. F. Krauss. Chemical sensing in slotted photonic crystal heterostructure cavities. *Applied Physics Letters*, 94(6):063503, 2009.

[24] V. Toccafondo, J. García-Rupérez, M. J. Ba nuls, A. Griol, J. G. Castelló, S. Peransi-Llopis, and A. Maquieira. Single-strand dna detection using a planar photonic-crystal-waveguide-based sensor. *Opt. Lett.*, 35(21):3673–3675, Nov 2010.

[25] Xinyuan Chong, Le Liu, Zhiyi Liu, Suihua Ma, Jun Guo, Yanhong Ji, and Yonghong He. Detect the hybridization of single-stranded dna by parallel scan spectral surface plasmon resonance imaging. *Plasmonics*, 8(2):1185–1191, Jun 2013.

[26] V. N. Konopsky. www.pcbiosensors.com. Technical report, 2018.

[27] S. S. Wang and R. Magnusson. Theory and applications of guided-mode resonance filters. *Appl. Opt.*, 32(14):2606–2613, May 1993.

[28] Brian Cunningham, Peter Li, Bo Lin, and Jane Pepper. Colorimetric resonant reflection as a direct biochemical assay technique. *Sensors and Actuators B: Chemical*, 81(2):316 – 328, 2002.

[29] Mohamed El Beheiry, Victor Liu, Shanhui Fan, and Ofer Levi. Sensitivity enhancement in photonic crystal slab biosensors. *Opt. Express*, 18(22):22702–22714, Oct 2010.

[30] Min Huang, Ahmet Ali Yanik, Tsung-Yao Chang, and Hatice Altug. Sub-wavelength nanofluidics in photonic crystal sensors. *Opt. Express*, 17(26):24224–24233, Dec 2009.

[31] Robert Magnusson, Debra Wawro, Shelby Zimmerman, and Yiwu Ding. Resonant photonic biosensors with polarization-based multiparametric discrimination in each channel. *Sensors*, 11(2):1476–1488, 2011.

[32] Bo Lin, Jean Qiu, John Gerstenmeier, Peter Li, Homer Pien, Jane Pepper, and Brian Cunningham. A label-free optical technique for detecting small molecule interactions. *Biosensors and Bioelectronics*, 17(9):827 – 834, 2002.

[33] Elewout Hallynck and Peter Bienstman. Photonic crystal biosensor based on angular spectrum analysis. *OPTICS EXPRESS*, 18(17):18164–18170, AUG 16 2010.

[34] Valery N. Konopsky and Elena V. Alieva. Photonic crystal surface waves for optical biosensors. *Analytical Chemistry*, 79(12):4729–4735, 2007. PMID: 17497829.

[35] Changkui Hu. Surface plasmon resonance sensor based on diffraction grating with high sensitivity and high resolution. *OPTIK*, 122(21):1881–1884, 2011.

[36] Xiaoliang Sun, Xuewen Shu, and Changhong Chen. Grating surface plasmon resonance sensor: angular sensitivity, metal oxidization effect of al-based device in optimal structure. *Appl. Opt.*, 54(6):1548–1554, Feb 2015.

[37] I. Roland, Y. Zeng, Z. Han, X. Checoury, C. Blin, M. El Kurdi, A. Ghrib, S. Sauvage, B. Gayral, C. Brimont, T. Guillet, F. Semond, and P. Boucaud. Near-infrared gallium nitride two-dimensional photonic crystal platform on silicon. *Applied Physics Letters*, 105(1):011104, 2014.

[38] Cheng Qian, Yinghui Wang, Yunfei Song, Lu Zou, Yuguang Ma, Yanqiang Yang, and Hanzhuang Zhang. Modulation of spontaneous emission characteristics of alq3 in three-dimensional pmma photonic crystals. *Journal of Polymer Science Part B: Polymer Physics*, 52(12):842–847, 2014.

[39] W. J. Bock G. Xiao, editor. *Photonic Sensing : Principles and Applications for Safety and Security Monitoring.* Wiley, 2012.

[40] Greg Swain. The susceptibility to surface corrosion in acidic fluoride media: A comparison of diamond, hopg, and glassy carbon electrodes. *Journal of The Electrochemical Society - J ELECTROCHEM SOC*, 141, 12 1994.

[41] M. Panizza and G. Cerisola. Application of diamond electrodes to electrochemical processes. *Electrochimica Acta*, 51(2):191 – 199, 2005.

[42] R. Ramesham and M.F. Rose. Electrochemical characterization of doped and undoped cvd diamond deposited by microwave plasma. *Diamond and Related Materials*, 6(1):17 – 26, 1997.

[43] Charles Agnès. *Le diamant dopé au bore pour la bioèlectronique : biocompatibilité et fonctionnalisation.* PhD thesis, Université Joseph Fourier, Grenoble, 2009.

[44] Christian G. Specht, Oliver A. Williams, Richard B. Jackman, and Ralf Schoepfer. Ordered growth of neurons on diamond. *Biomaterials*, 25(18):4073 – 4078, 2004.

[45] Anke Kruger, Yuejiang Liang, Gerald Jarre, and Jochen Stegk. Surface functionalisation of detonation diamond suitable for biological applications. *J. Mater. Chem.*, 16:2322–2328, 2006.

[46] Wensha Yang, Orlando Auciello, James E. Butler, Wei Cai, John A. Carlisle, Jennifer E. Gerbi, Dieter M. Gruen, Tanya Knickerbocker, Tami L. Lasseter, John N. Russell Jr., Lloyd M. Smith, and Robert J. Hamers. Dna-modified nanocrystalline diamond thin-films as stable, biologically active substrates. *Nature Materials*, 1:253, November 2002.

[47] Anke Krüger. Hard and soft: Biofunctionalized diamond. *Angewandte Chemie International Edition*, 45(39):6426–6427, 2006.

[48] Michael J. Burek, Yiwen Chu, Madelaine S.Z. Liddy, Parth Patel, Jake Rochman, Mikhail Lukin, and Marko Loncar. High-q optical nanocavities in bulk single-crystal diamond. In *CLEO: 2014*, page SM4M.3. Optical Society of America, 2014.

[49] Luozhou Li, Tim Schroder, Edward H. Chen, Hassaram Bakhru, and Dirk Englund. One-dimensional photonic crystal cavities in single-crystal diamond. *Photonics and Nanostructures - Fundamentals and Applications*, 15:130 – 136, 2015.

[50] T. V. Kononenko, P. N. Dyachenko, and V. I. Konov. Diamond photonic crystals for the ir spectral range. *Opt. Lett.*, 39(24):6962–6965, Dec 2014.

[51] Michael J. Burek, Nathalie P. de Leon, Brendan J. Shields, Birgit J. M. Hausmann, Yiwen Chu, Qimin Quan, Alexander S. Zibrov, Hongkun Park, Mikhail D. Lukin, and Marko Loncar. Free-standing mechanical and photonic nanostructures in single-crystal diamond. *Nano Letters*, 12(12):6084–6089, 2012. PMID: 23163557.

[52] Igal Bayn, Boris Meyler, Joseph Salzman, and Rafi Kalish. Triangular nanobeam photonic cavities in single-crystal diamond. *New Journal of Physics*, 13(2):025018, 2011.

[53] Thomas M. Babinec, Jennifer T. Choy, Kirsten J. M. Smith, Mughees Khan, and Marko Lon?ar. Design and focused ion beam fabrication of single crystal diamond nanobeam cavities. *Journal of Vacuum Science & Technology B*, 29(1):010601, 2011.

[54] Chiou-Fu Wang, Ronald Hanson, Tatyana Feygelson, Jie Yang, James Butler, David Awschalom, and Evelyn Hu. Fabrication and characterization of two-dimensional photonic crystal microcavities in nanocrystalline diamond. *Applied Physics Letters*, 91, 09 2007.

[55] Candice Blin, Xavier Checoury, Hugues A. Girard, Céline Gesset, Samuel Saada, Philippe Boucaud, and Philippe Bergonzo. Optical analysis of p-type surface conductivity in diamond with slotted photonic crystals. *Advanced Optical Materials*, 1(12):963–970, 2013.

[56] Shanhui Fan and J.D. Joannopoulos. Analysis of guided resonances in photonic crystal slabs. 65:235112, 06 2002.

[57] Ian M. White and Xudong Fan. On the performance quantification of resonant refractive index sensors. *Opt. Express*, 16(2):1020–1028, Jan 2008.

[58] Shouyuan Shi, Caihua Chen, and Dennis W. Prather. Plane-wave expansion method for calculating band structure of photonic crystal slabs with perfectly matched layers. *J. Opt. Soc. Am. A*, 21(9):1769–1775, Sep 2004.

[59] J. Joannopoulos. Mpb. Technical report, 2018.

[60] Kane S. Yee. Numerical solution of initial boundary value problem involving maxwell's equations in isotropic media. *IEEE Trans. Antennas and Propagation*, AP-14:302–307, 06 1966.

[61] Joannopoulos. Meep. Technical report, https://meep.readthedocs.io/en/latest/, 2018.

[62] Costa Nicolaou, Wah Tung Lau, Raanan Gad, Hooman Akhavan, Ryan Schilling, and Ofer Levi. Enhanced detection limit by dark mode perturbation in 2d photonic crystal slab refractive index sensors. *Opt. Express*, 21(25):31698–31712, Dec 2013.

[63] Candice Blin. *Développement de cristaux photoniques en diamant : modélisation, technologie et application à la biodetection.* PhD thesis, Université Pierre et Marie Curie, 2015.

[64] J. Juan-Colas, Thomas F. Krauss, and Steven D. Johnson. Real-time analysis of molecular conformation using silicon electrophotonic biosensors. *ACS Photonics*, 4(9):2320–2326, 2017.

[65] W J P van Enckevort and E H Versteegen. Temperature dependence of optical absorption by the single-substitutional nitrogen donor in diamond. *Journal of Physics: Condensed Matter*, 4(9):2361, 1992.

[66] Seiichiro Matsumoto, Yoichiro Sato, Mutsukazu Kamo, and Nobuo Setaka. Vapor deposition of diamond particles from methane. *Japanese Journal of Applied Physics*, 21, 04 1982.

[67] Seiichiro Matsumoto, Yoichiro Sato, Masayuki Tsutsumi, and Nobuo Setaka. Growth of diamond particles from methane-hydrogen gas. *Journal of Materials Science*, 17:3106–3112, 11 1982.

[68] Mutsukazu Kamo, Yoichiro Sato, Seiichiro Matsumoto, and Nobuo Setaka. Diamond synthesis from gas phase in microwave plasma. *Journal of Crystal Growth*, 62(3):642 – 644, 1983.

[69] J J Gracio, Q H Fan, and J C Madaleno. Diamond growth by chemical vapour deposition. *Journal of Physics D: Applied Physics*, 43(37):374017, 2010.

[70] James E Butler and Ivan Oleynik. A mechanism for crystal twinning in the growth of diamond by chemical vapour deposition. *Philosophical Transactions of the Royal Society of London A: Mathematical, Physical and Engineering Sciences*, 366(1863):295–311, 2008.

[71] Hideaki Yamada, Akiyoshi Chayahara, and Yohiaki Mokuno. Effects of intentionally introduced nitrogen and substrate temperature on growth of diamond bulk single crystals. *Japanese Journal of Applied Physics*, 55(1S):01AC07, 2016.

[72] Hugues A. Girard, Sandrine Perruchas, Céline Gesset, Marc Chaigneau, Laetitia Vieille, Jean-Charles Arnault, Philippe Bergonzo, Jean-Pierre Boilot, and Thierry Gacoin. Electrostatic grafting of diamond nanoparticles: A versatile route to nanocrystalline diamond thin films. *ACS Applied Materials & Interfaces*, 1(12):2738–2746, 2009. PMID: 20356151.

[73] S. Saada, S. Pochet, L. Rocha, J.C. Arnault, and P. Bergonzo. Real time investigation of diamond nucleation by laser scattering. *Diamond and Related Materials*, 18(5):707 – 712, 2009. Proceedings of Diamond 2008, the 19th European Conference on Diamond, Diamond-Like Materials, Carbon Nanotubes, Nitrides and Silicon Carbide.

[74] Nicolas Vaissière. *Synthèse de films de diamant de haute qualité cristalline pour la réalisation de dosimètres pour la radiothérapie*. PhD thesis, École normale supérieure de Cachan - ENS Cachan, 2014.

[75] Colin Delfaure. *Etude et réalisation de fenêtres innovantes en diamant : application aux tubes à rayons x*. PhD thesis, Université Pierre-et-Marie-Curie, 2016.

[76] Compton Richard G., Foord John S., and Marken Frank. Electroanalysis at diamond-like and doped-diamond electrodes. *Electroanalysis*, 15(17):1349–1363.

[77] C. Teichert, J. F. MacKay, D. E. Savage, M. G. Lagally, M. Brohl, and P. Wagner. Comparison of surface roughness of polished silicon wafers measured by light scattering topography, soft-x-ray scattering, and atomic-force microscopy. *Applied Physics Letters*, 66(18):2346–2348, 1995.

[78] Sum Huan Ng. *Measurement and modeling of fluid pressures in chemical mechanical polishing*. PhD thesis, Georgia Institute of Technology, 2005.

[79] Fnu Atiquzzaman. *Chemical Mechanical Planarization of Electronic Materials*. PhD thesis, University of South Florida, 2012.

[80] H.Y. Tsai, C.J. Ting, and C.P. Chou. Evaluation research of polishing methods for large area diamond films produced by chemical vapor deposition. *Diamond and Related Materials*, 16(2):253 – 261, 2007.

[81] Wen-Chang Chen and Cheng-Tyng Yen. Chemical-mechanical polishing of low dielectric constant poly(silsesquioxane): Hsq. 6:197–202, 07 1999.

[82] S. Roy, V.K. Balla, A.K. Mallik, V.G. Ralchenko, A.P. Bolshakov, E.E. Ashkinazi, and N. Dandapat. A comprehensive study of mechanical and chemo-mechanical polishing of cvd diamond. *Materials Today: Proceedings*, 5(3, Part 3):9846 – 9854, 2018. International Conference on Functional Nano-Materials, 28-29 September, 2016.

[83] C. Vivensang, L. Ferlazzo-Manin, M.F. Ravet, G. Turban, F. Rousseaux, and A. Gicquel. Surface smoothing of diamond membranes by reactive ion etching process. *Diamond and Related Materials*, 5(6):840 – 844, 1996. Proceedings of the 6th European Conference on Diamond, Diamond-like and Related Materials Part 2.

[84] M. Rabarot, J. Widiez, S. Saada, J.-P. Mazellier, C. Lecouvey, J.-C. Roussin, J. Dechamp, P. Bergonzo, F. Andrieu, O. Faynot, S. Deleonibus, L. Clavelier, and J.P. Roger. Silicon-on-diamond layer integration by wafer bonding technology. *Diamond and Related Materials*, 19(7):796 – 805, 2010. Proceedings of Diamond 2009, The 20th European Conference on Diamond, Diamond-Like Materials, Carbon Nanotubes and Nitrides, Part 2.

[85] X. Checoury, D. Néel, P. Boucaud, C. Gesset, H. Girard, S. Saada, and P. Bergonzo. Nanocrystalline diamond photonics platform with high quality factor photonic crystal cavities. *Applied Physics Letters*, 101(17):171115, 2012.

[86] http://www.fujifilm.com.sg/Innovation/Technologies/Grinding-of solids/. Copper cmp slurry (materials for semiconductor manufacturing process). Technical report, fujifilm, website visited 03/07/2018.

[87] Abaneshwar Prasad George Fotou Shoutian Li. The effect of polymer hardness, pore size and porosity on the performance of thermoplastic polyurethane (tpu) based chemical mechanical polishing (cmp) pads. Technical report, Cabot Microelectronics Corporation, 2014.

[88] M.Sivanandini Sukhdeep S Dhami B S Pabla. Chemical mechanical polishing by colloidal silica slurry. *International Journal of Engineering Research and Applications (IJERA) ISSN: 2248-9622 www.ijera.com Vol. 3, Issue 3, May-Jun 2013, pp.1337-1345*, 2013.

[89] C. W. Holzwarth, T. Barwicz, and Henry I. Smith. Optimization of hydrogen silsesquioxane for photonic applications. *Journal of Vacuum Science & Technology B: Microelectronics and Nanometer Structures Processing, Measurement, and Phenomena*, 25(6):2658–2661, 2007.

[90] Y K. Siew, G Sarkar, Xiao (Matthew Hu, J Hui, A See, and C T. Chua. Thermal curing of hydrogen silsesquioxane. 147:335–339, 01 2000.

[91] Dow Corning Corporation. Information about fox ® -1x and fox -2x flowable oxides. Technical report, Dow Corning Corporation, 2005.

[92] Dow Corning Corporation. Dow corning ® xr-1541 e-beam resist. Technical report, Dow Corning Corporation, 2008.

[93] A.M. Hynes, H. Ashraf, J.K. Bhardwaj, J. Hopkins, I. Johnston, and J.N. Shepherd. Recent advances in silicon etching for mems using the ase tm process. *Sensors and Actuators A: Physical*, 74(1):13 – 17, 1999.

[94] Ivo W. Rangelow. Critical tasks in high aspect ratio silicon dry etching for microelectromechanical systems. *Journal of Vacuum Science & Technology A*, 21(4):1550–1562, 2003.

[95] Tibor Izak, Alexander Kromka, Oleg Babchenko, Martin Ledinsky, Karel Hruska, and Elisseos Verveniotis. Comparative study on dry etching of polycrystalline diamond thin films. *Vacuum*, 86(6):799 – 802, 2012.

[96] R. Otterbach and U. Hilleringmann. Reactive ion etching of cvd-diamond for piezoresistive pressure sensors. *Diamond and Related Materials*, 11(3):841 – 844, 2002. 12th European Conference on Diamond, Diamond- Like Materials, Carbon Nanotubes, Nitrides & Silicon Carbide.

[97] A.P Malshe, B.S Park, William Brown, and Hameed Naseem. A review of techniques for polishing and planarizing chemically vapor-deposited (cvd) diamond films and substrates. 8:1198–1213, 07 1999.

[98] P. W. Leech, G. K. Reeves, and A. Holland. Reactive ion etching of diamond in cf4, o2, o2 and ar-based mixtures. *Journal of Materials Science*, 36(14):3453–3459, Jul 2001.

[99] Mathieu Lions. *Synthése et caractérisation de films ultraminces de diamant polycristallin pour les applications Silicon-On-Diamond.* PhD thesis, Université Pierre et Marie Curie, 2011.

[100] Sage Doshay. Hsq bonding, using evbond,updated. Technical report, Standford University, 2015.

[101] K. Ryu J. W. Chung B. Lu and T. Palacios. Wafer bonding technology in nitride semiconductors for applications in energy and communications. In *ECS Transactions, 33 (4) 125-135 (2010) 10.1149/1.3483500 © The Electrochemical Society*, 2010.

[102] Lai-Cheng Chen, Minjan Chen, Chenhsin Lien, and ChiâChao Wan. The band model and the etching mechanism of silicon in aqueous koh. 142:170–176, 01 1995.

[103] Hee Han, Zhipeng Huang, and Woo Lee. Metal-assisted chemical etching of silicon and nanotechnology applications. *Nano Today*, 9(3):271 – 304, 2014.

[104] Ernesto Vargas Catalan, Pontus Forsberg, Olivier Absil, and Mikael Karlsson. Controlling the profile of high aspect ratio gratings in diamond. *Diamond and Related Materials*, 63:60 – 68, 2016. 9th International Conference on New Diamond and Nano Carbons â NDNC 2015.

[105] K. Teii, M. Hori, and T. Goto. Codeposition on diamond film surface during reactive ion etching in sf6 and o2 plasmas. *Journal of Vacuum Science & Technology A*, 18(6):2779–2784, 2000.

[106] Zheng HAN. *Vers le laser Raman à cristal photonique en filière silicium.* PhD thesis, Universitè Paris-Sud XI U.F.R. Scientifique d'Orsay, 2010.

[107] Delphine Neel. *Etude en champ proche optique de guides à cristaux photoniques sur SOI.* PhD thesis, Institut national des sciences appliquées de Lyon, 2006.

[108] Mark P. Hiscocks, Christopher J. Kaalund, cois Ladouceur Fran Shane T. Huntington, Brant C. Gibson, Steven Trpkovski, David Simpson, Eric Ampem-Lassen, Steven Prawer, and James E. Butler. Reactive ion etching of waveguide structures in diamond. *Diamond and Related Materials*, 17(11):1831 – 1834, 2008.

[109] Thorlabs. Stabilized tungsten light sources user guide compact stabilized light sources. Technical report, Thorlabs, 2017.

[110] Thorlabs. Ccs series spectrometer operation manual. Technical report, Thorlabs, 2018.

[111] Thorlabs. Ddr 25 direct drive rotation stage. Technical report, Thorlabs, 2018.

[112] M. Galli, S. L. Portalupi, M. Belotti, L. C. Andreani, L. O'Faolain, and T. F. Krauss. Light scattering and fano resonances in high-q photonic crystal nanocavities. *Applied Physics Letters*, 94(7):071101, 2009.

[113] G. N. Ramachandran. Thermo-optic behavior of solids. 1947.

[114] C. Blin, Z. Han, H. A. Girard, P. Bergonzo, P. Boucaud, M. El Kurdi, S. Saada, S. Sauvage, and X. Checoury. Surface-sensitive diamond photonic crystals for high-performance gas detection. *Opt. Lett.*, 41(18):4360–4363, Sep 2016.

[115] A. Sinibaldi A. Anopchenko R. Rizzo N. Danz P. Munzert P. Rivolo F. Frascella S. Ricciardi F. Michelotti. Angularly resolved ellipsometric optical biosensing by means of bloch surface waves. *Analytical and Bioanalytical Chemistry*, 407(14):3965–3974, 05 2015.

[116] H.A. Girard, J.C. Arnault, S. Perruchas, S. Saada, T. Gacoin, J.-P. Boilot, and P. Bergonzo. Hydrogenation of nanodiamonds using mpcvd: A new route toward organic functionalization. *Diamond and Related Materials*, 19(7):1117 – 1123, 2010. Proceedings of Diamond 2009, The 20th European Conference on Diamond, Diamond-Like Materials, Carbon Nanotubes and Nitrides, Part 2.

[117] H. A. Girard, T. Petit, S. Perruchas, T. Gacoin, C. Gesset, J. C. Arnault, and P. Bergonzo. Surface properties of hydrogenated nanodiamonds: a chemical investigation. *Phys. Chem. Chem. Phys.*, 13(24):11517–11523, 2011.